UNIVERSITÄT STUTTGART

TITEL DER DOKTORARBEIT

Silicon Vacancy Defects in 4H-Silicon Carbide Semiconductor for Quantum Applications

---

Von der Fakultät 5 Informatik, Elektrotechnik und Informationstechnik der Universität Stuttgart zur Erlangung der Würde eines Doktors der Ingenieurwissenschaften (Dr.-Ing.) genehmigte Abhandlung

Vorgelegt von
Roland Nagy
aus Oberwischau

Hauptberichter: Prof. Dr. Jens Anders
Mitberichter: Prof. Dr. Jörg Wrachtrup

Tag der mündlichen Prüfung: 23.10.2019

Institut für Intelligente Sensorik und Theoretische Elektrotechnik (IIS) der Universität Stuttgart

Erscheinungsjahr 2019
27.10.2019

Eidesstattliche Erklärung

Ich, Roland Nagy, erkläre hiermit, dass ich die vorliegende Arbeit “Silicon Vacancy Defects in 4H-Silicon Carbide Semiconductor for Quantum Applications” selbstständig und nur unter Benutzung der angegebenen Literatur und Hilfsmittel angefertigt habe. Wörtlich übernomme Sätze oder Satzteile aus eigenen Publikatonen sind zum beginn des jeweiligen Kapitels vermerkt, andere Anlehnungen hinsichtlich Aussage und Umfang unter Quellenangabe kenntlich gemacht. Die Arbeit hat in gleicher oder ähnlicher Form noch keiner Prüfungsbehörde vorgelegen und ist nicht veröffentlich.

Unterschrift:

_____

Datum:

_____

Declaration of Authorship

I, Roland Nagy, declare that this thesis titled, “Silicon Vacancy Defects in 4H-Silicon Carbide Semiconductor for Quantum Applications” and the work presented in it are my own. All information used in this thesis is listed under bibliography. Sentences and parts used in this theses from my own publications are mentioned at the begin of a chapter.

Signed:

Date:

UNIVERSITÄT STUTTGART

Zusammenfassung

Department of Electrical Engineering and Information Science
and
Department of Math and Physics

Doktor der Ingenieurwissenschaften

Silicon Vacancy Defects in 4H-Silicon Carbide Semiconductor for Quantum Applications

by Roland Nagy

Die sichere Übertragung von Informationen ist in unserem Computerzeitalter ein Schlüsselaspekt für die Industrie und staatliche Einrichtungen. Die Umsetzung eines Netzwerkes, das abhörsicheres Übertragen von Daten erlaubt, kann in einem Quantennetzwerk realisiert werden. Ein Quantennetzwerk besteht aus Knotenpunkten (Quantensysteme, an denen Rechenoperationen durchgeführt werden), die durch Quantenrepeater verbunden sind. Dieses Quantennetzwerk benutzt, ebenfalls wie ein klassisches Netzwerk, Photonen im Telekomwellenlängenbereich zur Übertragung von Informationen. Dadurch kann zum einen die klassische Infrastruktur genutzt werden und zum anderen die Kompatibilität zu klassischen Netzwerken gewahrt werden. Wie ein klassisches Netzwerk benötigt ein Quantennetzwerk zum Ablegen der Informationen und zur Erzeugung von Verschränkung einen Zwischenspeicher. Zusätzlich muss ein Quantennetzwerk skalierbar und kostengünstig im Aufbau sein. Die erste Demonstration eines Quantennetzwerkes mit einem Festkörper konnte mit dem NV-Zentrum in einem Diamanten realisiert werden. Dieser Schritt konnte zeigen, dass ein Quantennetzwerk mit NV-Zentren generell umsetzbar ist, jedoch auch Nachteile mit sich bringt. Das NV-Zentrum im Diamanten legt gute kohärente Spin-Eigenschaften dar, jedoch sind nur 3-4 % aller emittierten Photonen für ein Quantennetzwerk brauchbar. Ein weiterer, womöglich noch wichtigerer, Aspekt ist die spektrale Instabilität des NV-Zentrums im Diamanten. Spektral instabil bedeutet, dass sich die Energie zwischen dem Grund- und Angeregtem-Zustand kontinuierlich ändert. Alle NV-Zentren in den Knotenpunkten müssen jedoch die exakt gleiche Energie in Anregung besitzen. Dieser Aspekt führt dazu, dass etwa alle einhundert Mikrosekunden überprüft werden muss, ob dies der Fall ist. Eine derartige Überprüfung verringert jedoch die Rate eines Netzwerkes massiv. Die genannten Probleme haben zur Folge, dass bei einer realistischen und effizienten kommerziellen Umsetzung eines Quantennetzwerkes Schwierigkeiten auftreten können. In der vorliegenden Doktorarbeit wurde ein alternativer Ansatz zur Lösung des Problems gefunden. Als Festkörper wurde Siliziumkarbid gewählt, da es in der Halbleiterfertigung CMOS kompatibel ist (Kapitel 2). Der Halbleiter Siliziumkarbid besitzt eine Bandlücke von > 3 eV und gute Fabrikationseigenschaften. Aus

der Literatur ist ebenfalls bekannt, dass Siliziumkarbid mehrere Quantendefekte besitzt. Die charakteristischen Eigenschaften der Siliziumfehlstelle in 4H-Siliziumkarbid wurden in der vorliegenden Doktorarbeit untersucht. Die Null-Phononen-Linien Emission der untersuchten Siliziumfehlstelle liegt bei 861 nm. Von verschiedenen wissenschaftlichen Gruppen konnte gezeigt werden, dass sich die Wellenlänge von 861 nm effizient auf 1550 nm (Telekomwellenlänge) konvertieren lässt. Zu Beginn der Forschung wurden Spin-Eigenschaften von Siliziumfehlstellen in ensembles untersucht. Dabei konnte festgestellt werden, dass sich Siliziumfehlstellen kohärent manipulieren lassen (Kapitel 3). Die erste Messung an einer einzelnen Siliziumfehlstelle konnte zeigen, dass 40 % der emittierten Photonen für ein Quantennetzwerk genutzt werden können. Im Vergleich zum NV - Zentrum im Diamant sind die emittierten Photonen um den Faktor zehn gröSSer. Die optischen Eigenschaften wurden im Kapitel 4 mit einer resonanter optischen Anregung untersucht. Das Ergebnis dieser Messung konnte so nicht erwartet werden, da die optischen Übergänge spektral stabil sind. Diese spektrale Stabilität impliziert, dass sich die Energie zwischen dem Grund- und Angeregten-Zustand nahezu nicht verändert. Spektral stabile optische Übergänge waren bis zu der oben genannten Entdeckung nur bei Quantendefekten mit Inversionssymmetrie bekannt. Siliziumkarbid ist ein piezoelektrisches Material. Aus diesem Grund kann Siliziumkarbid keine Quantendefekte mit Inversionssymmetrie haben. Der Grund für die spektrale Stabilität liegt in derselben Symmetrie der Grund- und Angeregten-Zustände. Dies hat zur Folge, dass der Dipolmoment im Grund- und Angeregten-Zustand fast identisch ist (siehe Kapitel 4). Das untersuchte Ergebnis konnte zeigen, dass eine Vielzahl von Materialien, die zuvor nicht in Betracht gezogen wurden, Quantendefekte mit spektral stabilen optischen Übergängen besitzen können. Kohärente Spin-Messungen an einzelnen Siliziumfehlstellen haben gezeigt, dass die Kohärenzzeit $T_2 \approx 1$ ms beträgt und somit vergleichbar mit einem NV-Zentrum im Diamanten ist. Mit dem NV-Zentrum im Diamanten konnte gezeigt werden, dass sich Kohlenstoff- oder Stickstoff-Isotope als Speicher verwenden lassen können. Diese Möglichkeit besteht ebenfalls bei der Siliziumfehlstelle in Siliziumkarbid, das ^{13}C und ^{29}Si besitzt. Durch die hohe spektrale Stabilität konnte in Kapitel 5 veranschaulicht werden, dass die optischen Absorptionslinien von Siliziumfehlstellen nahezu nicht unterscheidbar sind. In der Doktorarbeit konnte herausgearbeitet werden, dass eine Siliziumfehlstelle in 4H-SiC exzellente physikalische Eigenschaften (optische und Spin-Eigenschaften) besitzt. Resultierend aus den genannten Eigenschaften kann festgestellt werden, dass eine Siliziumfehlstelle in Siliziumkarbid als beachtenswert berücksichtigt werden muss, wenn es um die Umsetzung eines Festkörperquantennetzwerkes geht.

UNIVERSITÄT STUTTGART

Abstract

Department of Electrical Engineering and Information Science
and
Department of Math and Physics

Doktor der Ingenieurwissenschaften

Silicon Vacancy Defects in 4H-Silicon Carbide Semiconductor for Quantum Applications

by Roland Nagy

Secure transmission of information is a crucial element nowadays for industry and national security. Today, the only known way to establish provably secure communication is based on quantum key distribution in a quantum network. Currently, transmission rates and communication distances are limited by (unavoidable) optical loss in fibers and the fundamental quantum no-cloning theorem. In analogy to classical communication, improved network performance is obtained in a network based on multiple nodes that are connected by (quantum) repeaters. The information should be transferred with telecom-wavelength photons to be compatible with existing classical fiber networks. The nodes and repeaters need to consist of a quantum system with good optical properties and long memory times, e.g. using a spin with high coherence. Additionally, such memories will be useful for computation and entanglement creation. A realistic quantum system should also be scalable and cheap in fabrication. The first demonstration of a solid state quantum repeater has been recently realized with the NV-centre in diamond. This demonstration showed that the NV-centre in diamond can be used in principle as a quantum repeater but it also brings drawbacks. The NV-centre in diamond has a good spin coherence but a low emission of photons inside the zero phonon line which can be used in a quantum network. A crucial challenge for color defects like the NV-centre in diamond is spectral stability. After a certain amount of time, a sanity check needs to be done to measure the wavelength of the resonant absorption lines. Any change in absorption wavelength requires adapting a multitude of experimental parameters, which is a show-stopper for long-term network reliability. These drawbacks decrease the transmission rate within a quantum network. If one would plan to realize a commercial quantum network, a tailored quantum system with all the mentioned desired properties would be needed. My first approach in this thesis was to use a semiconductor material like 4H-SiC with matured industrial fabrication knowledge (Chapter 2). 4H-SiC hosts a large variety of known quantum defects. I choose to analyze the silicon vacancy V_1 centre because of the ZPL emission at 861 nm. It is known from the literature that this wavelength can be efficiently converted to commonly used telecom wavelengths (1530 - 1625 nm). I first analyzed the

optical and spin properties in ensembles (Chapter 3). The spin measurement showed that one can coherently manipulate silicon vacancy V_1 centre. Emission spectra of a single silicon vacancy V_1 centres showed that ≈ 40 % of the emission is guided into the ZPL (≈ 3 % NV centre). I perform resonant excitation studies in Chapter 4 to investigate the optical properties. Surprisingly, the result showed spectrally stable optical transitions, which was not expected. The general opinion in the research community during this time was that only defects with inversion symmetry can show spectrally stable transitions. 4H-SiC is a piezo electric material which, by definition can not host inversion symmetry quantum defects. The physical origin of spectrally stable transitions for the V_1 centre in 4H-SiC was found in the symmetry of the ground and excited state. Both states share the same symmetry and, more importantly, nearly the same dipole moment. The symmetry shields the optical transition frequencies of the silicon vacancy V_1 centre against electric field fluctuations and causes spectrally stable optical transitions. For the research community, this discovery opened a new approach in identifying spectrally stable quantum defects in various materials. I analyzed additionally the spin coherence properties of a single silicon vacancy V_1 centre and measured a spin coherence time up to 1 ms, which is comparable with the NV-centre in diamond. It has been shown for the NV-centre in diamond that nuclear spins can be used as quantum memory. In 4H-SiC, two types of isotopes exist, ^{29}Si and ^{13}C, that can also be exploited as a quantum memory. It turned also out that the symmetries of ground and excited states are responsible for very low inhomogeneous distribution of the V_1 centre resonant absorption lines. In Chapter 5, this property is investigated, especially in view of experiments that require multiple indistinguishable single photon emitters. In my thesis I present the physical properties of a quantum system with excellent optical and spin properties. Additionally, the indistinguishable single photon emission of silicon vacancy V_1 centre and mature fabrication knowledge in 4H-SiC make the systems scalable. All these properties combined makes the silicon vacancy V_1 centre in 4H-SiC an excellent candidate for the realization of a quantum repeater network.

Acknowledgements

First I would like to thank my parents **Margarete** and **Johann Nagy** who always supported and guided me. I also want to thank my brother **Victor Nagy** for your time and help. Congratulations on your marriage! My special gratitude goes to my beloved girlfriend **Christiane Harstel** for your support during my time as a PhD student. I also want to thank **Prof. Dr. Jörg Wrachtrup** and **Prof. Dr. Jens Anders** for the opportunity, guidance and help during my PhD. I had the chance during my PhD to be supervised by many talented scientist, I want to thank all of you (**Dr. Helmut Fedder**, **Dr. Sang-Yun Lee** and **Dr. Florian Kaiser**). I also want to thank my colleagues **Matthias Widmann** and **Matthias Niethammer** for your support at the start of my PhD. **Thomas Öckinghaus** and **Johannes Greiner** for the great discussions and time that we shared together, thank you! **Nathan Chejanovsky** we had an amazing time during our PhD, thank you! I also want the thank **Dr. Florian Kaiser** for the great time with him in the lab and in Nice.
I want to thank all the people who supported me during my time as a PhD student!

- **Claudia Unger:** I want to thank you for all the help that I received from you!
- **Britta Lenz:** Thank you for your help with the travel department.
- **Ivanka Spajic:** Thank you for your help every morning with my cup!
- **Stephan Hirschmann:** Thank you Stephan for the smile on your face and technical support.
- **Rainer Stöhr:** Thank you for the great moments during the time when we shared our office, fabrication of amazing nano-structures and reading my thesis!
- **Roman Koselov:** Thank you for your support with equipment and many experimental advice!
- **Durga Dasari:** My thesis would not have been possible without your amazing support in theoretical physics, thank you!
- **Amit Finkler:** It was a great time with you Amit! Thank your help with HF etching!
- **Sen Yang:** Thank you for hosting me in your office at the start of my thesis!
- **Thomas Häberle:** It was a great time with you at our institute, I will never forget our first conversation!
- **Ingmar Jakobi:** Thank you for taking care about our home build laser and beverages for the institute!
- **Philip Neumann:** Thank you for our discussions and managing our coffee supply at the institute!
- **Naoya Morioka:** I wish you good luck and success with my setup!

- **Ilja Gerhardt:** Thank you for showing me how to operate our ring laser!
- **Cristian Bonato:** Thank you for coming to Stuttgart for a couple of months and supervising me at the start of my thesis!
- **Adam Gali:** Thank you for your group theoretical support during my thesis!
- **Oney Soykal:** I want to thank you for the theoretical support during my thesis!
- **Peter Udvarhelyi:** Thank you for the great paper which we had together!
- **Tien Son Nguyen:** Without your support and expertise with SiC, my thesis would not have been possible to realize, thank you!
- **Jawad Ul-Hassan:** Thank you for growing these amazing SiC samples!
- **Takeshi Oshima:** Thank you for electron irradiation of our samples!
- **Patrick Berwian:** Thank you Patrick for our collaboration on SiC and supplying us with sample!
- **Birgit Kallinger:** Thank you for our discussions on SiC and sharing your knowledge!
- **David Bracher:** It was a great time with you David!
- **Xingyu Alex Zhang:** I want to thank you for the great time with you and our collaboration on SiC.
- **Evelyn Hu:** I want to thank you for hosting me at Harvard and for the great discussions that we had. I also want to thank you for the samples that you shared with us!
- **David Hunger:** Thank you David for our collaboration!

If one would ask me "what was the most special moment during your PhD time? " I would probably answer "The Friday evenings with **Prof. Dr. Jörg Wrachtrup** and **Dr. Florian Kaiser** performing with me together experiments on my setup". Thank you for this productive time!

Contents

List of Figures

List of Tables

Physical Constants

Speed of Light	$c_0 = 2.997\,924\,58 \times 10^{8}\,\mathrm{m\,s^{-1}}$ (exact)
Planck Constant	$\mathrm{h} = 6.626\,070\,15 \times 10^{-34}\,\mathrm{J\,s}$
Reduced Planck Constant	$\hbar = 3.161\,526\,49 \times 10^{-26}\,\mathrm{J\,m}$
Boltzmann Constant	$\mathrm{k} = 1.380\,648\,52 \times 10^{-23}\,\mathrm{J\,K^{-1}}$
Elementary Charge	$\mathrm{e} = 1.603\,176\,62 \times 10^{-19}\,\mathrm{C}$
Coulomb Constant	$k_e = 8.987\,551\,78 \times 10^{9}\,\mathrm{N m^{-2} C^{-2}}$
Vacuum Permittivity	$\epsilon_0 = 8.854\,187\,82 \times 10^{-12}\,\mathrm{F\,m^{-1}}$
Vacuum Permeability	$\mu_0 = 1.256\,637\,06 \times 10^{-19}\,\mathrm{N A^{-2}}$
Bohr Magneton	$\mu_B = 927.400\,994 \times 10^{-26}\,\mathrm{J\,T^{-1}}$
Bohr Radius	$a_0 = 5.291\,772 \times 10^{-11}\,\mathrm{m}$
Electron Mass	$m_e = 9.109\,383 \times 10^{-31}\,\mathrm{kg}$
Electron Gyromagnetic	$\gamma_e = 1.760\,859 \times 10^{11}\,\mathrm{s^{-1}\,T^{-1}}$
Proton Gyromagnetic Ratio	$\gamma_p = 2.675\,221 \times 10^{8}\,\mathrm{s^{-1}\,T^{-1}}$
Electron Magnetic Moment	$\mu_e = -9.284\,764 \times 10^{-24}\,\mathrm{J\,T^{-1}}$
Proton Magnetic Moment	$\mu_p = 1.410\,606 \times 10^{-26}\,\mathrm{J\,T^{-1}}$

List of Symbols

AOM	Acousto-Optic Modulator
APD	Avalanche Photo Diode
AWG	Arbitrary-Waveform Generator
BS	Beam Splitter
$CPMG$	Carr-Purcell-Meiboom-Gill sequence
CVD	Chemical Vapor Deposition
CW	Continuous Wave
DD	Dynamical Decoupling
EOM	Electro-Optic Modulator
ESR	Electron-Spin Resonance
EPR	Electron-Paramagnetic Resonance
FFT	Fast Fourier Transformation
FTL	Fourier Transform Limited
FIB	Focused Ion Beam
FID	Free Induction Decay
$FWHM$	Full-Width at Half-Maximum
HWP	Half-Wave Plate
LED	Light-Emitting Diode
MW	Microwave
NMR	Nuclear-Magnetic Resonance
$NVcentre$	Nitrogen Vacany Centre (in Diamond)
$ODMR$	Optically-Detected Magnetic Resonance
PSB	Phonon Side Band
PSD	Power Spectral Density
PSF	Point Spread Function
$Wedge$	Wedge Mirror
RF	Radiofrequency
RMS	Root Mean Square
SNR	Signal-to-Noise Ratio

SSR	Single-Shot Readout
SiC	Silicon Carbide
SM	Spectrometer
$SMIQ$	Vector-Signal-Generator
T_1	Longitudinal Relaxation Time
T_2	Transverse Telaxation Time
$T_2^\star$	Inverse Inhomogeneous Broadening
PBS	Polarizing Beam Splitter
PH	Pinhole
QWP	Quarter-Wave Plate
Si_V	Silicon Vacancy Centre (in Diamond)
ZFS	Zero-Field Splitting
ZPL	Zero-Phonon Line

I dedicate this thesis to my beloved family and girlfriend.
"Accidit in puncto, quod non speratur in anno"

CHAPTER 1

Introduction

We are living in a society that has to face the challenge of inducing the transition from classical to quantum technologies. The development of our highly advanced electronics technology sector was a major step forward for prosperity in the last century. Already in 1965, Gordon E. Moore (co founder of Intel corp.) proposed how classical electronics technology should scale to increase the performance on one hand and to decrease the price for the consumer on the other hand (Moore, 1965). He also pointed out in 1965 that the development of classical electronics will end at a certain point where the size of electronics structures reaches the quantum realm. A simple example is a metal nanowire with a size of $\approx$ 1 nm (Takayanagi, Kondo, and Ohnishi, 2001) where the mean free path of an electron can be already longer than the size of the nanowire. In this region, the physics is described by quantum mechanics instead of classical physics where effects like quantum tunneling can occur. In classical physics, information is represented by "0" and "1", which we call bits. In the quantum mechanic region the bits are represented by arbitrary superposition states of "0" and "1", called qubit. This superposition state of "0" and "1" allows a completely new approach of technology development.

The development of quantum mechanics started more than 100 years ago with Max Planck who developed the mathematical framework to explain the emission of a perfect black body. In this framework, the energy of the light field is quantized in multiples of a constant h, which is nowadays known as the Planck constant (Planck, 1890). This discovery created a new field of research, which we know nowadays as quantum mechanics. Many famous physicist (A. Einstein, N. Bohr, E. Schrödinger, W. Heisenberg, P. Dirac, J. von Neumann, M. Born, P. Jordan, L. de Broglie, A. Sommerfeld) developed the concept of quantum mechanics, which we use nowadays to predict the outcome of experiments and to understand the foundational concepts of Nature. The experiments in the field of quantum mechanics were (and still are) benefiting from the technological development of classical and semi-classical technologies like electronics and lasers. This technological development was responsible that many experiments in the field of quantum mechanics

became real. Several (famous) physicists were however uncomfortable with the predictions of quantum mechanics, especially it is stochastic nature. For example, to solve this apparent issue, Albert Einstein proposed that quantum mechanics is incomplete, and that there exist hidden variables (that we may never be able to access) that explain all measurement outcomes. At this point, it seems obviously hard to even imagine an experiment that could make the distinction between the statements "quantum mechanics is complete" and "quantum mechanics is essentially classical mechanics with additional hidden variables". Luckily, in 1964, a young physicist called John Steward Bell presented a theorem called "Bell's theorem" that explains an important distinction between the quantum and classical mechanics, which is mainly driven by the concept of quantum entanglement (Bell, 1964). This theorem opened the possibility to perform an experiment in the laboratory to test which of the two above statements is actually correct. Interestingly, it took another 50 years until experimentalists finally managed to perform a complete (loophole - free) Bell test, concluding that quantum mechanics is indeed a complete theory (Hensen et al., 2015; Giustina et al., 2015; Shalm et al., 2015). One of the first quantum experiments that gained the attention of a broad audience towards quantum mechanics was in the late nineties (1997). The group of S. Popescu and A. Zeillinger showed that quantum teleportation can be realized (Boschi et al., 1998; Bouwmeester et al., 1997). Their experiment represent a big breakthrough in the community because it showed that complex quantum mechanics experiments can be realized. The experiment of quantum teleportation is based on the resource of quantum entanglement, in this case pairs of entangled photons. The unique concept of entanglement is the key ingredient for many applications in the field of quantum mechanics and can only be found in the world of quantum mechanics. An example of entanglement is if one conducts a measurement on two qubits (let's assume photons and also they are already entangled). If the result of the measurement (let's assume the measurement is done in Stuttgart, Germany) of one qubit is known, then the state of the second qubit is immediately known (even if the second qubit is anywhere else in the universe).
Since the 1980s, the field of quantum mechanics is developing very quickly. The field is structured in the following sub-topics:

Quantum Communication: The research field of quantum communication is mainly driven by the idea of building a quantum network (quantum nodes, quantum repeaters, quantum resource distribution, quantum entanglement, quantum cryptography). A quantum network is very similar to a classical network. In both networks, photons are used to modulate and transport information. The big difference between both of them is the possibility of entanglement distribution in a quantum network. The amount of submitted information in a quantum network scales with 2^N where N is the Hilbert space dimension. The information in a classical network scales with N^2 with N number of bits. This indicates that the capability of a quantum network will overcome a classical one for large N. In addition, provably secure communication can only be realized in quantum networks.

Quantum Computing: Various companies like IBM and Google are working on the realization of a quantum computer based on superconducting quantum interference devices (SQUID) (You, Tsai, and Nori, 2002). Quantum computer are capable to solve complex problems with specialized algorithms (Deutsch, 1985; Raussendorf and Briegel, 2001). Quantum computers can efficiently solve problems of a class called bounded error, quantum, polynomial time (BQP). More precisely, quantum computers are expected to be restricted to P problems. P problems are associated with a set of counting problems (Shor, 1999; Deutsch and Jozsa, 1992).

Quantum Simulation: Simulation of quantum systems represents a computationally hard problem for classical computers. However, already in 1982, Richard Feynman proposed that it might be much more efficient to simulate the quantum interactions of complex systems using another (well controlled) quantum system (Feynman, 1982). The simulation of tailored drugs and their effects are hardly possible to simulate with classical algorithm. Most of the effects are driven by quantum mechanical interactions. Various companies are planing to use quantum algorithms to solve human medical problems (Zetter and Banyard, 2002). This field is especially important for physicists to understand the principle of Nature. Interactions between large numbers of atoms (ions, photons, molecules) can only be simulated with quantum algorithms.

Quantum Sensing: Nearly all electronics devices are nowadays using sensors during their operations. The requirements of sensors are normally defined by increased sensitivity, smaller size and less power consumption. Classical technology is suffering from the limitation of sensitivity and sensor size. A new approach to become more sensitive is a quantum sensor. One of the most developed quantum sensors is the NV-centre in diamond (Doherty et al., 2013). The NV-centre is a quantum defect in diamond and it consists of a vacancy and a nearest neighbor nitrogen atom, which substitutes a carbon atom (Coulson and Kearsley, 1957; Wrachtrup et al., 1993). The NV-centre in diamond is a sensitive magnetic field sensor (< 1 pT$/\sqrt{Hz}$, (Wolf et al., 2015)) and electric field sensor (Dolde et al., 2011). Due to the atomic size of the NV-centre, the spatial resolution is < 1 nm. The NV-centre can also be operated at ambient temperature. Recent progress in the field showed that the NV-centre can also be used as a nano NMR sensor (Aslam et al., 2017). This opens a new path for medical applications, autonomous transportation and all other fields where high sensitivity and atomic size resolution is needed.

The topic of my thesis is settled in the field of developing novel platforms and technologies for quantum information. The vision of my thesis topic was to identify a quantum system where the realization of a functional quantum network in solids would become feasible. When I started my thesis in 2015, the first experiments were published in the group of Ronald Henson on the realization of a quantum network (Childress and Hanson, 2013). The group of Ronald Henson was using the NV-centre in diamond to show that they were able to entangle two NV-centres which were separated by 1.3 km (Hensen et al.,

2015). This was a mayor step forward to realize a two node quantum network. We showed in the meanwhile in our group (Yang et al., 2016) that we can add to every node a long lived quantum memory which enhances the functionality of the network. The problems of the NV-centre is that the total amount of the photons in the zero phonon line (ZPL) is limited to ≈ 3-4 % of the all emitted photons. A second disadvantage for quantum information applications is the high electric field sensitivity of the NV-centre. Resonant excitation is based on setting the energy of the excitation laser on the energy difference between the ground and excited states of the NV-centre. Electric fields will continuously change the energy between the ground and excited states, which makes resonant excitation challenging. Another effect that makes experiments with the NV-centre challenging are different charge states. An electron of the NV-centre can be ionized to the conduction band. The ionization effect changes the charge state from NV^- to NV^0. The change of the charge state influences the total spin and the emission wavelength of the NV-centre. To solve these problems, multiple system sanity-checks have to be implemented. These sanity-checks are very time consuming and decrease the rate of the network dramatically. The research community realized these drawbacks and was looking for new quantum defects without these disadvantages. The group of Prof. Fedor Jelezko in Ulm showed that a new group of quantum defects may solve these problems, called inversion symmetry defects (Rogers et al., 2014b). Most of the emitted photons of these defects (≈ 60-90 %) are guided into the ZPL (Green et al., 2017; Iwasaki et al., 2015; Iwasaki et al., 2017). The inversion symmetry cancels the influence of electric fields. The optical properties are spectrally stable due to this effect (Gali and Maze, 2013). This makes the category of inversion symmetry defects nearly perfect optical quantum defects for network applications. The disadvantage of these quantum defects is the short spin coherence, which is mandatory for a quantum network. The spin coherence is decreased in inversion symmetry quantum defects due to scattering of phonons between the ground state spin levels (Rogers et al., 2014a). There were two ideas in the research community to overcome this issue. The first idea was to build a structure that suppresses the phonon scattering (Sukachev et al., 2017). It turned out that such a structure would be very demanding in terms of fabrication accuracy. The second option is to cool down the sample mK temperatures to freeze out phonons. This has been demonstrated by various groups and they showed an increase in spin coherence (Sukachev et al., 2017). The disadvantage of this method is the high price and huge space needed for the equipment, especially when considering the installation of a repeater node every 10 - 100 km. An important aspect for a real realization of a quantum network is the needed space and equipment price. In the meanwhile the research community was looking for alternative host materials and quantum defects in which the optical properties are comparable with inversion symmetry defects and the spin properties with the NV-centre in diamond. In 2015, the group of David Awschalom showed that they can isolate and excite single DiVacancy centres in 4H-SiC (Christle et al., 2017). At the same time, our group in Stuttgart also showed that we can create and isolate single silicon vacancy V_2 quantum defects in 4H-SiC (Widmann and Lee, 2015). The level structure of the DiVacancy centre is very similar to the NV-centre in diamond. Thus, it also brings the same drawbacks as the

NV-center in diamond. The silicon vacancy V_2 centre in 4H-SiC shows a spin signal and good coherence properties. On the other hand, the results showed that the spin contrast (ODMR) of the silicon vacancy V_2 centre is < 1 % (NV-centre ≈ 30 %) and the countrates are only ≈ 30 kcnts/s. At the begin of my thesis, we started to investigate the silicon vacancy V_1 centre in 4H-SiC at 4 K to analyze the properties of this quantum defect. The first measurements on silicon vacancy V_1 ensembles showed that resonant excitation at 4 K leads to a strong increase of the ODMR contrast (≈ 100 %). I also showed that the silicon vacancy V_1 in 4H-SiC can be coherently manipulated and has a long spin coherence time (Nagy et al., 2018b). The first measurements on a single silicon vacancy V_1 centre in 4H-SiC showed that roughly 40 % of the emitted photons are guided into the ZPL, which is a factor of 10 more as for the NV-centre in diamond. The first PLE measurement showed that the optical transitions are as stable as for the inversion symmetry defects (Nagy et al., 2018a). Also, spin coherence measurements on single silicon vacancy V_1 centres in 4H-SiC showed an extremely long spin coherence time T_2 of ≈ 1 ms. I figured out during my research that the silicon vacancy V_1 centre in 4H-SiC shares many key spin properties of the NV-centre in diamond and the optical properties of the inversion symmetry defects (Nagy et al., 2018a). These properties make the silicon vacancy V_1 centre in 4H-SiC an ideal candidate for quantum information applications.

My thesis shows the first measurements on single silicon vacancy V_1 centre in 4H-SiC. The results of the measurements are presented in this thesis. The thesis is structured in 6 Chapters and Appendix:

- **Chapter 1:** Introduction into the topic.
- **Chapter 2:** Basic concepts of structure and defect creation in SiC.
- **Chapter 3:** Ensemble measurements of silicon vacancy V_1 centres in 4H-SiC.
- **Chapter 4:** Resonant excitation studies on single silicon vacancy V_1 centres in 4H-SiC.
- **Chapter 5:** Indistinguishable properties of single silicon vacancy V_1 centres in 4H-SiC.
- **Chapter 6:** Summary, conclusion and outlook.

CHAPTER 2

Silicon Carbide as Host Material for Quantum Defects

Silicon carbide (SiC) is a IV-IV material compound. It offers unique chemical and physical properties. The strong binding energy between the silicon (Si) and carbon (C) atoms (4.6 eV) results in a very high hardness and chemical inertness. The strong bonds between Si and C atoms leads to a large bandgap of SiC, between 2.3 - 3.3 eV (depending on the polytype and crystal structure). The electronic properties of SiC show a ten times higher critical electric field strength than Si. Additionally, SiC provides also a three times higher thermal conductivity as Si, which makes the material especially attractive for high power electronic devices (Bhatnagar and Baliga, 1993; Cooperjr and Agarwal, 2002; Kimoto and Cooper, 2014; Kimoto, 2015). Wide bandgap SiC semiconductor devices can be operated at temperatures of 300 °C and above (depending on the polytype), which makes the materials interesting for applications under difficult thermal conditions. A specialty under various wide bandgap semiconductors is that SiC can be easily doped either n-type or p-type (Demichelis, Pirri, and Tresso, 1992). In the recent years the semiconductor industry has made remarkable efforts using SiC for high power devices and energy saving by using Schottky barrier diodes and power MOSFETs (Chaussende and Ohtani, 2019). These devices are used in air conditioners, photovoltaic converters, industrial motor control and railcars (Zhang et al., 2019; Leblebici et al., 2019). The challenging part of SiC is the growth process of large SiC wafers. The demand of high physical and chemical stability during the growing process makes it hard to grow large SiC wafers with high quality (Zhao and Wu, 2019). Another disadvantage and advantage of SiC is the existence of various SiC crystallographic structures with different stacking sequences (known in the literature as polytypism (Kimoto, 2019)). Polytypism of SiC offers an opportunity for tailoring a material with purpose designed physical and chemical properties for various applications. Producing various polytypes with high quality stays a difficult task during the growing process (Kimoto, 2019).

Another aspect getting more prominent in the last couple of years is the use of silicon carbide as host for spin active quantum defects (F Koehl et al., 2011). The reason for these

aspirations are the physical properties of SiC. The three relevant host material properties for spin active quantum defects are a wide bandgap material, low spin-orbit splitting and stable spinless nuclear isotopes (Awschalom, 2019). A wide bandgap material is mandatory for quantum defect applications. The electronic states which result from the bonds need to be within the forbidden bandgap. If the bandgap is too small or the states are too close to the valence or conductance band, an electronic transition can be triggered by thermal energy. Due to the wide bandgap of 4H-SiC ≈ 3.2 eV, these effects are neglectable. In order to achieve long spin coherence times, an isolated highly localized wavefunction is mandatory (Doherty et al., 2013). To avoid decoherence through spin flip of the defects states, a low spin-orbit coupling is required. The calculated spin-orbit coupling of SiC can be seen in Table 2.1. Additionally, to increase the spin coherence time of a quantum defect, one needs a density of spinless nuclei (Weber et al., 2010). Silicon carbide offers through ^{28}Si and ^{12}C an isotopically stable purified environment for quantum defects to achieve long spin coherence. As it can be seen in Table 2.1, SiC is an ideal host for spin active quantum defects.

Material	Bandgap (eV)	Spin-Orbit Splitting	Stable Spinless Nuclear Isotope
3C-SiC	2.2	10.0	Yes
4H-SiC	3.2 (Neudeck, 1995)	6.8	Yes
6H-SiC	2.86	7.1	Yes
Diamond	5.5	6	Yes
GaN	3.44	17	No
AlN	6.13	36 (Silveira et al., 2005)	No
ZnO	3.3 (Srikant and Clarke, 1998)	-3.5	Yes

TABLE 2.1: Properties of silicon carbide as host material for quantum defects (Bar-Gill et al., 2013). The mainly used polytype 4H-SiC is highlighted in red. The spin-orbit coupling is measured at low temperature, (Weber et al., 2010).

2.1 Silicon Carbide Crystal Structures and Polytypes

In SiC, C and Si atoms are tetrahedrally bonded by covalent bonds and sharing electron pairs in sp^3-hybrid orbitals. The pairs of Si-C (tetrahedra) can occupy different positions, which will be named A, B and C as shown in Fig. 2.1, each layer contains tetrahedra in one position. There are more than 200 different stacking structures 'polytypes' known in SiC. The lattice structure of the three mainly used polytypes can be seen in Fig. 2.1. In the literature, 3C-SiC (zincblende) is often referred to β-SiC and 4H & 6H as α-SiC (Kimoto, 2019). It is still subject of ongoing research why SiC can exist in so many polytypes. It is suspected that the intermediate ionicity of SiC (according to Pauling's definition 11 %) is a possible reason for the origin of the polytypism in SiC (Heine, Cheng, and Needs, 1991; Matsunami and Kimoto, 1997). Ab initio calculations show that the energy difference among different

polytypes in SiC is extrem small (1 meV/atom) (Ito et al., 2011; Mercier and Nishizawa, 2012). Another important factor is the stability and the nucleation probability of SiC polytypes. Experiments showed that theses properties strongly depend on the temperature. A very well known example is 3C-SiC, which is not stable and transforms into its hexagonal structure at high temperature (Yoo and Matsunami, 1991). A similar effect can also be observed in 6H-SiC. These kinds of instabilities make the growing process of big wafers for 3C-SiC very challenging. A big advantage of 3C-SiC is that it can be heteroepitaxially grown on Si substrates for device fabrication (Roschke and Schwierz, 2001). Due to the case that all polytypes of SiC consist of similar Si-C bonds, the mechanical (hardness) and thermal properties (thermal conductivity) are in general very similar (Bhatnagar and Baliga, 1993; Kildemo, 2003). An important case is the electronic structure in different SiC polytypes. 3C (zincblende), 4H (hexagonal with a hexagonality of 50 %) and 6H (hexagonal with a hexagonality of 33 %) have different lattice structures (see Fig. 2.1). This results in significantly different bandgab energies. This property indicates that it is crucial for quantum application to grow only single crystal polytypes. The best studied and widely used polytype yet is 4H-SiC, which shows the best lattice quality for quantum applications (Christle et al., 2017).

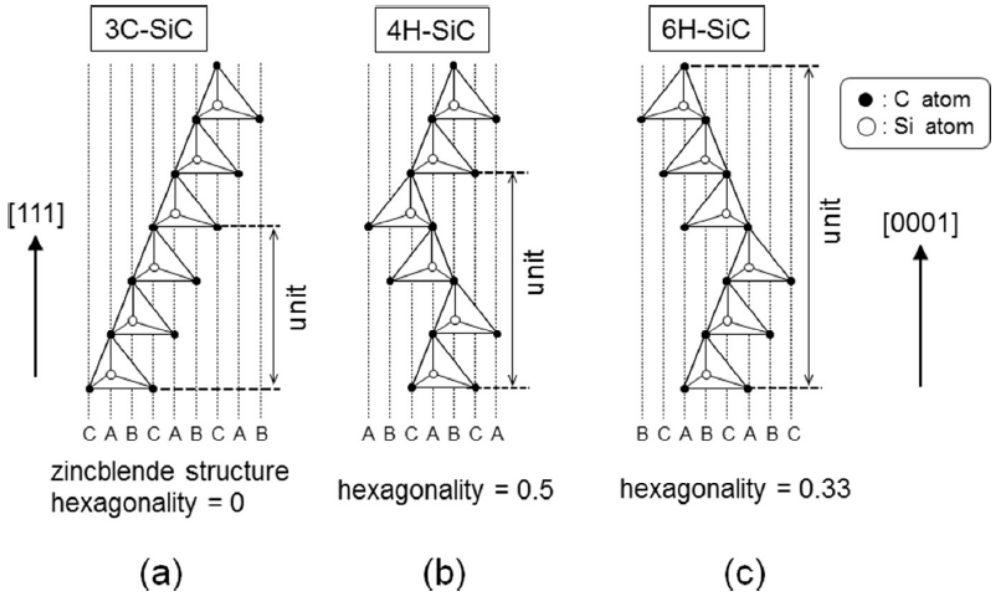

FIGURE 2.1: Silicon carbide stacking sequence of the most common used polytypes (a) 3C-SiC (zincblende), (b) 4H-SiC (hexagonal) and (c) 6H-SiC (hexagonal) (Fig. from (Kimoto, 2016)).

2.2 Silicon Carbide Material Growth Process

The state of the art technique for SiC bulk growth is the seeded sublimation method (Tairov and Tsvetkov, 1978; Tairov and Tsvetkov, 1981). Fig 2.2 shows a schematic of a crucible, which is used for seeded sublimation growth of SiC (Glass et al., 1997; Takahashi and

Ohtani, 1997; Chaussende, Wellmann, and Pons, 2007). The source species of SiC (powder or sintred polycrystalline SiC) is placed at the bottom of the graphite crucible. A SiC crystal seed is placed at the top near the seed. The total distance between the source and the seed is roughly 20 to 40 mm. To achieve high temperatures at the source, a radio frequency induction or resistive heating is used. The usual temperature during the growing process is 2300 - 2400°C. Additionally, the cruciable is thermally insulated by porous graphite. The standard seed temperature is normally fixed at about 50 - 100°C below the source temperature. The temperature gradient between the source and the seed causes sublimation of SiC condensates and crystallization at the seed. The pressure is normally kept low to enhance the mass transport from the source to the seed (Kimoto, 2016). Ar or He gas of high purity is employed during the growing process. The determination of the grow rate in sublimation growth is determined by the sublimation rate (flux of the source) and the mass transport efficiency. In more detail the sublimation rate is a function of the source

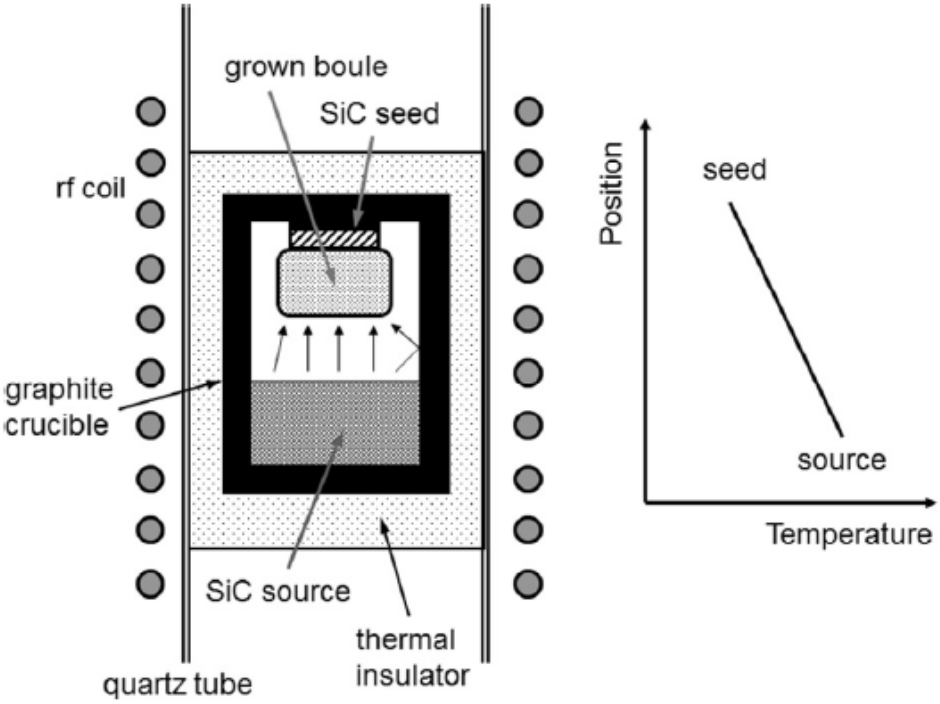

FIGURE 2.2: Growth chamber for sublimation growth of SiC. On the right side of the figure is an illustration of the temperature difference between the source and seeds. (Fig. from (Kimoto, 2016)).

temperature (Matsunami and Kimoto, 1997) and the mass transport efficiency which depends on the growth pressure, temperature gradient and the distance between the seed and source (Heine, Cheng, and Needs, 1991). The mass transport is described by a diffusion process, due to this behavior the growth rate is almost inversely proportional to the growth pressure. The concentration for the diffusion process is mainly determined by the difference in temperature between the source and seed. Any temperature fluctuations and changes in pressure reduces the quality of the growth crystal. If we look in more detail

into the process towards quantum application during changes in temperature and pressure fluctuations is the formation of so called micro defects. These created defects are, in first approximation, no quantum defects. On the grain boundaries of these classical defects, quantum defects can occur due to the missing atom at a lattice site. These sources of defects are known as potential decoherence sources in SiC. In the state of the art growing chambers the speed of the growth process is ≈ 0.3 - 0.8 mm/h at several hundres Pa or lower (Kimoto, 2016). If the growth rate is increased, also the probability of micro defects is enhanced.

Layer	Isotopically Purified	Free Carrier Concentration	Nitrogen Donors	Carbon Vacancies	Minority Carrier Lifetime	Density Electron Traps
CVD 100 μm	Yes $^{28}Si > 99.85\%$ and $^{12}C > 99.98\%$	$6 \cdot 10^{13} cm^{-3}$	$3.5 \cdot 10^{13} cm^{-3}$	$1 \cdot 10^{13} cm^{-3}$	$1.2 \mu s$	$\approx 5 \cdot 10^{12} cm^{-3}$

TABLE 2.2: Parameters of the used sample in chapter 4. These parameters are optimized for single defect studies.

2.3 Quantum Defects inside Silicon Carbide

A quantum defect inside solids usually induces a symmetry break on a localized position inside the lattice (M. Stoneham and Smoluchowski, 1976). The reason for a symmetry break can be, in the most easiest scenario, a vacancy created by kicking out one atom from its lattice site. In the case of silicon carbide, either a silicon or carbon atom can be kicked out. The resulting quantum defects are referred in the literature as carbon vacancy V_C or silicon vacancy V_{Si} centre (Sörman et al., 2000; Son et al., 1999). Due to the polytypism

Defect	ZPL Energy (eV)	ZPL Wavelength (nm)
$V_{Si}(V_1)$	1.444 & 1.438	858 & 861
$V_{Si}(V_2)$	1.352	916
$V_C - V_{Si}$	1.056	1173
$V_C - V_{Si}$	1.053	1176
$V_C - V_{Si}$	1.050	1179
$V_C - V_{Si}$	1.013	1223
$V_C - V_{Si}$	1.009	1227
$V_C - V_{Si}$	0.997	1242

TABLE 2.3: Quantum defects inside 4H-SiC. Wavelength of the zero phonon line (ZPL) of silicon vacancy centre V_{Si} and DiVacancy centre $V_C - V_{Si}$. The origin of two different silicon vacancy centre in 4H-SiC is the position of the vacancy either on the hexagonal or quasi-cubic lattice site respective V_1 and V_2. The DiVacancy centre can occour in many different basel configurations inside the 4H-SiC lattice as it can be seen in Fig. 2.3.

in SiC, optical and spin properties of the created defect centres can be quite different for various polytypes (due to different lattice configurations). The 4H-SiC polytype is mainly used for quantum applications due to his high lattice quality (the crystal of 4H-SiC can be seen in Fig. 3.1). Due to the stacking fault of silicon carbide, a silicon or carbon vacancy can occur in a cubic or lattice site. The literature refers to a silicon vacancy at a hexagonal lattice site as V_1 and at a cubic lattice site as V_2 centre. A spectrum of the V_1 and V_2 centre in 4H-SiC can be seen in Fig. 3.6 (b). Other defects which are naturally created in silicon carbide are antisite defects (Iwamoto and G. Svensson, 2015). An antisite defect in 4H-SiC can occur when a silicon and carbon atom are exchanging their position inside the lattice C_{Si} and Si_C (Iwamoto and G. Svensson, 2015). Additionally, also interstitial defects are naturally formed in SiC where either a silicon or carbon atom is located on a position between lattice sites C_i and Si_C (Gao and Weber, 2002). Another important

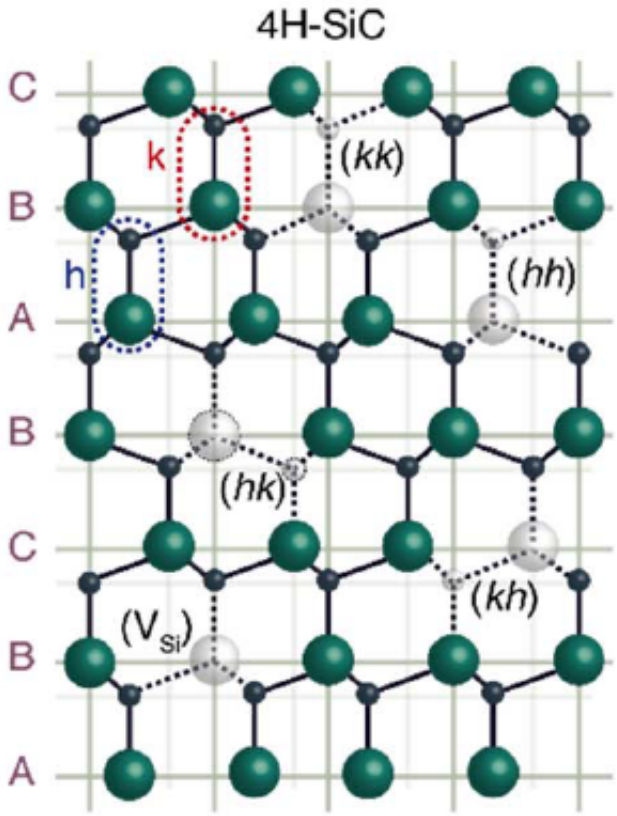

FIGURE 2.3: Point defects in 4H-SiC. The green color indicates silicon and black carbon atoms. Single missing atoms show the appearance of either silicon or carbon vacancy centre. Two vacancies next to each other form a DiVacancy centre. (Fig. from (Heremans, Yale, and Awschalom, 2016))

defect type composition inside SiC, which can be natural created, is a DiVacancy centre $V_C - V_{Si}$. A DiVacancy is a combination of a silicon and carbon vacancy next to each other inside the lattice, as it can be seen in Fig. 2.3. Due to the combination of two vacancy centres next to each other, the DiVacancy can exists in different lattice site variations, as it can be seen in Fig. 2.3 (N. T. Son, 2006; Drabold, 2007), similar to the nitrogen vacancy

centre in diamond (Doherty et al., 2013). Additionally, a second class of defect centres can be formed by implantation or diffusion of impurities (dopands) inside silicon carbide (Oliveira et al., 2017). This field is mainly driven by density function theory (DFT) simulations predicting the optical and spin properties of new defect centres. Recent progress on implanting various impurities inside SiC shows the formation of Cr^{4+} centre (Koehl et al., 2017) and nitrogen vacancy centre in 4H-SiC (Csóré et al., 2017). The best studied defects for quantum applications in silicon carbide are the silicon vacancy centre and DiVacancy in 4H-SiC (Widmann and Lee, 2015; Nagy et al., 2018b; Christle et al., 2017; F Koehl et al., 2011). This thesis will mainly focus on the silicon vacancy V_1 centre in 4H-SiC.

2.4 Creation of Single Silicon Vacancy Centres in 4H-SiC

For the creation of a single silicon vacancy centre, a single silicon atom needs to be pushed out of his crystal lattice site in 4H-SiC. To realize the creation of a single silicon vacancy centre, several technological methods have been established. The most common and developed methods are electron irradiation, ion beam and laser writing (Kraus et al., 2017; Wang et al., 2017; Castelletto et al., 2018; Yu-Chen Chen, 2018). Electron irradiation is a very well known method from the nitrogen vacancy community, which has been adapted for silicon carbide defect creation. Silicon vacancy centres can be created depending on the electron dose and energy of the irradiated electrons. Some basic parameters for electron irradiation can be seen in Table 2.4. The disadvantage of electron irradiation is the non deterministic positioning of created silicon vacancy centre. Another method is ion implantation (Kraus et al., 2017; Wang et al., 2017). Recent progress in the community showed deterministic creation of silicon vacancy centre with H, C, Si and He ions (Kraus et al., 2017; Wang et al., 2017). The created silicon vacancy centre can be very precisely positioned in x-y direction by ion implantation. Note that ion beam implantation is limited to near-surface defect generation. Even at high energies, only a few 100 nm implantation depth can be reached. Another recently investigated method is laser induced creation of silicon vacancy centre. For this method, femto-second laser pulses with an average energy of a nanojoule focused on a position inside the silicon carbide lattice will form single silicon vacancy centre (Castelletto et al., 2018; Yu-Chen Chen, 2018). All methods proved

Number of Defects	Electron Energy [MeV]	Dose [Electrons/cm^{-2}]
Ensemble of V_{Si}	2	$>1 \cdot 10^{14}$
Single V_{Si}	2	$1 \cdot 10^{12}$

TABLE 2.4: Parameters for electron irradiation. The irradiation dose of electrons determines the created number of silicon vacancy centres. An electron irradiation dose of $>1 \cdot 10^{14}$ elecrons/cm^{-2} will create a very diluted silicon vacancy ensemble. At an irradiation dose of $1 \cdot 10^{12}$ elecrons/cm^{-2} single silicon vacancy centre will be created with an average distance of 5 μm between the centres. A detailed analysis of the creation of silicon vacancy centre on various doses of electron irradiation can be seen in (Widmann and Lee, 2015).

the capability for the creation of single silicon vacancy centres. Another important aspect are the spin properties of the created silicon vacancy centres. The spin coherence properties of the silicon vacancy centre depends on the local lattice quality, especially how many paramagnetic impurities are close to the silicon vacancy centre (Balasubramanian, 2009; Bar-Gill et al., 2013). All presented methods in this section do not only create silicon vacancy centres, but also carbon vacancy centres (Son, Hai, and Janzén, 2001). Due to the different mass of Si $\approx 4.66 \cdot 10^{-23}$ g and C $\approx 1.99 \cdot 10^{-23}$ g, the probability of carbon vacancy generation is larger than for silicon vacancy centres. This indicates that the presented methods may have a different impact on the spin coherence time T_2 of the silicon vacancy centre. Table 2.5 shows an overview of all three methods. To date, the spin co-

Method	Single Defects	Spin Coherence T_2 [ms]	Deterministic Positioning
Electron irradiation	Yes	≈ 1 (Fig. 4.9 (a))	No
Ion implantation	Yes	Not measured	Yes
Laser beam writing	Yes	Not measured	Yes

TABLE 2.5: Overview of different defect creation methods. All three methods showed the capability to create single defects. The spin coherence of single defects was only measured with electron irradiation creation methods. Electron irradiation does not deterministically create single defects. Ion implantation creates single defects with good spatial resolution in x, y, and z. But the depth of defect creation is limited to a few hundred nanometers. Laser writing is also capable of creating spatially localized defects. The z resolution is limited to a couple of μm.

herence time T_2 is only analyzed for single defects created with electron irradiation. Up to now it is unknown if other methods will show similar results to electron irradiation. All measurements in this thesis were conducted on silicon vacancy centres created by electron irradiation.

Another important aspect for the creation of quantum defects is the so called formation energy. This energy indicates how much energy is needed to create one desired quantum defect inside 4H-SiC. A summary of the formation energies of relevant quantum defects inside 4H-SiC can be seen in Table 2.6. The formation energies of the silicon vacancy centre $V_{Si}(k)$ and $V_{Si}(h)$ are respectively 7.16 eV and 7.10 eV. The small difference in energy results from different lattice site position. The two values also indicate that it is more likely to create silicon vacancy centre on the hexagonal than on the cubic lattice site. The most important information of Table 2.6 is that it is much more likely to create $C_{Si}(k,h)$ in comparison to $V_{Si}(k,h)$. The formation energy of $C_{Si}(h)$ is a factor of ≈ 2.68 lower as for $V_{Si}(h)$. As a consequence, more $C_{Si}(k,h)$ will be created than $V_{Si}(h)$.

Another aspect in the creation and stabilization of quantum defects inside 4H-SiC is the engineering of the Fermi level. If I take the material properties of the 4H-SiC CVD sample from Table 2.2 with $< 3.5 \cdot 10^{13}$ cm^{-3} N, 10^{12}-10^{13} cm^{-3} V_C before irradiation and $\approx 1 \cdot 10^{13}$ cm^{-3} B, the Fermi level is roughly 1.5 eV below the conduction band (see Fig. 2.4). This indicates that the V_{Si} is negatively charged. This Fermi level was used during single studies.

Quantum Defects	Formation Energy [eV]
$V_{Si}(k)$	7.16
$V_{Si}(h)$	7.10
$Si_i(k)$	12.46
$Si_i(h)$	10.87
$Si_c(k)$	4.58
$Si_c(h)$	4.63
$V_c(k)$	4.84
$V_c(k)$	4.88
$C_{i,split}(k)$	6.32
$C_{i,split}(h)$	6.21
$C_{Si}(k)$	2.61
$C_{Si}(h)$	2.65

TABLE 2.6: Formation energy of quantum defects inside 4H-SiC. This illustrates the energy needed to create defects inside 4H-SiC (Kobayashi et al., 2019).

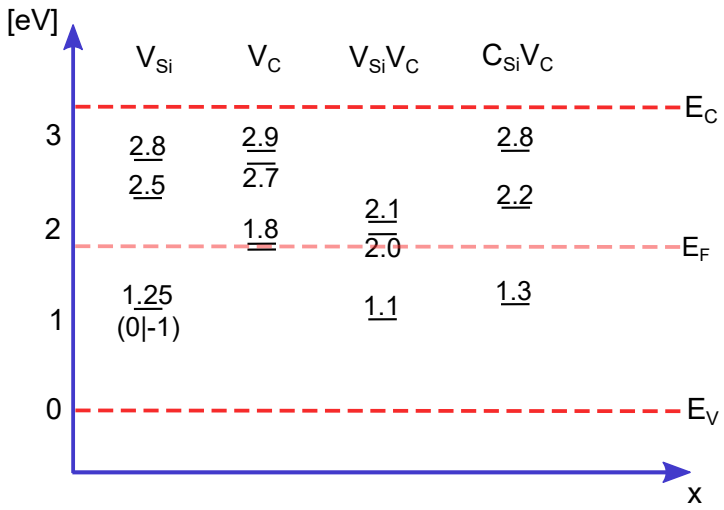

FIGURE 2.4: The position of the Fermi level determines the charge state and charge stability of quantum defects inside 4H-SiC. (Kobayashi et al., 2019)

2.5 Heteronuclear Spin Bath

Silicon carbide consists of Si and C atoms. The natural abundance of nuclear spin active isotopes ^{29}Si (p_{Si} = 4.7 %) and ^{13}C (p_C = 1.1 %) in SiC as a quantum material is very high. The spin coherence time T_2 is limited in pure silicon carbide samples (without taking other defect centres as decoherence sources into account) by spin flip-flops of ^{29}Si and ^{13}C isotopes. Diamond, which hosts nitrogen vacancy centres has in comparison a

natural abundance of ^{13}C (p_C = 1.1 %). The resulting spin coherence time T_2 for nitrogen vacancy centre is $\approx 10^2$ μs in samples with naturally abundant isotopes (Gruber et al., 1997) and even longer in isotopically purified samples (Balasubramanian, 2009; Bar-Gill et al., 2013). In silicon carbide the natural abundance of ^{29}Si is four times higher than ^{13}C, which may make silicon carbide not a suitable host material for quantum defects. But surprisingly, measurements of the spin coherence time T_2 in silicon carbide on silicon vacancy centre showed similar results as the nitrogen vacancy centre in diamond (Widmann and Lee, 2015; Nagy et al., 2018b). The reason for this behavior can be found in the vol-

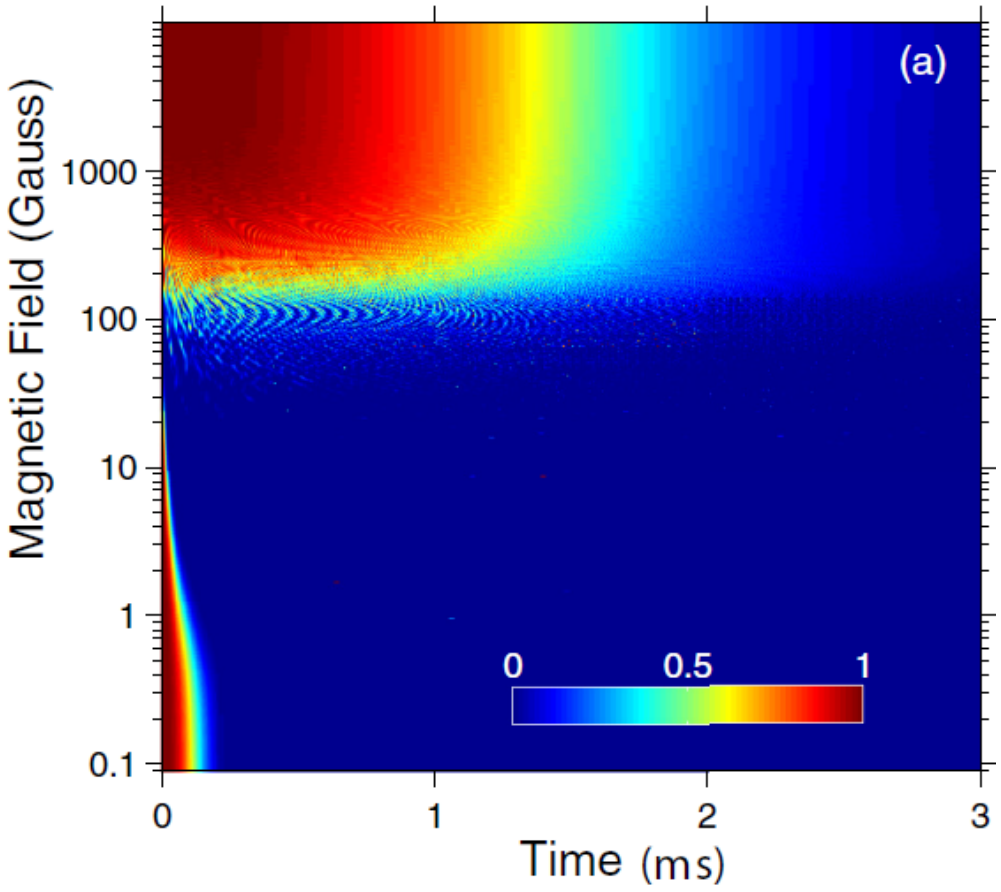

FIGURE 2.5: Hahn echo simulation of the V_{Si} centre in 4H-SiC. The spin coherence between simulated $|+\frac{1}{2}\rangle$ and $|+\frac{3}{2}\rangle$ states depending on the free evolution time and applied magnetic field B_0. This Fig. is from (Yang et al., 2014).

ume expansion of the crystal lattice in silicon carbide (Ivády et al., 2017). Silicon carbide has a lower density within the unit cell in comparison to diamond but the bonding length between the atoms is longer. The C-Si bond length is 1.89 $\AA$ in SiC and thus longer than the C-C 1.54 $\AA$ in diamond. This means that the volume density of nuclear spins in SiC is reduced by a factor of $(1.89/1.54)^3 \approx 1.8$ in comparison to diamond. Due to the lower density of nuclear spins, the magnetic noise created by nuclear spins in silicon carbide is lower. A second reason for the high spin coherence times of silicon vacancy centre in SiC

can be found in the different gyromagnetic ratio between ^{29}Si and ^{13}C. The gyromagentic factors for ^{13}C and ^{29}Si are respectively γ_C = 6.73 rad s^{-1}T^{-1} and γ_{Si} = -5.32 rad s^{-1}T^{-1}. Due to the four times higher natural abundance of ^{29}Si, 80 % of all nuclear spins in SiC show a lower gyromagnetic ratio. As a result, compared to ^{13}C they produce ($|\gamma_C/\gamma Si| \approx$ 1.3) weaker magnetic fluctuations as in diamond. The third reason can now be found if a magnetic field is applied. The difference in the gyromagnetic ratios between ^{29}Si and ^{13}C leads to a different nuclear Zeeman energy splitting (Jelezko et al., 2004). The Zeeman splitting between ^{29}Si and ^{13}C is $|\gamma_C| - |\gamma_{Si}| = 2\,\pi \cdot$ 0.2 kHz/G. If a magnetic field is applied in SiC, the Zeeman energy scales differently between ^{29}Si and ^{13}C by $2\pi \cdot 0.2$ kHz/G. It has been shown that if a magnetic field is applied with more than B > 300 G, the spin coherence time T_2 for silicon vacancy centres in SiC is longer than for nitrogen vacancy centres in diamond (Yang et al., 2014). The physical effect for the increasing spin decoherence is due to the suppression of C-Si spin flip-flop processes. With stronger magnetic field the energy difference becomes large enough that ^{29}Si and ^{13}C form a homonuclear spin bath. The effect on spin coherence T_2 with magnetic fields can be seen in Fig. 3.19 (c). The increase of the magnetic field strength from B_0 = 60 G to B_0 = 1000 G leads to an increase of spin coherence T_2 by a factor of ten. This behavior is simulated in Fig. 2.5. The figure shows Hahn-Echo measurements with different magnetic field strengths. It can be seen that the spin coherence T_2 can be significantly increased with higher magnetic fields.

CHAPTER 3

Silicon Vacancy Centre V_{Si} Ensembles in Silicon Carbide

Parts of Chapter 3 are published in Roland Nagy et al. Phys. Rev. Applied 9, 034022.

3.1 Silicon Vacancy Centre in 4H-SiC

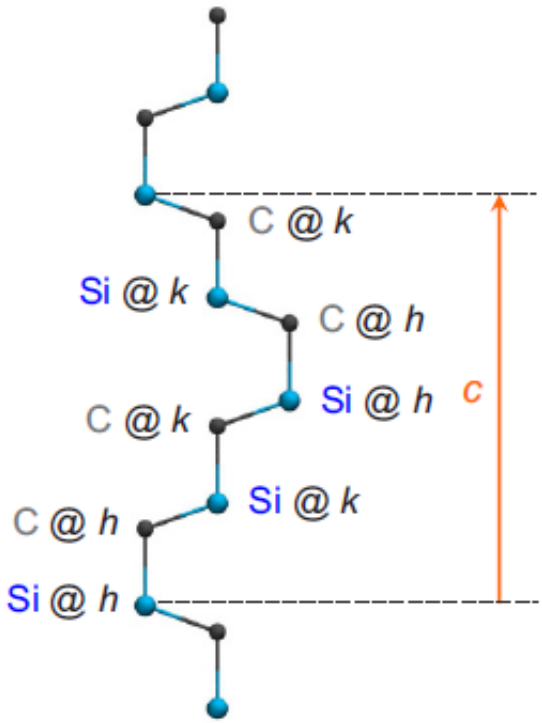

FIGURE 3.1: 4H-SiC crystal structure with hexagonal V_1 and quasi-cubic lattice site V_2. The orange arrow c denots the direction of the quantization axis.(Ivády et al., 2017)

The isolated silicon vacancy centre in 4H-SiC is one of the intrinsic defects inside the lattice structure (see Fig. 3.1). The hexagonal lattice structure of 4H-SiC hosts two inequivalent silicon lattice sites, one hexagonal (h) and one quasi-cubic (c or k), see Fig. 3.2. The defect centre related to the hexagonal lattice site is known as V_1 and the quasi-cubic

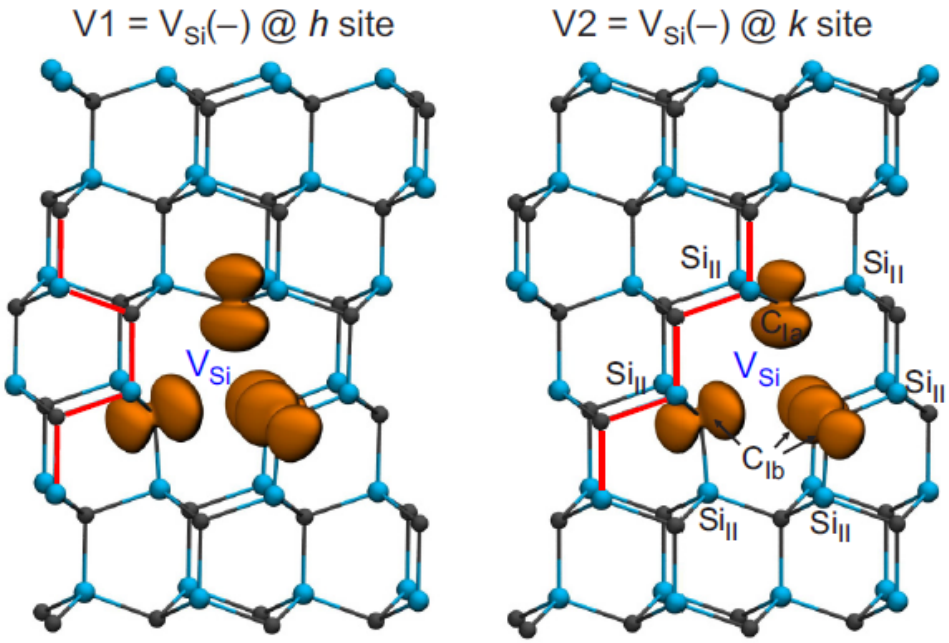

FIGURE 3.2: Inequivalent silicon vacancy centre locations in 4H-SiC. A silicon vacancy centre at the hexagonal (h) lattice site is known as V_1 (left graph) and on a cubic lattice site (c) V_2 (right graph). (Ivády et al., 2017).

defect as V_2 (a spectrum of both defects can be seen in Fig. 3.6). Both defect centres V_1 and V_2 have different charge states within the band-gap (Szász et al., 2015; Mizuochi et al., 2005; Son, Hai, and Janzén, 2001; Lingner et al., 2001), and are created by removing one silicon atom from his lattice position either on the hexagonal or quasi-cubic lattice site. The quantization axis of a silicon vacancy centre in 4H-SiC (Fig. 3.1) is given by the crystal field (Harris, 1995) of the host material (SiC). In 6H-SiC, three different inequivalent lattice sites (two quasi-cubic k_1 and k_2) and one hexagonal (h) exist. The silicon vacancy centre in 4H-SiC has four C dangling bonds to the vacant sites (Hemmingsson et al., 1997). The position of the bonds is localized, while the C atoms relaxes outwards and keeps the C_{3v} symmetry independently of its charge state. The resulting dangling bonds form two a_1 and one e level. The first a_1 state is resonant with the valence band electrons (see Fig. 3.3). The second a_1 level is 0.9 eV above the valence band and the e level is 4.4 meV above the second a_1 level. The negative silicon vacancy centre in 4H-SiC has five electrons. In the negative charge state, two electrons occupy the first a_1 level and one electron on the second a_1 level. The remaining e level is occupied by two electrons. The electron configuration for this charge state is $a^2{}_1 a^1{}_1 e^2$. As long as the lowest a_1 level is filled with two electrons, the only allowed symmetry is $^4A_2$ with spin $S = \frac{3}{2}$. This configuration is also predicted as the ground state of the negatively charged silicon vacancy centre (V_1 and V_2).

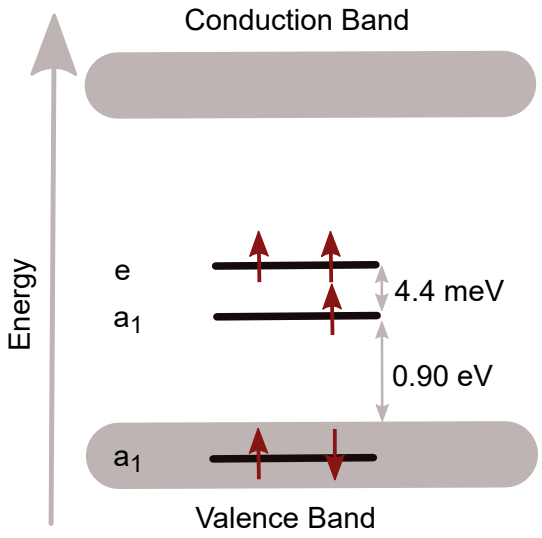

FIGURE 3.3: Band diagram of the silicon vacancy centre within 4H-SiC. The silicon vacancy centre has five electrons. Two electrons on the first a_1 level are resonant with the valence band. One electron is on the second a_1 level 0.90 eV above the valence band. The last two electrons occupy two e levels 4.4 meV above the second a_1 level.

The resulting possible electron multiplets for the silicon vacancy centre can be seen in

Electronic configuration		Possible multiplets
C_{3v}	T_d	
$a_1^2 a_1^2 e^1$		^2E
$a_1^2 a_1^1 e^2$		$^4A_2, {}^2A_2, {}^2E, {}^2A_1$
$a_1^1 a_1^0 e^3$		^2E
	$a_1^2 t_2^3$	$^4A_2, {}^2T_1, {}^2E, {}^2T_2$
$a_1^1 a_1^2 e^2$		$^4A_2, {}^2A_2, {}^2E, {}^2A_1$
$a_1^1 a_1^1 e^3$		$^4E, {}^2E, {}^2E$
$a_1^1 a_1^0 e^4$		$^2A_1$
	$a_1^1 t_2^4$	$^4T_1, {}^2T_1, {}^2E, {}^2T_2, {}^2A_1$
$a_1^0 a_1^2 e^3$		^2E
$a_1^0 a_1^1 e^4$		$^2A_1$
	$a_1^0 t_2^5$	$^2T_2$

FIGURE 3.4: Electron configuration of the silicon vacancy centre with possible electron multiplets. (Janzén et al., 2009)

Fig.. 3.4.

3.1.1 Ground State Spin Hamiltonian of Silicon Vacancy Centre in 4H-SiC

The Hamiltonian of the V_{Si} centre in 4H-SiC ground-state manifold with a static magnetic and driving field can be written as

$$H_{gs} = \underbrace{D_{gs}\hat{S}_z^2}_{ZFS} + \underbrace{\gamma_e \vec{B}\cdot\hat{\vec{S}}}_{ElectronZeeman} + \underbrace{\hat{\vec{S}}\cdot\bar{A}\cdot\hat{\vec{I}}}_{Hyperfine} + \underbrace{\gamma_p \vec{B}\cdot\hat{\vec{I}}}_{NuclearZeeman} + \underbrace{B_1 cos(wt)\hat{S}_x}_{DrivingField}. \tag{3.1}$$

Strain effects are neglected. The first term in Equation 3.1 describes the ZFS. D_{gs} = 4.5 MHz has been inferred experimentally in this thesis. The second term denotes the Zeeman interaction of the electron spin with an external magnetic field, with the gyromagnetic ratio of the silicon vacancy centre $\gamma_e = 28\ MHz/mT$. During this work, the $\vec{B}$ field is considered to be aligned along the c-axis with $\approx \vec{B} = B_z\vec{e}_z$, which simplifies the Zeeman Hamiltonian to $H_{Zeemann} = \gamma_e B_z \hat{S}_z$. The third part of the Hamiltonian describes the hyperfine interaction between the silicon vacancy centre's electron and a nuclear spin. The interaction strength is shown in the hyperfine tensor $\bar{A}$. The silicon vacancy centre can be surrounded either by ^{13}C or ^{29}Si both with a nuclear spin of $I = 1/2$. The fourth part of the spin Hamiltonian describes the nuclear Zeemann interaction. Spin transitions can be described within the ground-state manifold by driving an oscillating magnetic field either in $\vec{e_x}$ or $\vec{e_y}$ direction. The last term in Equation 3.1 describes this interaction. In the rotating frame and by applying rotating wave approximation (Slichter, 1990), the effective magnetic field can be derived from the alternating magnetic field in the form of

$$\vec{B}_{eff} = -\frac{w}{\gamma_e}\vec{e}_z + B_1\vec{e}_x. \tag{3.2}$$

By neglecting the hyperfine interaction and adding the ZFS, the effective magnetic field B_{eff} in z-direction is given by:

$$\vec{B}_{z,eff} = -\frac{1}{\gamma_e}(\underbrace{D \pm \gamma_e B_z - w}_{\Delta_{\pm}^{1,2}}). \tag{3.3}$$

The term w/γ_e is added to the effective magnetic field in z-direction from Equation 3.2. Here the detuning from the Larmor frequency $\Delta_{\pm}^{1,2}$ is introduced. The ground state spin transition $m_s = +1/2 \leftrightarrow +3/2$ corresponds to Δ_+^1 and $m_s = +1/2 \leftrightarrow -1/2$ to Δ_-^1. The third allowed ground state spin transition is $m_s = -1/2 \leftrightarrow -3/2$ is indicated by Δ^2. If the driving MW field fulfills the resonance criteria $w = w_{Larmor}$ the detuning vanishes to $\Delta_{\pm}^{1,2} = 0$ and, as a consequence, also the effective magnetic field. The second term in Equation 3.2 leads to a rotation around the x-axis. The visualization of the rotation can be shown in a Bloch sphere (see Fig. 3.5). Depending on the time duration during which the microwave field is applied along the x-direction, a $\pi/2$, π or $3\pi/2$ pulse is applied to the system. The evolution of all three pulses can be seen in Fig. 3.5 (a-c). The detuning depending on the effective magnetic field along the z-axis can be seen in Fig. 3.5 (d). All measurements on the ground spin states of the silicon vacancy centre in 4H-SiC can be simulated by Equation 3.1. It may be that not all terms of this equation are needed.

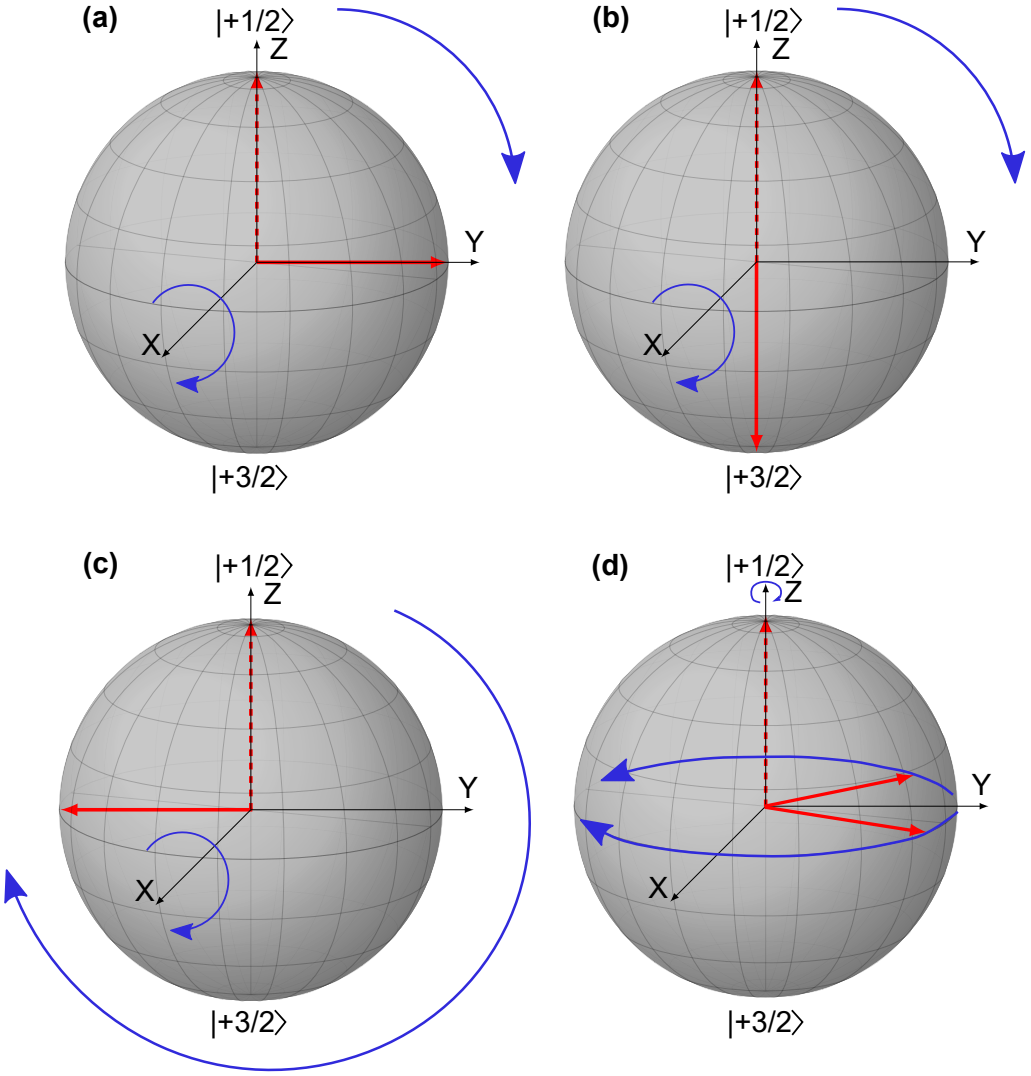

FIGURE 3.5: The Bloch sphere represents the dynamical spin evolution between $m_s = +1/2 \leftrightarrow +3/2$. In (a) is a $\pi/2$ pulse applied. The spin evolves after a $\pi/2$ pulse from the eigenstate $m_s = +1/2$ to a superposition state of $\Phi = \alpha|+1/2\rangle + \beta|+3/2\rangle$. In (b) a π pulse is applied, where after the spin state ends up in $m_s = +3/2$. Also, a $3\pi/2$ pulse is shown in (c). The spin state evolves to $\Phi = \alpha|+1/2\rangle - \beta|+3/2\rangle$. The detuning Δ can be seen in (d) as free evolution around the equator.

3.2 Sample Preparation

All measurements in this chapter were performed on a commercially available high purity 4H-SiC substrate purchased by CREE Inc.. The sample was electron irradiated (2 MeV) with a dose of $5 \cdot 10^{17}$ electrons / cm^2 to create a high density of V_{Si} defect centres. In order to remove contaminations on the surface, acetone in an ultrasonic bath was used. After the acetone treatment, a Piranha solution was used to remove remaining organic contaminations.

3.3 Flourescence Properties

The theoretically calculated energy level scheme proposed by group theoretical analysis is shown in Fig. 3.6 (a) (Soykal, Dev, and Economou, 2016). The ground state of the hexagonal silicon vacancy centre in 4H-SiC called V_1 is a spin quartet of symmetry $^4A_2(a^2{}_1a^1{}_1e^2)$ Fig. 3.4 with a total spin S = 3/2 (Janzén et al., 2009). It was proposed that the ground state $|\pm1/2\rangle$ and $|\pm3/2\rangle$ sublevels of the V_1 centre are split by a zero-fild splitting (ZFS) of 4.5 MHz (Janzén et al., 2009). The two excited states $^4E(a^1{}_1a^1{}_1e^3)$ V_1' and $^4A_2(a^2{}_1a^1{}_1e^2)$ V_1

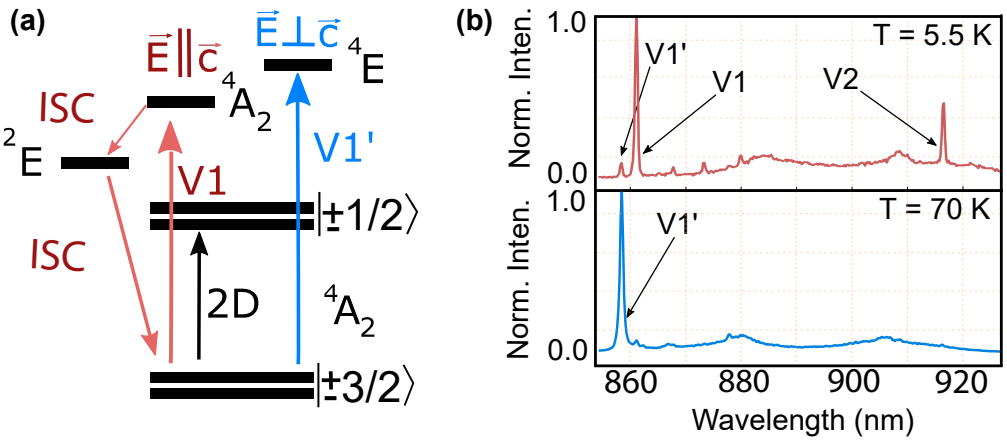

FIGURE 3.6: (a) The energy level scheme of the V_1 centre in 4H-SiC. The V1 optical transition is at 861 nm and V1' at 858 nm. (b) The PL spectrum of a V_{Si} ensemble at 5.5 K and 70 K. Both silicon vacancy types V_1 and V_2 can be seen in the spectrum. The V_1 V_{Si} centre has two excited states one called V1 and the second V1'.

can be selectively excited from the ground state via resonant optical laser excitation. The ZPL energy of the optical transition V_1' and V_1 is 1.445 eV (858 nm) and 1.440 eV (861 nm) (Janzén et al., 2009; Bracher, Zhang, and Hu, 2017). Both optical emission of the V_1 ZPL transition ($^4A_2$ - $^4A_2$) and V_1' emission ($^4A_2$ - V^4E) are observable at a temperature of 5.5 K as shown in Fig. 3.6 (b). The intensity of V_1 and V_1' shows a temperature dependence for which the maximum intensity of V_1 and V_1' is reached at ≈ 4 and 70 K as shown in Fig 3.6 (b). A couple of sharp peaks (ZPL's) can be seen in Fig. 3.6 (b), where the origin is coming from other active defect centres. The peak at 916 nm corresponds to the V_2 silicon vacancy centre at the cubic lattice site (Ivády et al., 2017). The energy difference between the two excited states V_1 and V_1' is roughly 4.4 meV which corresponds to a equivalent thermal energy of 51 K. The temperature effect of enhanced emission of the V_1' optical transition may be related to a phonon-assisted process. The optical lifetime measured with a 805 nm picosecond laser is roughly 5.5 ns as shown in Fig 3.7.

3.3.1 Polarization Properties

The polarization properties of the V_1 silicon vacancy centre are an important parameter to understand the physical nature of the system. The polar plot in Fig. 3.8 (a) shows the integrated intensity of each V_1 and V_1' optical transition inside the ZPL as a function of the

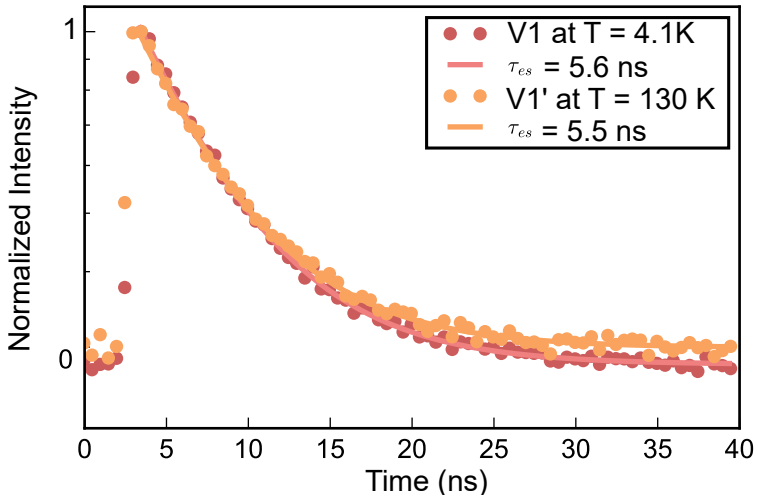

FIGURE 3.7: The excited state lifetime is measured by optically exciting the system with a 805 nm picosecond laser at 4 and 130 K. The dominant optical transition at 4 K is V1 and at 130 K V1'.

half-wave plate angle in emission (see Fig. A.1). The measurement was conducted at T = 5.5 K and with the laser incident angle perpendicular to the c-axis. The emitted photons

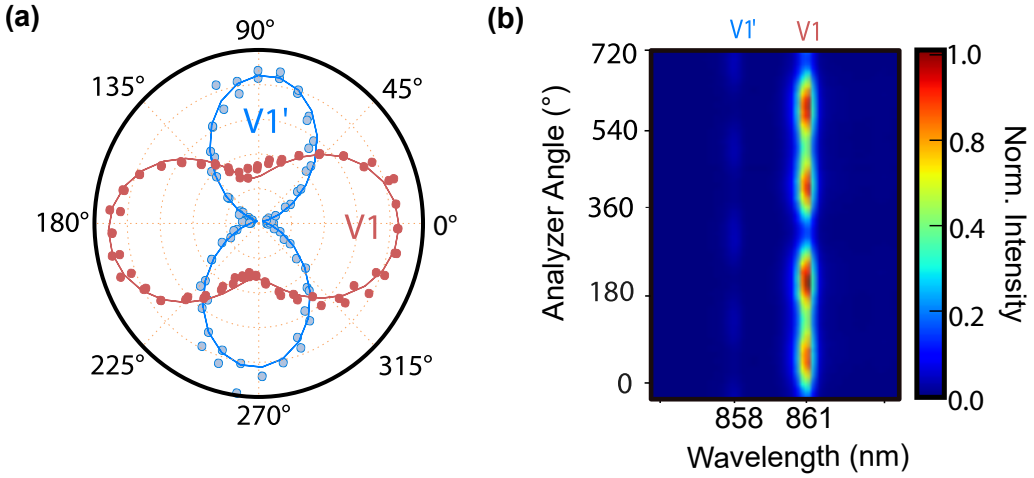

FIGURE 3.8: The optical polarization of the $V_1 / V_1^{'}$ transitions at the sample orientation in which the c-axis is perpendicular to the laser incident direction at 5.5K. (a) The polar plot of the normalized V_1 and $V_1^{'}$ intensities. 0°, equivalently 180°, corresponds to the c-axis orientation. (b) The density plot shows the absolute intensities of the $V_1 / V_1^{'}$ ZPLs.

of V_1 and V_1' inside the ZPL are polarized almost orthogonal to each other. The full optically polarization orientation analysis results are in qualitative agreement with reported optical selection rules based on group theoretical analysis with single group C_{3V}, which represents the symmetry of the silicon vacancy centre in 4H-SiC (Janzén et al., 2009; Wagner et al., 2000). The group theoretical analysis predicts that the electric field component of the emitted photons in the V_1 ZPL is $E \parallel c$, and for the V_1' ZPL $E \perp c$. Fig. 3.8 shows that the emitted photons from V_1' are indeed linearly polarized $E \perp c$. But V_1 is not completely

linear $E \parallel c$ polarized but contains an $E \perp c$ component. This measurement indicates that the current selection rules need revision. Since the negatively charged silicon vacancy V_{Si} contains five electrons which results in an half-integer spin system,the correct symmetry is the double group $\overline{C_{3v}}$ (Soykal, Dev, and Economou, 2016). The prediction of the selection rules for the $\overline{C_{3v}}$ group leads to a better estimate of the relative contribution of the $E \parallel c$ and $E \perp c$ polarization of the emitted photons inside the V_1 and V_1' ZPL. The group theoretical prediction of the polarized photons of V_1 inside the ZPL is a distribution among the two polarizations $E \parallel c : E \perp c$ = 3:1, whereas for V_1' $E \perp c : E \parallel c$ = 11:1. These calculations are in reasonable agreement with the polar plots in Fig. 3.8 (a) and (b) $E \parallel c$ / $E \perp c$ = 1.85±0.06 for V_1 and $E \perp c$ / $E \parallel c$ = 19:3 for V_1.

Group Theoretical Analysis of the Polarization

To gain further details about the polarization of the $\overline{C_{3v}}$ symmetry group, a group theoretical analysis is needed. The individual symmetries of each state belonging to the V_1 ground and first excited states (both labeled as $^4A_2$ in the thesis due to their orbital symmetry) are given as $\{^1E_{3/2}, ^2E_{3/2}, ^+E_{1/2}, ^-E_{1/2}\}$ in the

$$\{|3/2\rangle + i|-3/2\rangle, |3/2\rangle - i|-1/2\rangle, |1/2\rangle, |-1/2\rangle\} \tag{3.4}$$

zero field spin basis. Similarly, the symmetries of each state belonging to the second excited state (labeled as ^{4}E) are given as

$$\{E^+_{1/2}, E^-_{1/2}, {}^1E_{3/2} + {}^2E_{3/2}, {}^1E_{3/2} - {}^2E_{3/2}, E^+_{1/2}, E^-_{1/2}, E^+_{1/2}, E^-_{1/2}\} \tag{3.5}$$

in the $\{|3/2\rangle, |-3/2\rangle, |-1/2\rangle, |1/2\rangle, |-3/2\rangle, |3/2\rangle\}$ spin basis. Note that the previously predicted small spin mixing between some of the ^1E states (due to higher order spin-spin interactions) (Yang et al., 2016) are omitted here. The optical selection rules between these

C_{3v}	$E_{1/2}$	$^1E_{3/2}$	$^2E_{3/2}$
$E_{1/2}$	A_1, E	E	E
$^1E_{3/2}$	E	-	A_1
$^2E_{3/2}$	E	A_1	-

FIGURE 3.9: Optical selection rules of $\overline{C_{3v}}$ symmetry.

various symmetries are given in Fig. 3.9 in terms of the vector components $\{(\hat{x}, \hat{y}); \hat{z}\} \in \{E; A_1\}$ of the electric field within the $\overline{C_{3v}}$ double group. The $\hat{z}$ axis is parallel to the defects c-axis. Therefore, by considering all four possible transitions after the spin selection

rules are applied, I find that the V_1 transition has a mixed polarization of $E \parallel c : E \perp c =$ 3:1 involving the electric field components parallel and orthogonal to the c-axis. For the more complicated V_1 transition consisting of 12 possible transitions, I found the polarization ratio to be roughly (1:11). Thus, the V_1 ($^4A_2$ to $^4A_2$) transition contains polarizations both parallel and orthogonal to the c-axis whereas the V_1 ($^4A_2$ to ^4E) is mostly polarized along the basal plane of the defect. These expectations are in very good agreement with

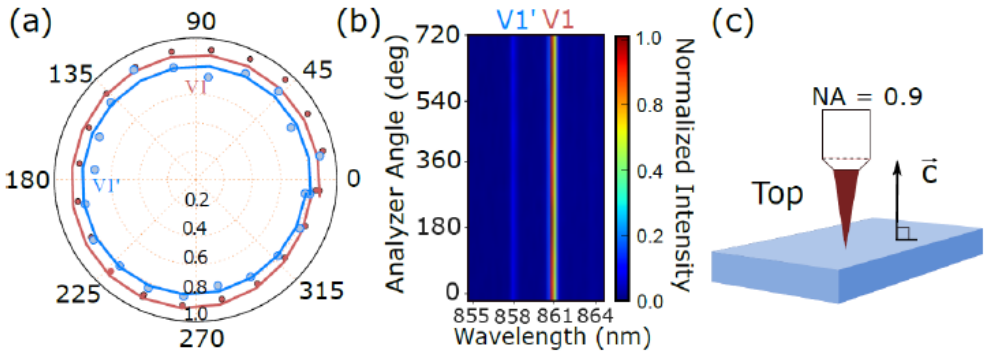

FIGURE 3.10: The polarization of the $V_1/V_1^{'}$ ZPLs analyzed with an HWP and PBS at the sample orientation in which the laser incident orientation coincide with the c-axis. (a) The polar plot of the normalized V_1 and $V_1^{'}$ intensities. (b) The density plots showing the absolute intensities of the $V_1/V_1^{'}$ ZPLs. (c) The schematic diagrams depicting the sample orientation with respect to the laser incident orientation.

our experimental results shown in Fig. 3.8. Fig. 3.10 and 3.11 show that, as expected, only photons with $E \perp c$ polarization are registered in this geometry, and all directions in the plane perpendicular to the c-axis are equivalent. The orbital and spin properties of this

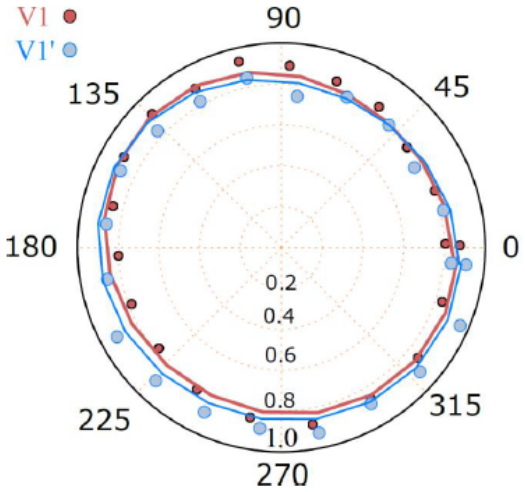

FIGURE 3.11: V_1 and $V_1^{'}$ ZPL polarization analyzed by a QWP and a PBS. The laser incidence orientation is parallel to the c-axis.

defect are different from the well-studied NV centre in diamond and the DiVacancy in SiC.

While both ground states of V_{Si} and NV centres feature A_2 orbital symmetry, V_{Si} has entirely different electron and spin configuration (quartet versus triplet) with distinct optical selection rules dictated by the $\overline{C_{3v}}$ double group representations. The V_1 transition with $E \perp c$ polarization is reminiscent of the NV centre $E_{\pm} \rightarrow A_{1,2}$ transitions (Yang et al., 2016), which are circularly polarized and have been used for spin-photon entanglement (Rao, 2015).

3.3.2 Temperature Dependency Model

At a temperature of 5.5 K, the emission of the V_1 ZPL transition ($^4A_2\,|es\rangle$ to $^4A_2\,|gs\rangle$) dominates. With increasing temperature, the intensity of the V_1 ZPL decreases, whereas the V_1 ZPL emission ($^4E\,|es\rangle$ to $^4A_2\,|gs\rangle$) becomes more prominent and peaks at around 70 K, as shown in Fig. 3.12. The energy difference between the ZPLs of V_1 and V_1 is about 4.4 meV which corresponds to a thermodynamic equivalent temperature of 51 K. The enhanced emission from the V_1 transition at elevated temperatures may be understood as a phonon-assisted process, where the temperature-induced dephasing of the orbital excited states leads to thermally-induced excitation transfer among the excited states between V_1 and V_1 excited states. The transfer reaches a maximum when temperature-induced mixing (dephasing) becomes comparable to the splitting between the energy levels. The experimental observation, however, cannot be explained by a simple thermally induced excita-

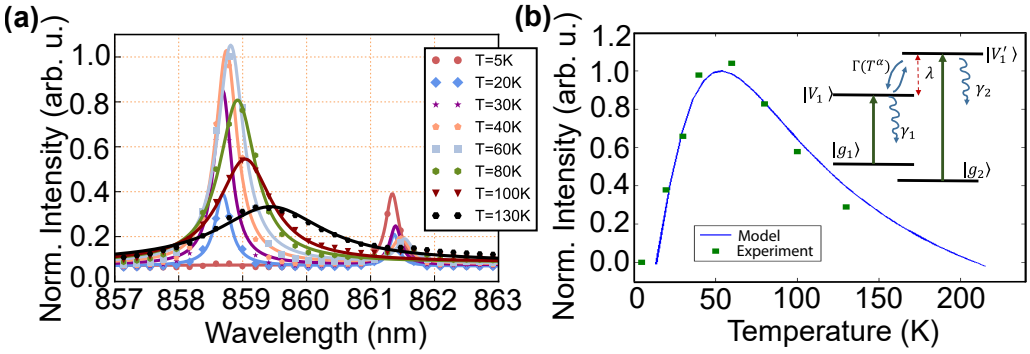

FIGURE 3.12: Temperature dependence of silicon vacancy centre ZPL emission. (a) The temperature dependence of both V_1 and $V_1^{'}$ ZPLs from 5 K to 130 K. (b) A model to describe the temperature dependence.

tion transfer but rather requires a more complex mixing of excited states. We performed numerical simulations of the Lindblad master equation for a four-level system with two ground and two excited states as shown in Fig. 3.12 (b) using the experimental decay rates of the V1 and V1 excited states (to be discussed later). In this model, as discussed below, we introduced, in addition to the normal decay channels from the excited states as shown above, a temperature-dependent mixing of the excited states at a rate $\Gamma(T^{\alpha})$ with a power-law dependence on temperature. We find that the best fit to our data occurs for $\alpha \approx 1.57$. This is consistent with the inter-level phonon coupling (pseudo Jahn-Teller effect) between the V1 and V1' states mediated by the E-symmetry vibrational normal modes of the lattice (Perlin and Wagner, 1984). Starting from the molecular orbits of the defect cen-

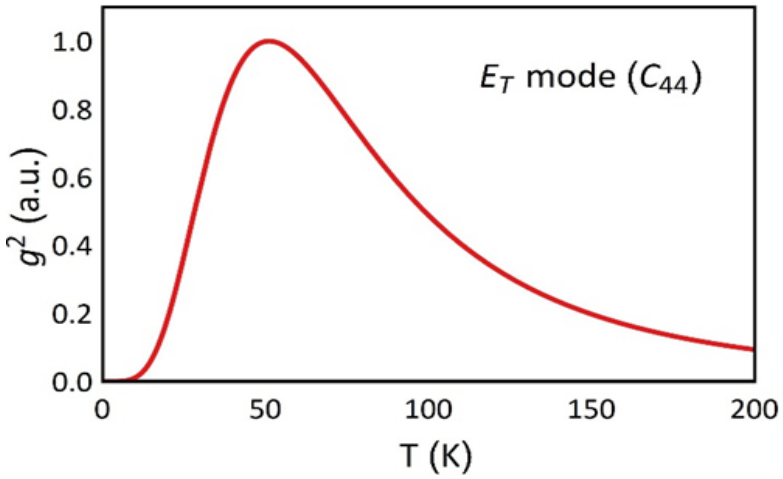

FIGURE 3.13: Coupling strength of the E symmetry. Normalized electron-phonon coupling square g^2 between the E symmetry transverse vibrational mode (propagating along [001]) and V_{Si} defect in 4H-SiC as a function of temperature.

tre, one can form an irreducible representation for the symmetry operator of the defect in which the ground and excited states are constructed. By incorporating the spin-orbit and spin-spin interactions, one can find the splitting among various states resulting in the formation of energy subspaces $^4A_2$ ground and excited states separated by 1.44 eV, and the 4E excited state split from the $^4A_2$ excited state by 4.4 meV. At finite temperature T, these energy states are broadened; thermal energy acts as a dephasing operation that introduces incoherent mixing among the energy states. As the $^4A_2$ ground and excited states are split by 1.44 eV, the energy gap exceeds way above the thermal broadening for the working temperatures and is not relevant to the present discussion. On the other hand, the excited states $^4A_2$ and ^4E which are split by only 4.4 meV corresponding to 51 K should mix in a fashion that changes the optical emission properties. We see similar effects in the experiment as shown in Fig. 3.12 and below we give a simple quantum mechanical model that explains this temperature behavior. Instead of considering all the 32 states of the excited subspace and ground state subspace, we consider a simpler case of a four-level system that explains the observed temperature behavior of the V1 excitation. The four-level system is formed by two excited states and two ground states. The Hamiltonian governing the dynamics in the dressed basis given by

$$H = E_+ |g_1\rangle \langle e_+| + E_- |g_2\rangle \langle e_-| + \lambda(|e_+\rangle \langle e_+| - |e_-\rangle \langle e_-|) + h.c., \tag{3.6}$$

where the optical fields with an intensity E_+, couple the ground and excited states and λ , is the spinorbit splitting of the excited states. The dressed excited states are given by

$$|e_\pm\rangle = \frac{1}{\sqrt{2}}[|e_1\rangle \pm |e_2\rangle]. \tag{3.7}$$

Additionally, the excited states decay to the respective ground states and also suffer from a temperature dependent dephasing that causes incoherent mixing within the dressed basis. Including these non-unitary terms, the total dynamics is then described by a master equation

$$\dot{\rho}(t) = -i[H,\rho(t)] + \sum_k \gamma_k [\mathscr{L}_k \rho \mathscr{L}_k^\dagger - \frac{1}{2}(\rho \mathscr{L}_k \mathscr{L}_k + \mathscr{L}_k^\dagger \mathscr{L}_k \rho)] \tag{3.8}$$

where the Lindblad operators are $\mathscr{L}_1 = |g_1\rangle\langle e_+|$, $\mathscr{L}_2 = |g_2\rangle\langle e_-|$, $\mathscr{L}_3 = |e_1\rangle\langle e_1| - |e_2\rangle\langle e_2|$, with respective decay rates $\gamma_1, \gamma_2, \gamma_d$. While the optical decay is described by the operators $\mathscr{L}_1$ and $\mathscr{L}_2$, the dephasing is described by $\mathscr{L}_3$. We assume a power-law temperature dependence for the dephasing rate, i.e. $\gamma_d(T^a)$. By taking γ_2, γ_1 and solving the master equation, we find the temperature dependence of the relative intensity of the two emission lines by evaluating the steady state populations in the ground states that are initially equally populated. At very high temperatures, i.e., $\lambda \ll \gamma_d$, the dressed basis is completely dephased resulting in no population exchange among the two excited states. Similarly, in the other extreme limit $\gamma_d \ll \lambda$, there is no population exchange between $|e_+\rangle$ and $|e_-\rangle$ states as the detuning is much larger than the thermal dephasing. Only in the intermediate regime, there is population exchange between $|e_+\rangle$, allowing for maximal population transfer to $|g_2\rangle$, i.e., enhanced emission in the second decay channel, V_1'. Moreover, the physical origin of the mixing between the $^4A_2$ and ^4E states in our model can be determined by examining the molecular vibrations of the Si monovacancy centre. These Raman and infrared active vibrational normal modes in the vicinity of the defect belong to the $2a_1 + 2e$ irreducible representations of the C_{3v} symmetry group. Therefore, the first (V1) and second (V1') excited states with $^4A_2$ and ^4E symmetry, respectively, are only allowed to couple each other by the E symmetry vibrational normal modes. Such inter-level coupling between nearly degenerate electronic states that are linear in lattice displacements is also known as the pseudo-Jahn-Teller (PJT) effect. Using an electron-lattice coupling Hamiltonian of

$$H_{e-p} = G\begin{bmatrix} 0 & \theta & -\eta \\ \theta & 0 & 0 \\ -\eta & 0 & 0 \end{bmatrix} + \frac{\Delta}{3}\begin{bmatrix} -2 & 0 & 0 \\ 0 & 1 & 0 \\ 0 & 0 & 1 \end{bmatrix} + \frac{1}{2}K(\theta^2+\eta^2) \tag{3.9}$$

given in the electronic basis states $|A\rangle; |E_x\rangle, |A_y\rangle$ of $^4A_2$ and ^4E states, we obtain a minimum Jahn-Teller energy configuration of

$$E_\pi = -\frac{\Delta}{6} - \epsilon_0 - (\frac{\Delta}{4\epsilon_0})^2 \tag{3.10}$$

at normal mode displacement $Q = \sqrt{\theta^2+\eta^2} = [Q_0^2 - (\frac{\Delta}{2G})^2]^{1/2}$. The terms $\epsilon_0 = \frac{G^2}{2K}$ and $Q_0 = \frac{G}{K}$ correspond to the PJT energy and normal mode nuclear displacement, respectively, when the energy splitting between the excited states is zero ($\Delta = 0$). They are given in terms of the electron-phonon coupling G and lattice K force constants. From $Q > 0$, the condition for the PJT instability to occurreduces to the well-known order-of-magnitude rule $|\frac{\Delta}{4\epsilon_0}| < 1$ (Stoneham, 2001). It is important to note that due to the small energy splitting

(4.4 meV) between the excited states of this defect, this condition is satisfied and the wave function at A_2 excited state minimum becomes a linear combination of the electronic A_2 and E symmetry states. To illustrate the temperature dependence of this PJT mixing, we define the coupling strength of the E symmetry normal mode vibrations to the defect as $g(w) = \rho_D(w) f(q(w)) \xi(w)$ in terms Debye density of states $\rho_D = \frac{3w^2}{2v_n^3\pi^2}$ and phonon coupling coefficient $\xi(w) = (\frac{\hbar w_n}{2Mv_n^2})^{1/2}$ for the n^{th} mode with velocity v_n. This leads to a $T^{\frac{3}{2}(w^{\frac{3}{2}})}$ temperature dependence consistent with our findings above. The defect wave functions extended over many lattice sites are reflected in a cut-off function $f(q) = (1 + \frac{r_B^2 q^2}{4})^{-2}$ using an effective mass approximation within an effective Bohr radius of r_B. We now have a quick look at one of the E symmetry transverse phonon modes around the defect propagating along [100] and polarized along [001] with sound velocity of $v = 7.1{\cdot}10^3 \frac{m}{s}$ in 4H-SiC. We use an effective Bohr radius of 2.7 nm (Beke et al., 2015) to include most of the charge density around the V_1 defect, comparable to some deep centre acceptor states and 3C-SiC. Resulting electron-phonon coupling strength square with respect to temperature is shown in Fig. 3.13 and it is closely related to what is observed in the experiment (Fig. 3.12) since the contrast between V_1 and V_1' states is proportional to g^2. Although more sophisticated cut-off functions can be used for this deep centre, they are beyond the scope of the current work.

3.4 Optical Spin State Detection of Silicon Vacancy Centre in Ensembles

In this section I will demonstrate Optical Dectected Magnetic Resonance (ODMR) measurements on ensembles to characterize and detect the spin states of V_{Si} centre in 4H-SiC. At any constant finite magnetic fields (B_0), the spin energy levels are determined by the Hamiltonian,

$$H = g\mu_g \mathbf{BS} + D[S_z^2 - \frac{S(S+1)}{3}] \tag{3.11}$$

where g is the Landé g-factor, μ_g is the Bohr magneton, D is the ZFS (2 D = 4.5 MHz), and S_z is the projection of the total spin onto the quantization axis, the c-axis in 4H-SiC. By applying resonant radio-frequency (RF) fields one can induce transitions between spin sublevels (Fig. 3.6 (a)), resulting in a change in ODMR as shown in Fig. 3.14. The relative change in ODMR signal is calculated as

$$C = \frac{I(f) - I_{\text{off}}}{I_{\text{off}}} \tag{3.12}$$

$I(f)$ is the PL intensity at the RF frequency f , and I_{off} is the PL intensity at the offresonant RF frequency. The spin-sublevels are energetically split by B_0 = 60 G aligned along the c-axis. The relative ODMR signal as a function of the driving RF frequency shows a negative signal at 170 MHz, with the relative intensity 0.05 % as shown in the upper panel of Fig. 3.15 (a). It is attributed to the V_1 silicon vacancy ground state spin. A similar signal was also reported for V_1 and V_3 centres in 6H-SiC (Baranov et al., 2011). The two outer spin

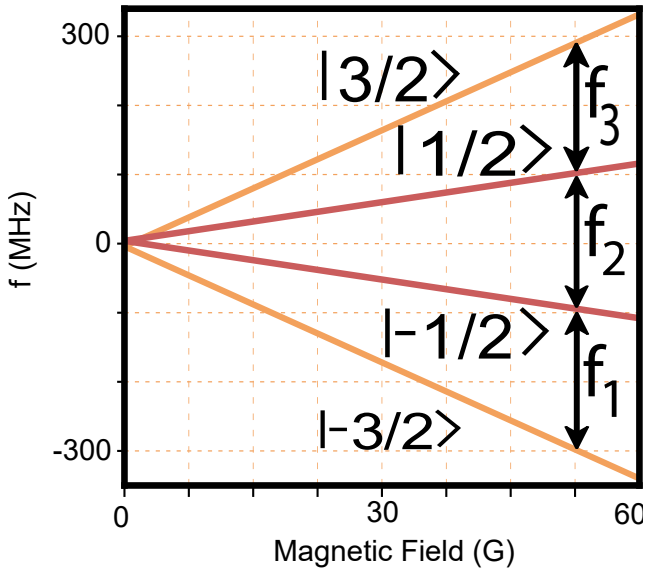

FIGURE 3.14: Zeeman effect of the spin $\frac{3}{2}$ ground state of the V_1 centre for $B||c$. f_1, f_2, and f_3 represent possible resonant spin transitions.

transitions in Fig. 3.15 (a) are a signature of the silicon vacancy V_2 defect (Widmann and Lee, 2015) in 4H-SiC. By exciting the optical transition V_1 resonantly, a positive relative ODMR signal with $100\% \pm 0.6$ is achieved (lower panel in Fig. 3.15 (a)). In contrast, excitation of the V_1 optical transition in Fig. 3.6 (a), reveals a negative signal with a minimal change in the relative signal intensity Fig. 3.15 (b). A similar substantial enhancement of the ODMR signal was reported for the V_2 centre ensemble in 6H-SiC (Baranov et al., 2011). Although at this time the underlying mechanism is not yet completely understood,

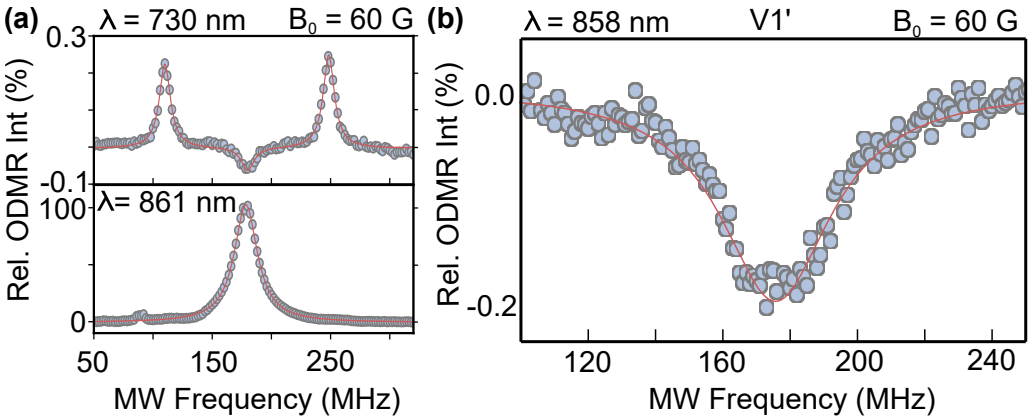

FIGURE 3.15: Optically Detected Magnetic Resonance: (a) Upper panel: an ensemble ODMR spectrum with a 730 nm laser at 60 G. Lower panel: the ODMR with a laser resonant to V_1, 861 nm. (b) ODMR with a resonant laser at $V_1^{'}$ ($\lambda = 858$ nm).

we attribute it to the enhanced spin polarization in the ground state resulting from resonant optical excitation. Resonant excitation of V_1 ZPL results in the excitation into the lowest vibrational level of the V_1 excited state vibrational levels. This observation may also

indicate that optical polarization is mainly established by the intersystem-crossing (ISC) between the $^4A_2$ excited states and the ^2E metastable state while the ^4E excited states have a less efficient ISC (Soykal, Dev, and Economou, 2016). I expect further enhancement of the ODMR signal when a single V_1 centre is isolated owing to the suppressed inhomogeneous broadening. I note that if an identical ODMR contrast, namely C, and an identical photoluminescence (PL) intensity without spin resonance are assumed, a positive signal leads to a signal-to-noise ratio larger than the negative signal, as of the NV centre in diamond (Balasubramanian, 2009) and DiVacancies in 4H- and 6H-SiC (Falk, 2013), by a factor of $(1-C)^{-0.5}$.

3.4.1 Signal-to-Noise Ratio of Enhancement and Quenching ODMR Signal

The contrast of ODMR signals is defined by $C \equiv \frac{I_{\max}-I_{\min}}{I_{\max}}$: $C_p = \frac{I_p-I_0}{I_p}$ and $C_m = \frac{I_0-I_m}{I_0}$ for the signal which is enhanced and quenched by spin resonance, respectively. Here I_0, I_p , and I_m are the PL intensity without applying magnetic resonance, the total PL intensity which is enhanced and quenched by magnetic resonance, respectively. Note that $0 \le C \le 1$, and C is different from the relative ODMR intensity used in Fig. 3.15. If we assume identical contrast ($C_p = C_m = C$), and shot-noise limit, the relative ratio of the signal-to-noise ratio (SNR) of the enhancement signal with respect to that of the quenching signal is, by using uncertainty propagation,

$$\frac{\frac{C_p}{\partial C_p}}{\frac{C_m}{\partial C_m}} = \frac{\partial C_p}{\partial C_m} = \frac{\sqrt{\frac{I_m I_0 + {I_m}^2}{{I_0}^3}}}{\sqrt{\frac{I_0 I_p + {I_0}^2}{{p}^3}}} = \frac{1}{\sqrt{1-C}} \ge 1 \tag{3.13}$$

Thus, the enhancement signal for a positive ODMR signal has a better SNR ratio in comparison to a negative ODMR signal by a factor of $(1-C)^{-0.5}$.

3.5 Rabi Oscillations in Silicon Vacancy Ensembles

In order to demonstrate coherent control of the electronic spins, we investigated spin dynamics of V_1 centre ensembles with a driving RF field. The resulting distribution of the Rabi oscillations in the range of f = 160-190 MHz at B_0 = 60 G, is shown in Fig. 3.16. The dynamics is strikingly different from the single frequency Rabi oscillations typical of a two-level system. Further understanding can be obtained by plotting the Fast-Fourier transform of the Rabi oscillations, for different values of the driving power. For two-level transitions one expects parabolic profiles, corresponding to a Rabi frequency Ω increasing with the detuning $\Delta\Omega$ as $\Omega^2 = {\Omega_0}^2 + \Delta\Omega^2$ where Ω_0 is the driving frequency determined by the applied B_1 field strength ($\Omega_0 \sim B_1$). The experimental data reveal richer and more complex dynamics. We explain our observations with the presence of three closely-spaced transitions, corresponding to f_1 , f_2 , and f_3 in Fig. 3.16 (a). While resonantly driving one transition, due to the small ZFS, off-resonant excitation of the other two transitions is not negligible. To support this explanation, we developed a theoretical model based on four

levels of $S = \frac{3}{2}$ driven by a single monochromatic radio-frequency field. The system dynamics is investigated assuming initial polarization into an incoherent mixture of $|S_z \pm \frac{3}{2}\rangle$. Further details on the simulation can be found in Section 3.5.1. The simulations match

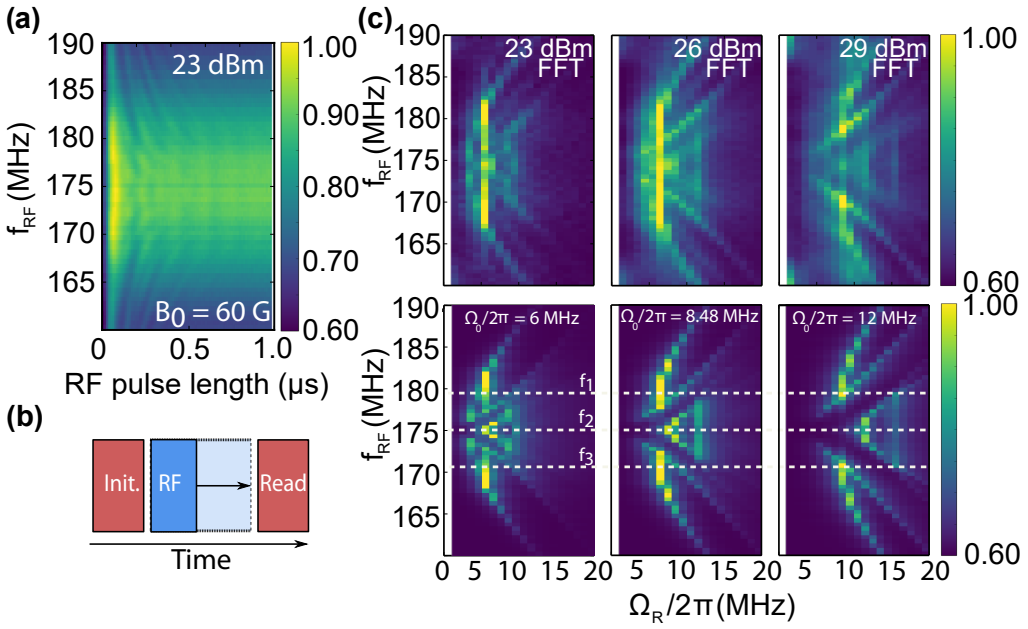

FIGURE 3.16: (a) Rabi measurement with detuned RF driving frequencies. (b) Pulse scheme for a Rabi measurement. The first laser pulse (Init.) polarizes the spin state. The RF pulse manipulates the spin state followed by the last laser pulse (Read) for the spin state readout. (c) Fast Fourier transformed Rabi oscillations at different RF powers. (d) Simulated Rabi oscillations. The dotted lines indicate three resonant RF frequencies, as shown in Fig. 3.14 (a). The strong zero frequency intensities in both (c) and (d) are removed for better distinguishability of the Rabi frequencies.

quite closely the complex structure of the experimental data (see Fig. 3.16 (c, d)). When f is lower than f_1 $|-\frac{3}{2}\rangle \leftrightarrow |-\frac{1}{2}\rangle$, the transition f_1 is mainly excited, leading to a parabolic profile. However, off-resonant excitation of the transition f_2, coupling $|-\frac{1}{2}\rangle$ to $|+\frac{1}{2}\rangle$, results in a second weaker Fourier component in the Rabi spectrum with larger Rabi frequency. With increasing RF power (B_1 field strength), simulated by increasing the driving frequency proportional to the increase of the experimentally used B_1 field strength, this component becomes stronger. When $f = f_2$, one simultaneously drives off-resonantly the transitions f_1 and f_3, resulting in a larger Rabi frequency. This is evident in the plots corresponding to the largest RF power, where the parabolic profile centered around f_2 shows a much larger Rabi frequency than the profiles related to f_1 and f_3. Note that the experimental data can only be explained by assuming the excitation of the $|-\frac{1}{2}\rangle \leftrightarrow |+\frac{1}{2}\rangle$ transition, which was not reported. Additionally, the assumption for initial polarization into $\pm\frac{1}{2}$, which is the case for the V_2 centre, does not reproduce the observed signal. Note that we report for the first time the experimental evidence for S=$\frac{3}{2}$ of the ground state of the V_1 in 4H-SiC. The small ZFS poses challenges for high-fidelity coherent spin control, which need to be addressed for the V_1 centre to be a serious contender for quantum technology. There are

several possibilities to explore: use of (i) optimal quantum control sequences, (ii) adiabatic passage techniques that restrict the dynamics only to a two level subspace (e.g. $|+\frac{3}{2}\rangle$ and $|-\frac{1}{2}\rangle$), with no leakage to other states of the Hilbert space (Oreg, Hioe, and Eberly, 1984), (iii) pulses designed to avoid a transition by building holes in their frequency spectrum to avoid leakage (Neill, 2016), (iv) superadiabatic (shortcuts to adiabaticity) control (Berry, 2009), which was recently demonstrated for NV centres in diamond (Zhou et al., 2017). Alternatively, the V_1 in 6H-SiC is known to exhibit a larger ZFS (Sörman et al., 2000; Janzén et al., 2009), which would relax this problem.

3.5.1 Numerical Model of Silicon Vacancy Rabi Oscillations in Ensembles

In this section I will discuss a theoretical model for the observed distribution of the Rabi oscillations as in Fig. 3.16. We consider a spin S = $\frac{3}{2}$ system, driven by a radio-frequency field with amplitude Ω and frequency ω under a static magnetic field B. The system dynamics is investigated assuming initial polarization into an incoherent mixture of $S_z = |\pm\frac{1}{2}\rangle$. The system Hamiltonian is $H = H_0 + \Omega[cos(wt)\hat{S}_x + sin(wt)\hat{S}_y]$, where H_0 is the diagonal Hamiltonian with energy levels $\varepsilon_{\pm\frac{3}{2}} = \pm\frac{3}{2}\gamma B$ and $\varepsilon_{\pm\frac{1}{2}} = (D \pm \gamma B)$, γ is the gyromagnetic ratio (γ = 28 MHz/mT) and D the zero-field splitting (2D = 4.5 MHz for the V_1 centre). We set ourselves in a frame rotating at angular velocity w around the z-axis:

$$U = e^{-iwt\hat{S}_z}\begin{bmatrix} e^{3iwt/2} & 0 & 0 & 0 \\ 0 & e^{iwt/2} & 0 & 0 \\ 0 & 0 & e^{-iwt/2} & 0 \\ 0 & 0 & 0 & e^{-3iwt/2} \end{bmatrix} \tag{3.14}$$

The Hamiltonian in this rotating frame can be calculated as $H_{\text{rot}} = U^\dagger H U - i\dot{U}U^\dagger$. Neglecting fast components at $2w$ (rotating-wave approximation), we get:

$$H_{rot} = \begin{bmatrix} \epsilon_{-\frac{3}{2}} + (\frac{3}{2})w & (\frac{\sqrt{3}}{4})\Omega & 0 & 0 \\ (\frac{\sqrt{3}}{4})\Omega^* & \epsilon_{-\frac{1}{2}} + (\frac{1}{2})w & \frac{\Omega}{2} & 0 \\ 0 & \frac{\Omega^*}{2} & \epsilon_{+\frac{1}{2}} - (\frac{1}{2})w & (\frac{\sqrt{3}}{4})w \\ 0 & 0 & (\frac{\sqrt{3}}{4})w & \epsilon_{+\frac{3}{4}} - (\frac{3}{2})w \end{bmatrix} \tag{3.15}$$

Let $|u_i\rangle$ be the eigenvectors of H_0 , i.e. the eigenvectors corresponding to $S_z = -\frac{3}{2}, -\frac{1}{2}, +\frac{1}{2}, +\frac{3}{2}$. The time-independent Schrödinger equation for $H|v_i\rangle = a_i|v_i\rangle$. Let V the matrix of the eigenvectors of: $|v_i\rangle = \sum_k V_{ik}|u_k\rangle$. Let us assume that the initial state is one of the eigenvectors of H_0: $|\Psi_0\rangle = |u_k\rangle$, which can be expressed as a linear combination of eigenvectors of H as $|u_k\rangle = \sum_l V^{-1}{}_{kl}|v_l\rangle$. The temporal evolution is described by Schrödinger equation as:

$$|\Psi(t)\rangle = e^{-iHt/\hbar}|\Phi_0\rangle = \sum_l e^{-ia_l t/\hbar}|v_l\rangle = \sum_{l,m} e^{-ia_l t/\hbar} V^{-1}_{kl} V_{lm}|u_m\rangle\,. \tag{3.16}$$

After a time t, the probability associated with the state $|u_m\rangle$ is:

$$\rho_{mk}(t) = |\sum_{l,m} e^{-ia_l t/\hbar} V^{-1}_{kl} V_{lm}|^2. \tag{3.17}$$

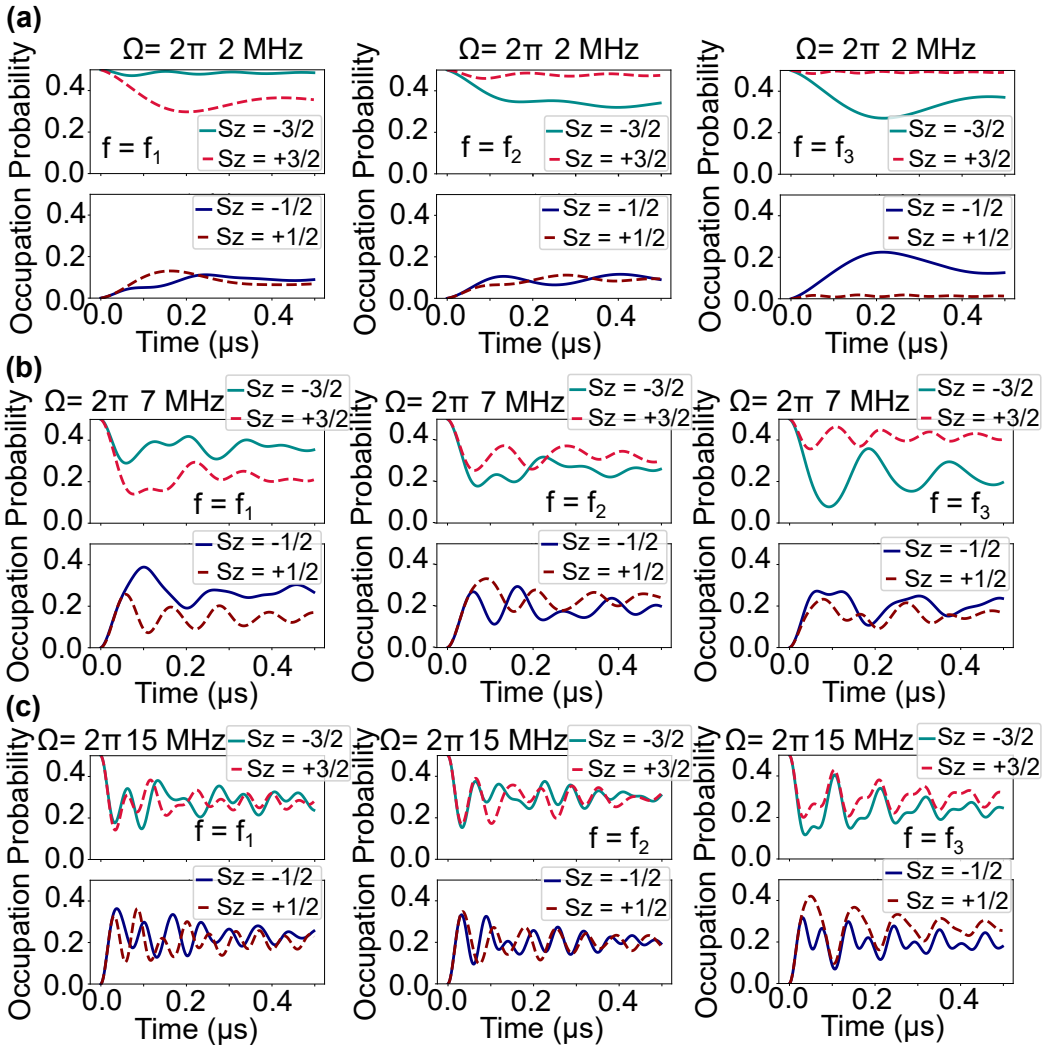

FIGURE 3.17: Rabi model. Spin level populations as a function of time under radiofrequency driving at frequency f and amplitude Ω.

Assuming that each spin level is associated with a photoluminescence intensity I_m, the total photo-luminescence $I_k(t)$, assuming initialization into $|\Psi_0\rangle = |u_k\rangle$, evolves as:

$$I_k(t) = \sum_k I_m \rho_{mk}(t). \tag{3.18}$$

For the silicon vacancy, optical excitation results in a identical polarization of S_z = - 3/2 and S_z = +3/2. This case would require the solution of the Liouville equation for the density matrix. Here, we take a more empirical approach, considering the incoherent superposition of pure states, each evolving according to Schrödinger equation, as discussed above. Assuming that the probability of initial spin polarization into the eigenstate $|u_k\rangle$ is described by P_k, the temporal evolution of photoluminescence intensity is calculated as:

$$I(t) = \sum_{m,k} I_m P_k |\sum_{l,m} e^{-i a_l t/\hbar} V_{kl}^{-1} V_{lm}|^2 \tag{3.19}$$

I investigate the electron spin dynamics assuming perfect initial polarization in an incoherent mixture of S_z = -3/2 and S_z = +3/2, corresponding to $P_{+\frac{3}{2}} = P_{-\frac{3}{2}} = 0.5$, $P_{+\frac{1}{2}} = P_{-\frac{1}{2}} = 0$. Results are shown in Fig. 3.17, for three different values of Ω ($\Omega/2\pi$ = 2 MHz, 7 MHz, and 15 MHz). In each case, we plot the dynamics for a driving frequency corresponding to each of the three transitions: f = f_1($|-\frac{3}{2}\rangle \leftrightarrow |-\frac{1}{2}\rangle$), f = f_2 ($|-\frac{1}{2}\rangle \leftrightarrow |+\frac{1}{2}\rangle$), f = f_3($|+\frac{1}{2}\rangle \leftrightarrow |+\frac{1}{2}\rangle$). We include decoherence in the results by an exponential decay with time constant T_2^* = 200 ns. The simulation results, presented in Fig. 3.16 (c) (lower graph), show good agreement with the experimental data. Simulation accuracy could be further improved by including inhomogeneous broadening and finite bandwidth of the applied RF field. Numerical simulations were also performed solving the Liouville-von Neumann equation for the density matrix: no significant difference was observed with respect to the simplified model illustrated above.

3.5.2 Rabi Oscillations at High Magnetic Field

The Rabi measurements were done at B_0 = 60 and 1000 G. The data which was collected at B_0 = 60 G is shown in Fig. 3.18. The magnetic field was applied at B_0 = 60 G with a large cylindrical permanent magnet (30 mm diameter and 50 mm thick) from outside the cryostat chamber, and the magnetic field was aligned to the c-axis. For B_0 = 1000 G a small samarium cobalt magnet (1 mm thick and 10 mm diameter) was placed beneath our 4H-SiC sample. The measured Rabi oscillations in the time domain and their FFT can be seen in Fig. 3.18. I observed seriously broadened Rabi frequency distributions near-independent on the detuning of the RF field frequency over the tested RF frequency range. I attribute this broadening to the serious inhomogeneous broadening originating from the small magnet placed right below the sample. Note that similar broadening can happen in the disordered spin distribution in a homogeneous magnetic field (Michel et al., 2009; Lee et al., 2010). The large magnet used for 60 G experiment may not produce such serious inhomogeneity since it was placed outside the chamber (17 cm away from the sample) thus the magnetic field gradient inside the focal volume is likely to be insignificant.

3.6 Coherent Spin Control of Silicon Vacancy Ensembles

I studied spin coherence at T = 5.5 K with B_0 = 60 G and 1000 G by Ramsey, Hahn-echo, and XY-8 dynamical decoupling pulse sequences by optical excitation resonant with the V_1 ZPL (861 nm). I observed an evolution of the coherent superposition with the electron spin dephasing time of T_2^* = 1.3 ± 0.3 μs at B_0 = 1000 G aligned parallel to the c - axis by a Ramsey experiment as shown in Fig. 3.19. To suppress the inhomogeneous broadening in an ensemble and decouple the spin ensembles from low-frequency spin noise from such as paramagnetic impurities and a nuclear spin bath composed of ^{29}Si and ^{13}C (Yang et al., 2014), we applied a Hahn-Echo sequence. Identical laser pulses of 2 μs length were applied before and after the MW pulse sequences for the optical spin polarization and projective spin state readout, respectively, and also to avoid dephasing due

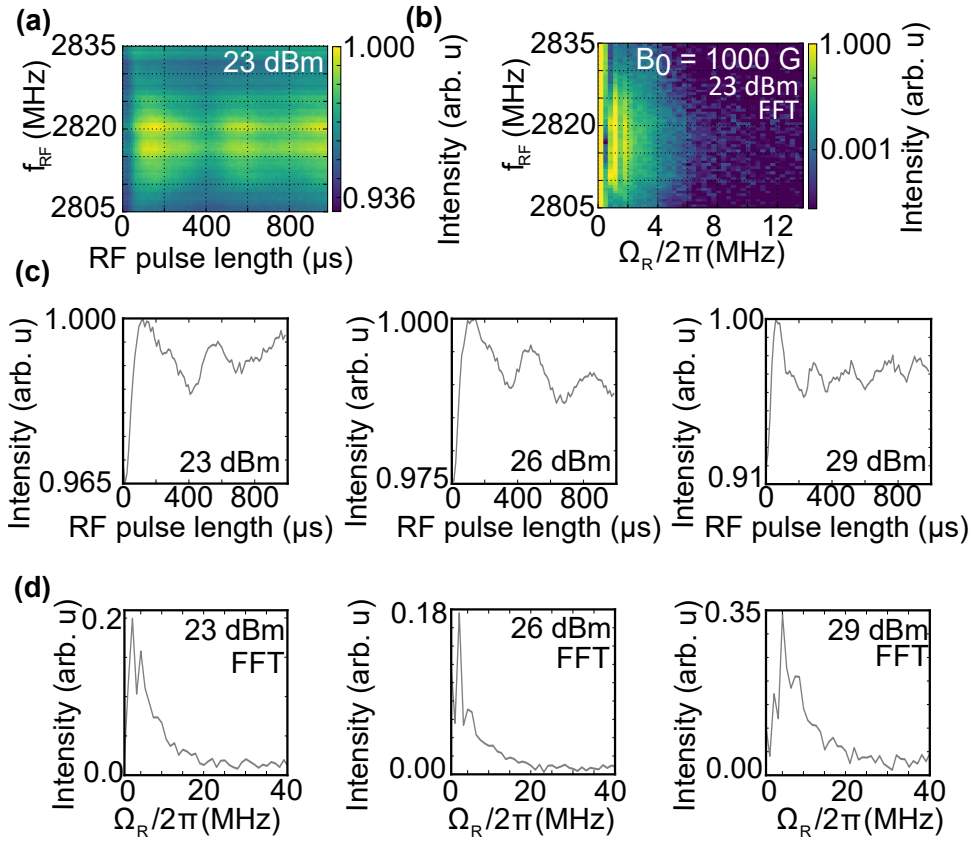

FIGURE 3.18: Rabi oscillations at B_0 = 1000 G. The density plots: The observed Rabi oscillations at RF power of 23 dBm as a function of the RF frequency (a) and the FFT of them (b). The 2D plots: The Rabi oscillations at the RF frequency of 2820 MHz measured at three different RF powers (c) and their FFT (d).

to the optical excitation (Soykal, Dev, and Economou, 2016). I could see a typical exponential decay with $T_2 = 83.9 \pm 1.6\ \mu s$ (Fig. 3.19 (b)). The observed T_2 is, however, shorter than the theoretical expectations for the V_2 centre (Yang et al., 2014) and the value measured for a single V_2 centre at room temperature (Widmann and Lee, 2015). This could be related to the imperfect π pulses and the inhomogeneity of the B_0 field. These observations, however, support the findings by Carter et al. (Carter et al., 2015), related to the fact that the dephased state cannot be refocused by a π pulse due to the oscillating local fields produced by coupled nuclear spins. Thus, the shorter T_2 could be related to electron spin echo envelope modulation (ESEEM). The four sublevels of a $S = \frac{3}{2}$ electronic spin have four different nonzero hyperfine couplings to nearby nuclear spins and thus result in more complex ESEEM than S = 1 systems (Yang et al., 2014; Widmann and Lee, 2015). Furthermore, as reported by Carter et al., the ensemble inhomogeneous broadening induces beating oscillations among the various modulation frequencies, leading to a shortening of the Hahn-echo T_2 (Carter et al., 2015). To further suppress decoherence, we applied the XY-8 dynamical decoupling sequence, which acts as a filter for the environmental magnetic noise (Souza, Álvarez, and Suter, 2012). This sequence has proven to be effective to extend the coherence time of the $S = \frac{3}{2}$ spin ensemble of the V_2 centre from the nuclear

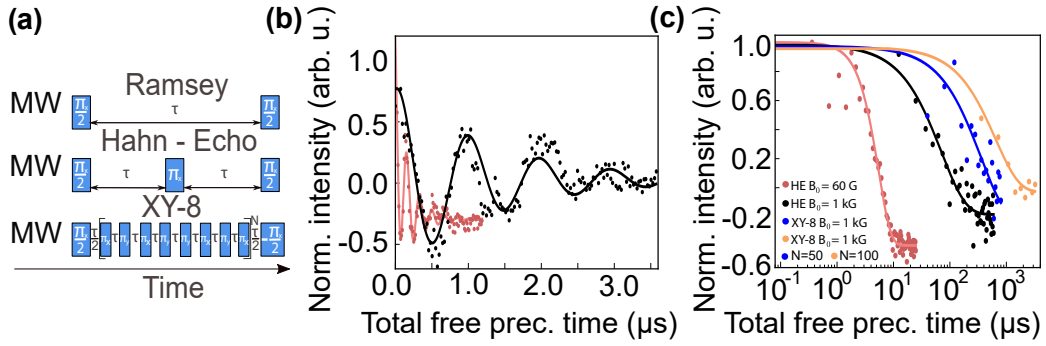

FIGURE 3.19: (a) Applied pulse scheme for Ramsey (FID), Hahn-Echo and XY-8 decoupling sequence. (b) Ramsey measurement at B_0 = 60 G (red) and B_0 = 1000 G black. The measured time $T_2^\star$ is 203 ns and 1.3 μs respectively. (c) Hahn-Echo measurement at B_0 = 60 G (red), B_0 = 1000 G (black) and XY-8 dynamical decoupling with N = 50 (blue) and N = 100 orange repetitions.

spin bath in 4H-SiC (Simin et al., 2017). A repeated decoupling pulse scheme leads to a better suppression of noise, increasing the spin decoherence time with N = 10 and N = 50 repetitions to a value of respectively $T_2 = 286 \pm 7 \mu s$ and $T_2 = 0.60 \pm 0.01 ms$ (3.19 b). These findings suggest that the heteronuclear spin bath in SiC itself provides a diluted spin bath for not only the V_2 centre (Simin et al., 2017; Widmann and Lee, 2015), and DiVacancy defects (Christle et al., 2015), but also the V_1 centre.

Coherent Spin Control at Small Magnetic Fields

In section 3.6, I presented and discussed the spin coherence investigated only at B_0 = 1000 G. I indeed studied spin coherence at T = 5.5 K with both B_0 = 60 G and 1000 G by Ramsey, Hahn echo, and XY-8 dynamical decoupling pulse sequences. Spin measurements were performed by optical excitation resonant with the V_1 = ZPL (861 nm). As discussed above, coherent spin control poses a challenge for a four-level system with a small ZFS. In the following experiments, I take the duration of a π-pulse as the minimum time required for transferring the maximal population from $|\pm\frac{3}{2}\rangle$ to $|\pm\frac{1}{2}\rangle$ subspace. Experimentally, this is signaled by the maximum contrast in the observed Rabi oscillation signals. The Ramsey pulse sequence can be seen in Fig. 3.6 (a). After optical spin polarization, I applied a $\frac{\pi}{2}$ pulse to create a superposition between $|\pm\frac{3}{2}\rangle$ and $|\pm\frac{1}{2}\rangle$ sublevels. Another $\frac{\pi}{2}$ pulse was applied after a free precession time τ for a projective readout before the readout laser pulse. I observed an evolution of the coherent superposition, with a frequency corresponding to the detuning from the resonant transition, and spin dephasing time $T_2^* = 200 \pm 11 ns$ and $1.3 \pm 0.3 \mu s$ at B_0 = 60 G and 1000 G, respectively, as shown in Fig. 3.6 (b). To suppress the inhomogeneous broadening in an ensemble and decouple the spin ensembles from low frequency spin noise sources, I applied a Hahn-Echo sequence. The Hahn-Echo pulse sequence can be seen in Fig. 3.6 (a), which adds a π pulse between two $\frac{\pi}{2}$ pulses, to refocus the dephased spin ensemble due to inhomogeneous broadening and slowly fluctuating magnetic noise. Although the applied π pulses exhibit limited spin control to a single

transition as discussed above, I could see a typical exponential decay with decoherence time $T_2 = 4.4 \pm 0.3\ \mu s$ at B_0 = 60 G (Fig. 3.6 (c)). Since a drastically improved coherence time is expected at a stronger B_0 field by suppressing nuclear spin flip-flops due to a large mismatch of nuclear spin Zeeman levels of ^{29}Si and ^{13}C (Seo et al., 2016), I applied a high magnetic field along the c-axis (0001). The spin decoherence time increases at B_0 = 1000 G to $T_2 = 83.9 \pm 1.6 \mu s$. The observed T_2 is, however, shorter than the theoretical expectations (Seo et al., 2016) and the value measured for a single V_2 centre at room temperature (Golter et al., 2016). This could be related to the imperfect π pulses and the inhomogeneity of the B_0 field for the case B_0 = 1000 G as explained above.

3.6.1 Pulsed Spin Control of a Silicon Vacancy Ensemble

Due to the incoherent mixture of various spin states during the Rabi driving, I find that at various driving strengths, there are no perfect revivals of the population in any subspace of the four-level system. This makes the definition of π, and $\frac{\pi}{2}$ pulses more complex when compared to the well studied two-level system. For both experimental and theoretical analysis, I define a π-pulse as the minimum time required for transferring the maximal population from $|\pm\frac{3}{2}\rangle \rightarrow |\pm\frac{1}{2}\rangle$ subspace. Experimentally, this is signaled by the maximum contrast in the observed fluorescence. But to really know how the state of the four-level system looks during these pulses, I consider the following limits

- $\Omega >> D$, i.e., when the applied B_1 field strength is much stronger than the zero-field splitting. In this limit, the π-pulse will result in

$$|\pm\frac{3}{2}\rangle \rightarrow \frac{1}{\sqrt{2}}(|\pm\frac{3}{2}\rangle \pm |\pm i\frac{1}{2}\rangle) \tag{3.20}$$

  and similarly the $\frac{\pi}{2}$ pulse,

$$|\pm\frac{3}{2}\rangle \rightarrow \frac{1}{\sqrt{3}}(\sqrt{2}|\pm\frac{3}{2}\rangle \pm |\pm i\frac{1}{2}\rangle) \tag{3.21}$$

- $\Omega \approx D$, i.e., when the applied B_1 field strength is of the same order as that of the zero-field splitting, the π-pulse will result in

$$|\pm\frac{3}{2}\rangle \rightarrow \frac{1}{3}[(\sqrt{2}|\pm\frac{3}{2}\rangle - |\mp\frac{3}{2}\rangle) + \sqrt{3}(|\pm\frac{1}{2}\rangle - |\mp\frac{1}{2}\rangle)] \tag{3.22}$$

- $\Omega << D$, i.e., when the applied microwave power is much smaller than that of the zero-field splitting, the π-pulse will result in

$$|\pm\frac{3}{2}\rangle \rightarrow |\pm\frac{1}{2}\rangle \tag{3.23}$$

  The final states after the applied pulses clearly depict the complexity involved by incoherently driving and controlling a four-level system.

CHAPTER 4

Single Silicon Vacancy Centre V_{Si} in Silicon Carbide

Parts of Chapter 4 are published in Roland Nagy et al. Phys. Rev. Applied 9, 034022 and Roland Nagy et al. arXiv:1810.10296 (to be published in Nature Communications).

4.1 Isolation of Single Silicon Vacancy Centres

Investigation for the single V_1 centre started with a pillar sample (Radulaski et al., 2017). The pillars act as a broadband optical waveguide, which provides enhanced photon collection efficiency. The 4H-SiC pillar sample was electron irradiated (2 MeV) with an electron dose of $4 \cdot 10^{14} cm^{-2}$. I found a single V_1 or V_2 defect in one out of 20 pillars. The density of single V_1 defects is higher compared to single V_2 defects. The ratio between single V_1 and V_2 centres is roughly 3:1. The saturation power of a single defect inside a pillar is 190 μW, and the saturated count rate is 14 kcps. The photon detection efficiency in the tested wavelength range (around 900 nm) is roughly a half of the optimized wavelength (around 700 nm) of this Si-APD based detector (Dautet et al., 1993). Since the saturated count rate of a single V_1 centre measured at 5 K with an air objective was 14 kcps, one can expect 30 kcps if I assume the optimized efficiency at the tested wavelength. The Debye-Waller factor (DWF) of the V_1 zero phonon line was measured at 4 K where the phonon side band caused by V_1' is expected to be minimal. The formula how the DWF for V_1 is calculated is $\frac{\int V_1}{\int V_1 + \int V_{PSB}}$. The best measured DWF of V_1 is 40 % as shown in Fig. 4.2. The lowest DWF measured from a single V_1 centre is 37 % as shown in Fig. 4.1 (c). At 80 K, at which V_1 emission is minimized, the measured DWF for V_1' is 19 % (Fig. 4.1 (d)). There is uncertainty in the data caused by the PSB of V_1' and V_1 at 4 K and 80 K, respectively. This indicates that the real DWF of V_1 and V_1' can be higher. If I calculate the DWF at 4 K as the overall number of coherent photons in comparison to the incoherent photons $\frac{\int (V_1 + V_1')}{\int (V_1 + V_1') + \int V_{PSB}}$ I achieve a DWF of 48 % and 41 %, using the data in Fig. 4.2 and the data at 4 K in Fig. 4.1, respectively. The DWF at 80 K calculated with this formula is 32%.

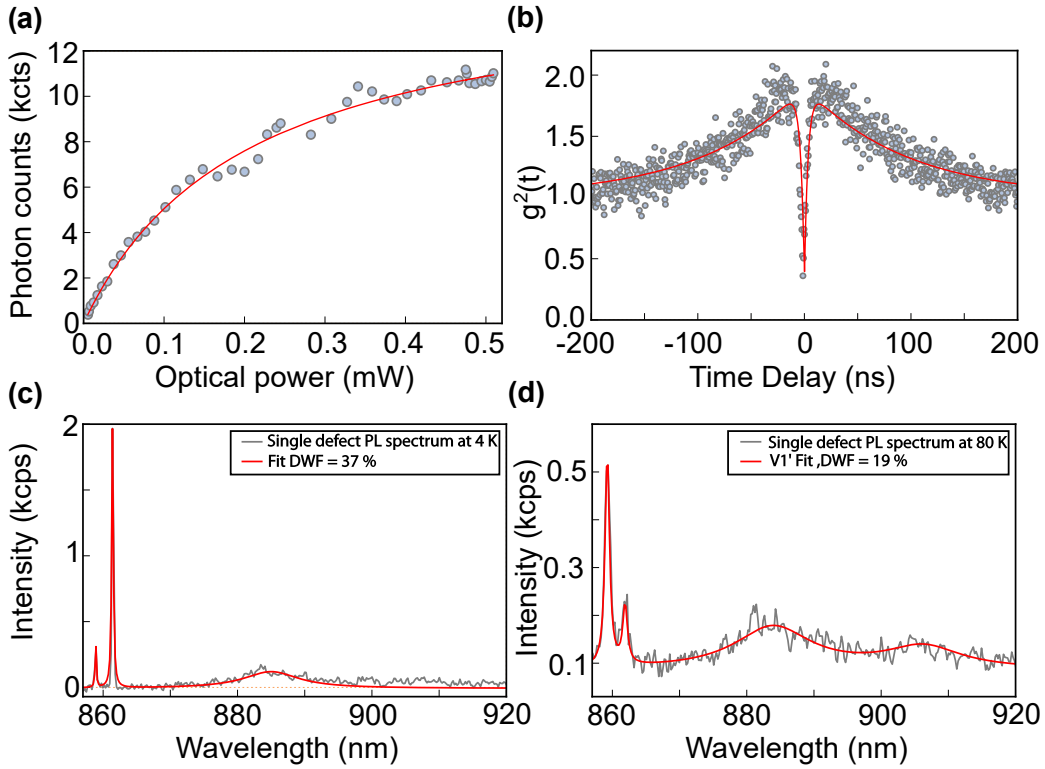

FIGURE 4.1: (a) The optical saturation curve of a single V_1 centre PL emission. (b) The g^2 autocorrelation measurement indicates clearly a single photon emission character, $g^2 < 0.5$. The data in (a) and (b) were taken from the single V_1 centre shown in Fig. 4.2. (c, d) The PL spectra of a single V_1 centre at 4 K and 80 K, respectively. Note that this V_1 centre is different from one in Fig. 4.2

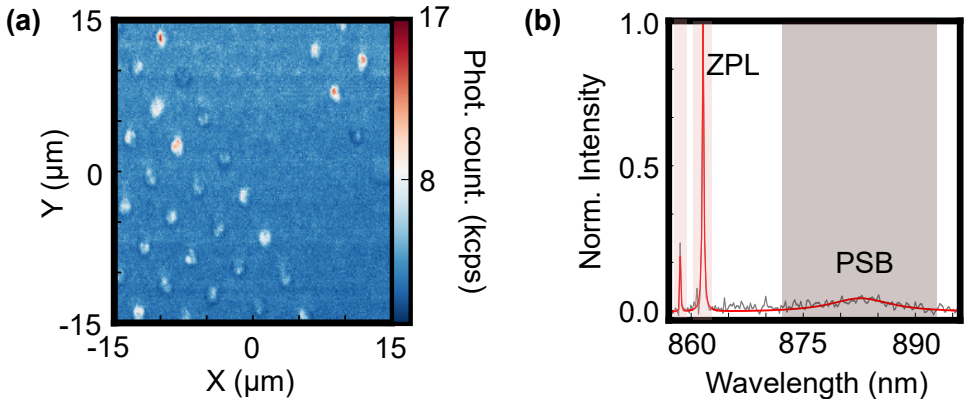

FIGURE 4.2: (a) Confocal fluorescence raster scan showing single silicon vacancy V_1 and V_2 centres in SiC nanopillars at 4K. (b) A single V_1 defect PL spectrum with the $V_1^{'}$ and V1 ZPLs at 858 and 861 nm, respectively.

4.2 Sample Preparation for Resonant Single Defect Studies

The sample was fabricated in Linköping by Prof. Tien Son Nguyen and his colleagues. The electron irradiation was conducted in Japan by the group of Prof. Takeshi Oshima.

The starting material is a 4H-^{28}Si^{12}C silicon carbide layer grown by chemical vapour deposition (CVD) on a n-type (0001) 4H-SiC substrate. The CVD layer is 110 μm thick. The isotope purity is estimated to be 4H-^{28}Si > 99.85 % and ^{12}C > 99.98 %, which was confirmed by secondary ion mass spectroscopy (SIMS) for one of the wafers in the series (Benninghoven, 1975). After chemical mechanical polishing (CMP) of the top layer, the substrate was removed by mechanical polishing and the final isotopically enriched free-standing layer had a thickness of 100 μm. Current-voltage measurements at room temperatures show that the layer is n-type with a free carrier concentration of $6 \cdot 10^{13}$ cm^{-3}. This value is close to the concentration of shallow nitrogen donors of $3.5 \cdot 10^{13}$ cm^{-3}, which was determined by photoluminescence at low temperatures. Deep level transient spectroscopy measurements show that the dominant electron trap in the layer is related to the carbon vacancy with a concentration in the mid 10^{12} cm^{-3} range. Minority carrier lifetime mapping of the carrier shows a homogeneous carrier lifetime of 0.6 μs. Since the lifetime was measured by an optical method with high injection, the real lifetime is expected to be twice as large, i.e. 1.2 μs Kimoto and Cooper, 2014. Such a high minority carrier lifetime indicates that the density of all electron traps should not be more than mid 10^{13} cm^{-3} (Danno, Nakamura, and Kimoto, 2007). To generate a low density of silicon vacancy centres, I used room temperature electron beam irradiation at 2 MeV with a fluence of 10^{12} cm^{-2} to pin the Fermi level ≈ 1.5 eV below the conduction band. The irradiation creates also carbon vacancies, interstitials, anti-sites and their associated defects, but their concentrations are expected to be below mid 10^{12} cm^{-3}. After irradiation, the sample was annealed at 300 °C for 30 minutes to remove some interstitial-related defects. In order to improve light extraction efficiency out of this high refractive index material ($n \approx 2.6$), I fabricate solid immersion lenses using a focused ion beam milling machine (Helios NanoLab 650). The sample was cleaned for two hours in peroxymonosulfuric acid to remove surface contaminations (Widmann and Lee, 2015).

4.3 Resonant Excitation of Single Silicon Vacancy Centres

The defects are optically addressed by confocal microscopy at cryogenic temperatures (T = 4 K). I employ a 730 nm laser diode for off-resonant excitation. A wavelength-tunable diode laser (Toptica DL pro) performs resonant excitation at 861 nm in the zero phonon line of the lowest optical transition with A_2 symmetry, known as V1 line (Nagy et al., 2018b). Another energetically higher transition to an electronic state of E symmetry, called V1' line (Ivády et al., 2017; Nagy et al., 2018b; Janzén et al., 2009), is not investigated in this work. Fluorescence emission is detected in the red-shifted phonon side band (875 - 890 nm). In addition, ground state spin manipulation is performed with microwaves (MW) that are applied via a 20 μm diameter copper wire. Fig. 4.3 (b) illustrates the defect's energy level structure. At zero external magnetic field (B_0 = 0 G), ground and excited state manifolds show pairwise degenerate spin levels $m_s = \pm 1/2$ and $m_s = \pm 1/2$, with zero-field splittings (ZFS) of $2D_{gs}$ and $2D_{es}$, respectively. Previous studies constrained

$2D_{gs} < 10MHz$ (Ivády et al., 2017; Nagy et al., 2018b; Sörman et al., 2000) and here I determine $2D_{gs} = 4.5 \pm 0.1$ MHz, see Section 4.4.1. In order to investigate the excited state structure, I use resonant optical excitation. I apply a strong MW field at 4.5 MHz to continuously mix the ground state spin population, and wavelength-tune simultaneously the 861 nm Toptica laser across the optically allowed transitions. As shown in Fig. 4.4 (a), I ob-

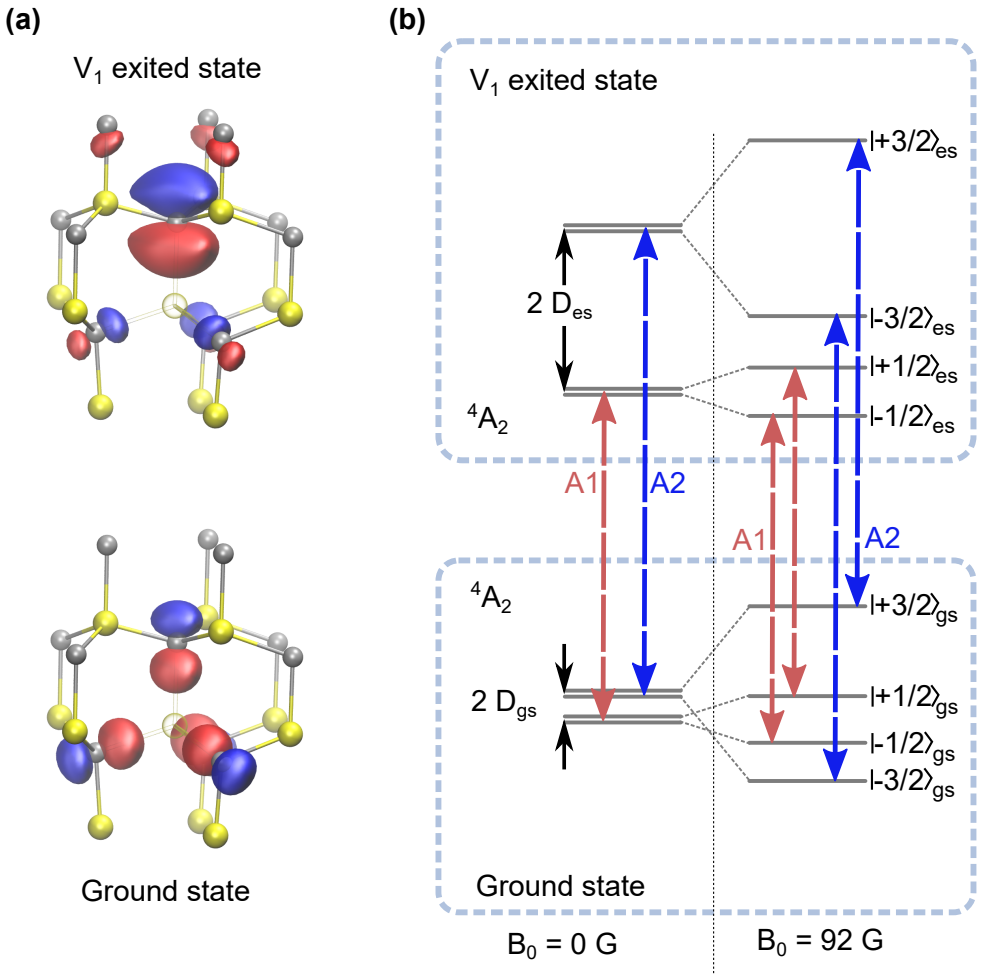

FIGURE 4.3: Optical transitions of the silicon vacancy in 4H-SiC. (a) Crystalline structure of 4H-SiC with a silicon vacancy centre at a hexagonal lattice site. Upper (lower) graph shows the square moduli of the defect wave functions of the V_1 excited (ground) state, as calculated by density functional theory. Red (blue) shaded areas symbolise that the wave function has a positive (negative) sign. The yellow and grey spheres represent silicon and carbon atoms, respectively, and the crystallographic c-axis is aligned vertically in this figure. (b) Ground and excited state level scheme with and without a magnetic field applied along the c-axis. Red (blue) optical transitions labelled A1 (A2) connect spin levels $m_s = \pm 1/2 (m_2 = \pm 3/2)$.

serve two strong fluorescence peaks, labelled A_1 and A_2. The peak separation of 980 ± 10 MHz corresponds to the difference between the ground and excited state ZFS. As shown in Section 4.4.2, I use coherent spin manipulation to infer a positive excited state ZFS,

i.e. $2D_{es}$ = 985 ± 10 MHz, which is in line with the results of first principles density functional theory. To determine optical selection rules, I apply an external magnetic field of B_0 = 92 G precisely aligned along the uniaxial symmetry axis of D_{gs}, which is parallel to the c-axis of 4H-SiC, such that the ground state Zeeman spin splitting exceeds the optical excitation linewidth (see Fig. 4.3 (b)). I observe no shift of the optical resonance lines, corroborating my assignment of $A_{1,2}$ as spin-conserving optical transitions between ground and excited states. Further, I observe no spin-flip transitions, which would show up as additional peaks in the spectra in Fig. 4.4 (a) at approximately ± 258 MHz. However, as I will show later, spin-flips can still occur through nonradiative decay channels. More-

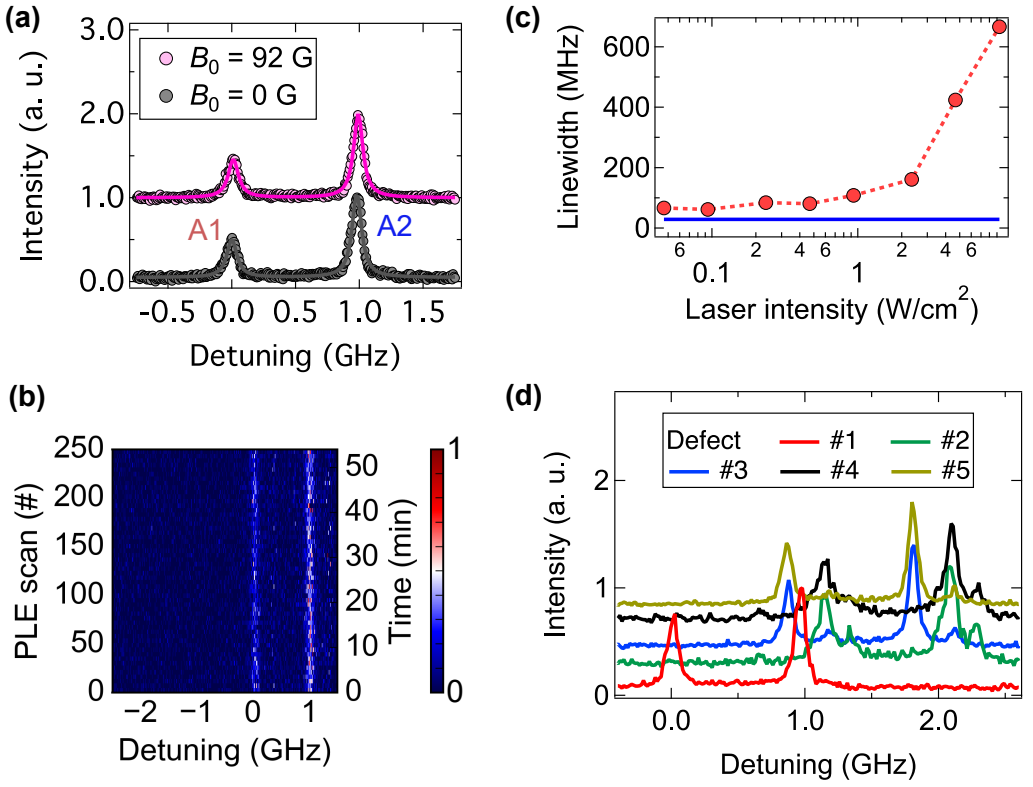

FIGURE 4.4: (a) Resonant absorption spectrum of a single vacancy centre at B_0 = 0 G and B_0 = 92 G. Lines are fits using a Lorentzian function. (b) Repetitive resonant absorption scans at B_0 = 0 G over 52 minutes without any sign of line wandering. (c) Absorption linewidth of the peak A2 as a function of the resonant pump laser intensity. Below 1 W/cm^2 no power broadening is observed and the linewidth is close to transform limited as indicated by the blue line. (d) Resonant absorption spectra of five single defect centres, showing several defects with overlapping lines.

over, as the presence of a magnetic field does not alter the peak separation, I confirm that ground and excited state g-factors are identical (see Section 4.4.2, (Wagner et al., 1999)). Fig. 4.4 (b) shows repetitively recorded excitation spectra for which I find exceptionally stable lines over an hour time scale. To underline that the defect's intrinsic symmetry indeed decouples it from strain and stray charges in its local environment, I perform resonant excitation studies on four other defects. As shown in Fig. 4.4 (d), the peak separation

of all defects is nearly identical. In addition, all resonant absorption lines are inhomogeneously distributed over only a few 100 MHz, allowing us to identify several defects with overlapping emission. Our results suggest a very low strain sensitivity, consistent with the Kramer's degeneracy of half-integer spin systems, and almost identical dipole moment in the ground and excited state (see 4.3.1). My findings are intimately related to the symmetry properties of the defect, showing A-type states in ground and first excited state with similar electron density distributions. Unlike inversion symmetry, this does not preclude the existence of an electric dipole moment in ground and excited state but restricts its orientation to the symmetry axis of the defect. A similar line of arguments shows that optical transitions among those states are allowed because of the alternating phase of the wavefunctions nevertheless, if excitation is polarized along the symmetry axis of the defect, i.e. the c-axis of the crystal. This is indeed found in my experiments. Advanced quantum information applications based on spin-photon entanglement require that the quantum system emits transform-limited photons. I measure this via the excitation linewidth of the optical transitions. In Fig. 4.4 (c), I show that for excitation intensities below 1 W/cm^2, the linewidth approaches 60 MHz. Considering the 5.5 ns excited state lifetime (see Fig. 3.7 (Nagy et al., 2018b)), this is only twice the Fourier-transform limit, and might be explained by small residual spectral diffusion.

4.3.1 Electrical Dipole Moment of the Silicon Vacancy Centre in 4H-SiC

In Section 4.3, I reported studies on resonant optical excitation spectra that show an outstanding spectral stability in contrast to the nitrogen-vacancy (NV) centre in diamond (Nagy et al., 2018b). I attribute the small inhomogeneous distribution (see Fig. 4.4 (b)) to a low sensitivity of the defects to surrounding electric field fluctuations originating from other defects. Since this may be related to a small dipole moment of the V_1 centre in 4H-SiC, we test this hypothesis by performing theoretical calculations as described in the following. We calculate the change in the polarization for the excitation process between $^4A_2$ ground and $^4A_2$ excited states of the negatively charged V_1 centre in 4H-SiC (silicon vacancy defect on a hexagonal lattice site). We compare these results with the ones obtained for the nitrogen-vacancy (NV) centre in diamond. The group of Prof. Adam Gali applied density functional theory (DFT) for electronic structure calculation and geometry relaxation using the plane-wave-based Vienna Ab initio Simulation Package (VASP) (Kresse and Furthmüller, 1996b; Kresse and Hafner, 1993; Kresse and Furthmüller, 1996a; Paier et al., 2006). The core electrons are treated in the projector augmented-wave formalism (Blöchl, 1994). For the 4H-SiC supercell, calculations are performed with 420 eV plane wave cut-off energy and with Γ centred $2\cdot2\cdot2$ k-point mesh to sample the Brillouin zone. For the diamond supercell, we use 420 eV plane wave cut-off energy and Γ-point to sample the Brillouin zone. We apply Perdew-Burke-Ernzerhof functional in these calculations (Perdew, Burke, and Ernzerhof, 1996). The model for the silicon vacancy defect in bulk 4H-SiC is constructed using a 432-atom hexagonal supercell, whereas we use the 512-atom simple cubic supercell to model the NV centre in diamond. The excited state electronic structure and geometry is calculated by constraint occupation of states, or Delta

Self-Consistent Field (ΔSCF) method (Gali et al., 2009). We calculate the permanent polarisation in ground and excited states, and their difference, in order to infer the coupling to the optical transition. To this end, we use the VASP implementation of both Born effective charge calculation using density functional perturbation theory (DFPT) (Gajdoš et al., 2006) and the Berry phase theory of polarization (King-Smith and Vanderbilt, 1993; Vanderbilt and King-Smith, 1993; Resta, 1994). In a DFT calculation, one can define the change in macroscopic electronic polarisation (P) as an adiabatic change in the Kohn-Sham potential (V_{KS})

$$\frac{\partial P}{\partial \lambda} = \frac{-ife\hbar}{\Omega m_e} \sum_k \sum_{n=1}^{M} \sum_{m=M+1}^{\infty} \frac{\langle \Psi^\lambda_{kn} | \hat{p} | \Psi^\lambda_{km} \rangle \langle \Psi^\lambda_{km} | \frac{\partial V_{KS}}{\lambda} | \Psi^\lambda_{kn} \rangle}{(\epsilon^\lambda_{kn} - \epsilon^\lambda_{km})^2} + c.c., \tag{4.1}$$

where f is the occupation number, e the elemental charge, m_e the electron mass, Ω the cell volume, M the number of occupied bands, $\hat{p}$ the momentum operator, λ is the adiabatic parameter, ϵ is the band energy. The first part of the equation corresponds to the electronic part of the permanent polarization (p_{el}), whereas the second part corresponds to the contribution of ions (p_{ion}) to the permanent polarization. In a periodic gauge, where the wavefunctions are cell-periodic and periodic in the reciprocal space, the permanent polarization takes a form similar to the Berry phase expression

$$\Delta P = \frac{ife}{8\pi^3} \sum_{n=1}^{M} \int_{BZ} dk \langle u_{kn} | \nabla_k | u_{kn} \rangle \tag{4.2}$$

Using DFPT, $\nabla_k | u_{kn} \rangle$ can be calculated from the Sternheimer equations with similar self-consistent iterations as in DFT:

$$(H_k - \epsilon_{kn} S_k) \nabla_k | u_{kn} \rangle = \frac{-\partial (H_k - \epsilon_{kn} S_k)}{\partial_k} | u_{kn} \rangle \tag{4.3}$$

where n is the refractive index, $\hbar w$ is the transition energy, μ is the optical transition dipole moment, ϵ_0 is the vacuum permittivity, and c is the speed of light. μ is proportional to the integrated imaginary dielectric function (I) of the given transition:

$$|\mu|^2 = \frac{\epsilon_0 V}{\pi} \int \Im \epsilon_r(E) dE = \frac{\epsilon_0 V I}{\pi} \tag{4.4}$$

where V is the volume of the supercell. The results of the Berry phase evaluation for macroscopic dipole moment calculation are shown in Tables 4.1 and 4.2 for the V_1 centre in 4H-SiC and the NV centre in diamond, respectively. The change in the total dipole moment is about 20 times larger for NV centre in diamond with respect to that for V_1 centre in 4H-SiC. This means that the V_1 centre has intrinsically low coupling strength between optical transition and stray electric fields.

Preliminary studies have been performed to constrain Δp_{tot} via Stark shift control of optical transition frequencies. To this end, I spanned two parallel copper wires over the sample in order to apply an electric field. The wires were separated by approximately 100 μm and voltages up to ± 200 V were applied. I note that by applying higher electric fields

Transition	$\Delta p_{ion}(e\mathring{A})$	$\Delta p_{el}(e\mathring{A})$	$\Delta p_{tot}(e\mathring{A})$
gr → ex(V_1)	0.000	0.044	0.044

TABLE 4.1: Macroscopic electric dipole moment of the hexagonal lattice site silicon vacancy defect (V_1 centre) as calculated within the Berry phase approximation.

Transition	$\Delta p_{ion}(e\mathring{A})$	$\Delta p_{el}(e\mathring{A})$	$\Delta p_{tot}(e\mathring{A})$
gr → ex	0.061	0.842	0.903

TABLE 4.2: Macroscopic electric dipole moment of the NV centre in diamond as calculated with-in the Berry phase approximation.

led to electrical breakdown in the cryostat's low-vacuum atmosphere. Considering the relative permittivity of 4H-SiC ($\epsilon_r \approx 10$), this results in an estimated in-crystal field of about $\pm$ 200 kV/m. Two experiments were performed, one in which the electric field was applied along the crystal's c-axis, and a second one in which the field was orthogonal to the c-axis. I performed resonant excitation studies at zero magnetic field (B_0 = 0 G) as a function of the electric field strength, in analogy to the studies shown in Fig. 5.3 a. A change in the width or separation of the A1 and A2 optical transitions would indicate electric field sensitivity through which Δp_{tot} can be inferred. I observed, however, neither effect within the investigated electric field range as it can be seen in Fig 4.5. In my current experimental setup, I can infer peak width and separation with a precision of approximately $\pm$ 12 MHz. According to theory, an electric field perpendicular to c-axis has no coupling to V_1 centre and the coupling is maximum with direction of the electric field parallel to c-axis. By assuming an homogeneous crystal field along the c-axis of $\pm$ 200 kV/m, I can constrain the Stark shift tuning coefficient to be $\leq$ 60 MHz/(MV/m). This is at least two orders of magnitude smaller than reported for NV centres in diamond ($\approx$ 6.3 GHz/(MV/m)) (Tamarat et al., 2006), such that I estimate $\Delta\, p_{tot} < 0.009$. However, theory implies that the coupling coefficient is about an order magnitude smaller for V_1 centre in SiC than that for NV centre in diamond. I show below that a compensating field can be developed when both electric field and illumination are applied that can explain the experimental data. I note that there is a variation in the position of zero-phonon-line (ZPL) for various single V_1 centres in the SiC sample of about few 100 MHz but the stability of the ZPL of each investigated single V_1 centre is within 60 MHz after repetitive PLE measurements. This implies that charge redistribution occurs upon illumination for each single V_1 centre even without applying external electric field. Understanding of these features requires a close inspection of the SiC sample. First of all, the nitrogen donor concentration is very low $3.5 \cdot 10^{13}$ cm^{-3}, thus the resistivity is very high. This means that the exchange of carriers is very limited, and the concept of Fermi-level does not apply to the entire SiC sample. Si-vacancies are created by 2 MeV irradiation of electrons. According to previous studies (Steeds et al., 2001), the energy threshold of kicking off C and Si atoms in SiC lattice is about 120 keV and 250 keV, respectively. The application of 2 MeV energy should lead to a cascade process where the Si or C atoms kick out other C and Si atoms from the lattice. After annealing at 300

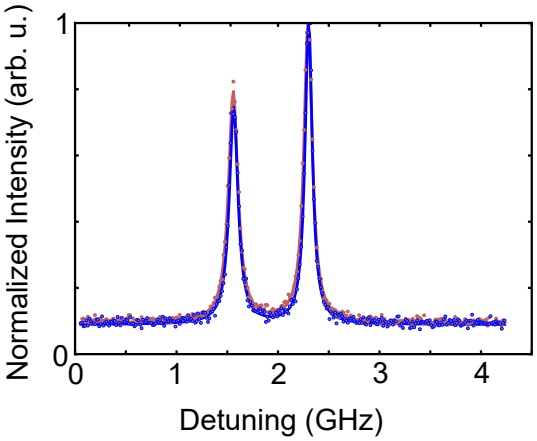

FIGURE 4.5: Stark shift measurement of a single silicon vacancy in 4H-SiC. The blue and red lines show a photoluminescence excitation (PLE) measurement. The blue line corresponds to + 200 V and the red line to - 200 V applied parallel to the optical axis of the silicon vacancy centre. Neither the blue nor the red line shows a shift in absorption frequency.

°C, the Frenkel-pairs disappear in the form of either recrystallization or antisite defects. The antisite defects are not activated by near infrared illumination. Besides, carbon interstitial clusters and vacancies may form. Interestingly, Si-vacancy has two faces in SiC crystal: the simple Si-vacancy which is basically a deep acceptor and the carbon antisite-vacancy pair (CAV) complex which has donor levels. Furthermore, the amphoteric carbon vacancies are left after the materials processing. Carbon vacancies are expected to appear in majority because they have the lowest formation energy among the considered defects (Ivády et al., 2017) and threshold energy to form by electron irradiation (Kresse and Furthmüller, 1996b). The negative charge of the Si-vacancy should be donated by a nearby defect. The average distance between nitrogen donors is about 306 nm in the SiC sample, thus only few Si-vacancies will reside near (≈50 nm) the nitrogen donor. Among the considered vacancy-like defects, the CAV defect has the shallowest donor level (Ivády et al., 2017), which can be activated by near infrared illumination. The simplest model is that a positively charged defect resides near the negatively charged Si-vacancy, the V_1 centre. According to our calculations, the positively charged donor defect (N-donor or CAV) should sit around ≈ 40 nm around the V_1 centre at different lattice sites going from the symmetry axis of the defect toward the basal plane, in order to experience few 100 MHz variation in the ZPL of various V_1 centres. The small spectral diffusion may be understood by assuming that another donor defect lies near the V1 centre with about the same distance but another location where the illumination will activate that donor, and the resulting electron, free carrier, will be captured by the previously positively charged donor defect. According to a previous study (Wallace et al., 2015), low energy Si atoms will produce vacancy defects in about 10 nm region, thus Si atoms that are created by 2 MeV electron irradiation have much higher kinetic energy and should produce vacancies, antisites and interstitials at larger distances, around 40 nm and larger distances. By applying an external electric field that is parallel to the symmetry axis of the V_1 centre, illumination

will again ionize a donor defect but the electric field will drag the electron in the opposite direction of the electric field. One of the carbon vacancies around V_1 centre will capture this electron, and the positive donor and negative carbon vacancy will form an electric field that mostly screens the external electric field. We find that if these defects are both 40 nm apart from the V_1 centre along the symmetry axis then they shield the external electric field to about 10 % of its magnitude. As a consequence, the resulting Stark-shift agrees with the experimental data $\Delta\, p_{tot} < 0.09$. Although, this estimation is crude as the statistics about the point defects around V_1 centre is not known but our scenario still explains all the experimental findings. We think that both the small coupling constant of the V_1 centre and the shielding effects created by the donor and acceptor point defects around the V_1 centre are responsible for the spectral stability of the V_1 centre.

4.3.2 Orientation of the Electrical Dipole and Polarization of Emitted Photons from Silicon Vacancy Centres in 4H-SiC

Previous studies have already shown that the silicon vacancy centre at a hexagonal lattice site (V_1 centre) is most effectively excited using a linearly polarized off-resonant laser whose polarization is parallel to the crystal's c-axis (Janzén et al., 2009; Nagy et al., 2018b). Here, I investigate the behavior of the individual optical transitions A1 and A2 under resonant excitation. As I have shown in Section 4.3, when applying a magnetic field, no additional optical transitions are observed, supporting the absence of circularly polarized optical transitions. In the following, I show that both transition dipoles are indeed linearly polarized and parallel to each other. To this end, I applied broadband microwaves in order to continuously mix the ground state populations, and performed resonant optical excitation along either A1 or A2 at an intensity of about 1 W/cm^2. The polarization of the excitation laser was adjusted by a half-wave plate (HWP), the efficiency of the excitation was inferred from the detected fluorescence intensity in the phonon sideband. Fig. 4.6 shows the experimental results. In both cases, tuning the HWP leads to near-perfect sinusoidal oscillations, demonstrating that linear dipole transitions are excited, which are parallel to each other.

4.4 Optically Detected Magnetic Resonance on Single Silicon Vacancy Centres

Realizing a spin-to-photon interface for quantum information applications requires high-fidelity spin state initialization, manipulation and readout (DiVincenzo, 2000a). Previous theoretical models (Soykal, Dev, and Economou, 2016) and ensemble-based measurements (Nagy et al., 2018b) have indicated that continuous off-resonant optical excitation of V_{Si} eventually leads to a decay into a metastable state manifold (MS), followed by rather non-selective relaxation into the ground state spin manifold. Here, I use resonant optical excitation to strongly improve spin state selectivity. As shown in Fig. 4.7(a), I apply a magnetic field of B_0 = 92 G, allowing to selectively address transitions within the ground

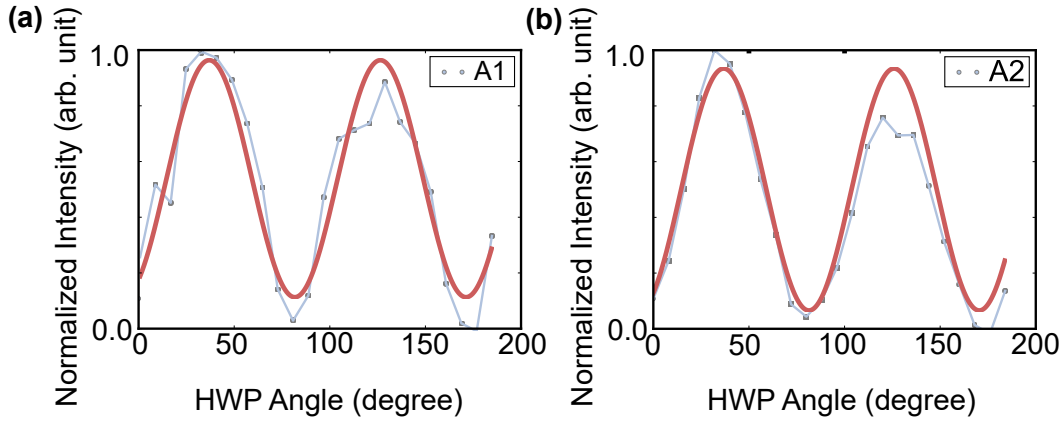

FIGURE 4.6: Measuring the polarization of the optical dipole transitions A1 (a) and A2 (b). Dots are data, and blue lines are sinusoidal fits. The high contrast in the observed oscillations shows that both dipoles are linear and parallel to each other.

state spin manifold via MW excitation. I first excite the system along the A2 transition (linking the $m_s = \pm 3/2$ spin states), which eventually populates the system into the $m_s = \pm 1/2$ ground state via decays through the MS. Then, I perform optically detected mag-

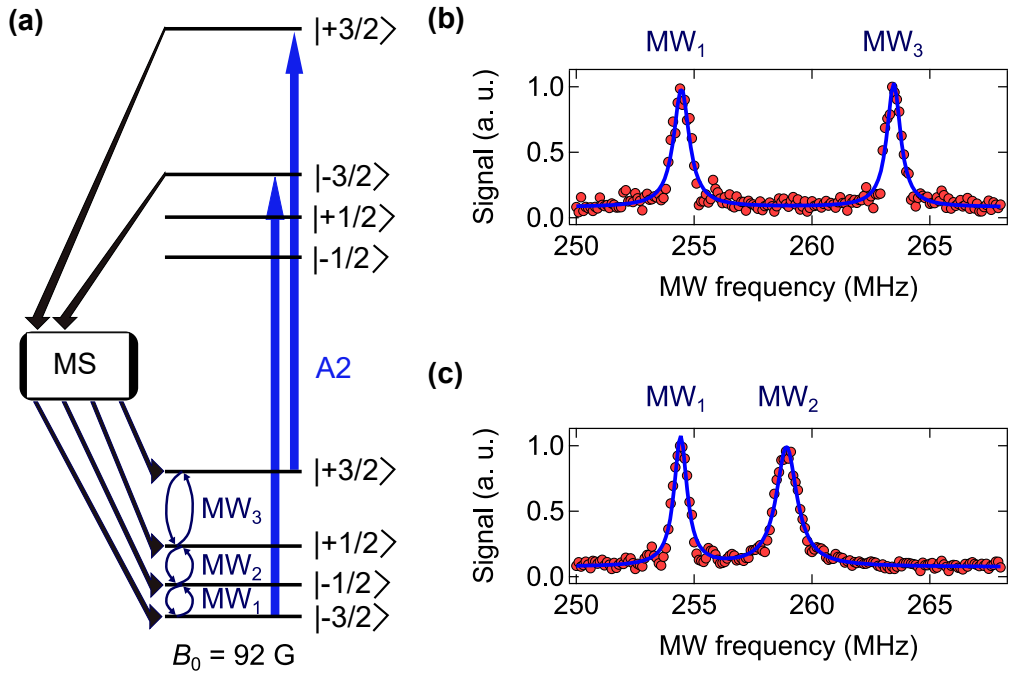

FIGURE 4.7: Optically detected magnetic resonance. (a) Level scheme indicating the used optical transition (A2) and microwave fields MW_1, MW_2 and MW_3. Spin flips occur via nonradiative channels involving metastable states (MS). (b) ODMR signal of the ground state after initializing the system into $|\pm 1/2\rangle_{gs}$. (c) ODMR signal after initialization into $|-1/2\rangle_{gs}$. Blue lines are fits using Lorentzian functions. All data are normalized raw data, i.e. without background subtraction.

netic resonance. For this, I apply narrowband microwave pulses in the range of 245 - 275

MHz, followed by fluorescence detection during an optical readout pulse on the A2 transition. As shown in Fig. 4.7 (b), I observe two spin resonances at the magnetic dipole allowed transitions, $|-\frac{1}{2}\rangle_{gs} \leftrightarrow |-\frac{3}{2}\rangle_{gs}$ and $|+\frac{1}{2}\rangle_{gs} \leftrightarrow |+\frac{3}{2}\rangle_{gs}$ at 253.5 MHz (MW_1) and 262.5 MHz (MW_3), respectively. To observe the centre resonance at 258.0 MHz (MW_2), I need to imbalance the population between $|-\frac{1}{2}\rangle_{gs}$ and $|+\frac{1}{2}\rangle_{gs}$. To this end, I combine the initial resonant laser excitation pulse on A2 with MW_3. MW_3 continuously depopulates $|+\frac{1}{2}\rangle_{gs}$, such that the system is eventually pumped into $|-\frac{1}{2}\rangle_{gs}$. After applying microwaves in the range between 245 - 275 MHz, the optical readout pulse is also accompanied by MW_3, which transfers population from $|+\frac{1}{2}\rangle_{gs}$ to $|+\frac{3}{2}\rangle_{gs}$. This effectively allows us to detect a fluorescence signal from spin population in $|+\frac{1}{2}\rangle_{gs}$. As shown in Fig. 4.7 (c), I observe the two expected resonances for $|-\frac{1}{2}\rangle_{gs} \leftrightarrow |-\frac{3}{2}\rangle_{gs}$ and $|-\frac{1}{2}\rangle_{gs} \leftrightarrow |+\frac{1}{2}\rangle_{gs}$ at 253.5 MHz (MW_1) and 258.0 MHz (MW_2), respectively. Unless mentioned otherwise, I now always initialize the system into $|-\frac{1}{2}\rangle_{gs}$ using the above-described procedure and read out the spin state population of the $|+\frac{3}{2}\rangle_{gs}$ levels with a 1 μs long laser pulse resonant with the A2 transition.

4.4.1 Sign of the Excited State Zero Field Splitting (ZFS_E)

Using a wavemeter (Coherent WaveMaster) with a resolution of 0.1 GHz, I inferred that the A2 optical transition is the one at higher energy. I now want to infer whether this transition links the spin sublevels $|\pm\frac{3}{2}\rangle_{gs}$ (resulting in a positive sign of D_{es}) or the sublevels $|\pm\frac{1}{2}\rangle_{gs}$ (resulting in a negative sign of D_{es}). For this, the experimental results of the Rabi oscillations between $|-\frac{1}{2}\rangle_{gs}$ and $|+\frac{1}{2}\rangle_{gs}$ are relevant (see Fig 4.8 (a)). I now consider both cases of D_{es} (positive and negative). Assuming that D_{es} is positive, the A2 optical transition links the $m_s = \pm 3/2$ sublevels, such that the ground state spin initialization procedure (laser excitation on the A2 transition and continuous MW_3 excitation in order to depopulate $|\pm\frac{1}{2}\rangle_{gs}$ leads to near deterministic population of $|-\frac{1}{2}\rangle_{gs}$. Thereafter, MW_2 is applied for τ_{Rabi}, followed by a population swap (π-pulse at MW_3) between $|+\frac{1}{2}\rangle_{gs}$ and $|+\frac{3}{2}\rangle_{gs}$, and eventual population readout of the states $|\pm\frac{3}{2}\rangle_{gs}$. This experiment should lead to clearly visible Rabi oscillations, starting at a minimum intensity. Assuming on the other hand that D_{es} is negative, then A2 links the $m_s = \pm 1/2$ sublevels, such that the ground state spin initialization procedure would lead to a near deterministic population of m_s = - 3/2. Thereafter, MW_2 is applied for τ_{Rabi}, which does not alter the ground state spin population at all. In addition, the population swap π-pulse at MW_3 has also no effect. As a consequence, the eventual population readout of the states $m_s = \pm 1/2$ should lead to no observable signal. The experimental results in Fig 4.8(a) clearly support therefore that the excited state zero field splitting is positive, i.e. $|2D_{es}|_{es} = 985 \pm 10$ MHz. I note that our ab initio calculations (Ivády et al., 2017) resulted in positive zero-field constant both for the ground and excited states that strongly supports the analysis of experimental results.

4.4.2 Landé g-Factor and Optical Transition Energies of the First Excited State

The spin Hamiltonian of ground and excited states with an external axial magnetic field is:

$$H_{gs,es} = D_{gs,es}S_z^2 + g_{gs,es}\mu_B B_0 S_z \tag{4.5}$$

Here, the subscripts gs and es denote ground and excited states, respectively. $2D_{gs,es}$ denotes the zero field splitting, S_z is the spin projection operator in the z-direction, $g_{gs,es}$ is the Lande g-factor, μ_B is the Bohr magneton, and B_0 the strength of the axial magnetic field. Diagonalization of the Hamiltonian leads to four spin-conserving optical transition energies:

- $2(D_{es} - D_{gs}) + \frac{3}{2}\mu_B B_0(g_{es} - g_{gs}) + \Delta E_{gs,es}$ for transitions between $m_s = +\frac{3}{2}$ sublevels.
- $\frac{1}{2}\mu_B B_0(g_{es} - g_{gs}) + \Delta E_{gs,es}$ for transitions between $m_s = +\frac{1}{2}$ sublevels.
- $-\frac{1}{2}\mu_B B_0(g_{es} - g_{gs}) + \Delta E_{gs,es}$ for transitions between $m_s = -\frac{1}{2}$ sublevels.
- $2(D_{es} - D_{gs}) - \frac{3}{2}\mu_B B_0(g_{es} - g_{gs}) + \Delta E_{gs,es}$ for transitions between $m_s = -\frac{3}{2}$ sublevels.

Here, $\Delta E_{gs,es} \approx 1.44$ eV is the energy difference between ground and excited states. At zero magnetic field, one expects two pairwise degenerate spin-conserving optical transitions for the sublevels $m_s = \pm 1/2$ and $m_s = \pm 3/2$. For the latter transition (A2 in my notation), I observe a linewidth (full width at half maximum (FWHM)) of $\Delta f_{B_0=0G} = 86.6 \pm 1.6$. At $B_0 \neq 0$ G, one would expect to see four optical spin-conserving transitions, provided that there is a sizable difference in the Lande factors g_{gs} and g_{es}. As shown in Fig. 4.4 (a), I do not observe any additional transitions at $B_0 = 92$ G. The linewidth of the A2 transition remains essentially unchanged, i.e. $\Delta f_{B_0=92G} = 87.7 \pm 1.6$ MHz. Consequently, I conclude that the change in linewidths is $\Delta f_{B_0=92G}$ - $\Delta f_{B_0=0G} = 0.1 \pm 2.3$ MHz. I assume now that the optical transitions between the sublevels $m_s = \pm 3/2$ show a Lorentzian profile, i.e. $I_\pm \propto \frac{(\frac{a}{2})^2}{(f \pm \frac{f_0}{2})^2 + (\frac{a}{2})^2}$, in which $I_\pm$ denotes the intensity of the $m_s = \pm 3/2$ transition, $a = \Delta f_{B_0=0G}$ is the FWHM of each transition at $B_0 = 0$ G, f is the laser frequency offset with respect to the centre of the resonance, and $\pm\frac{f_0}{2}$ is the displacement of the $m_s = \pm 3/2$ transition at $B_0 \neq 0$ G. There exists an analytic solution for the apparent FWHM of the sum of two displaced Lorentzian functions:

$$\Delta f_{DoubleLorentz} = \sqrt{2f_0^2 - \sqrt{5f_0^4 + 8f_0^2a^2 + 16a^4}} \tag{4.6}$$

Using this equation, I infer a displacement of $f_0 = 0.2 \pm 11.6$ MHz. By using this result, I now infer the difference in ground and excited state Lande g-factors:

$$g_{es} - g_{gs} = \frac{\Delta f_{DoubleLorentz}}{3\mu_B B_0} = (0.5 \pm 30.0) \cdot 10^{-3} \tag{4.7}$$

Since previous studies (Janzén et al., 2009) have already reported $g_{gs} = 2.0028$, I determine the excited state Lande factor to be $g_{es} = 2.0033 \pm 0.0300$. In addition, as the ground and excited state g-factors have been determined to be nearly identical, if spin-flipping

optical transitions ($|\Delta m_s| = 1$) were allowed, they should appear at $\pm g\mu_B B_0 \approx \pm 258$ MHz compared to the spin-conserving transitions. However, such transitions have not been observed as shown in Fig. 4.4 (a).

4.5 Spin Coherence and Hyperfine Coupling

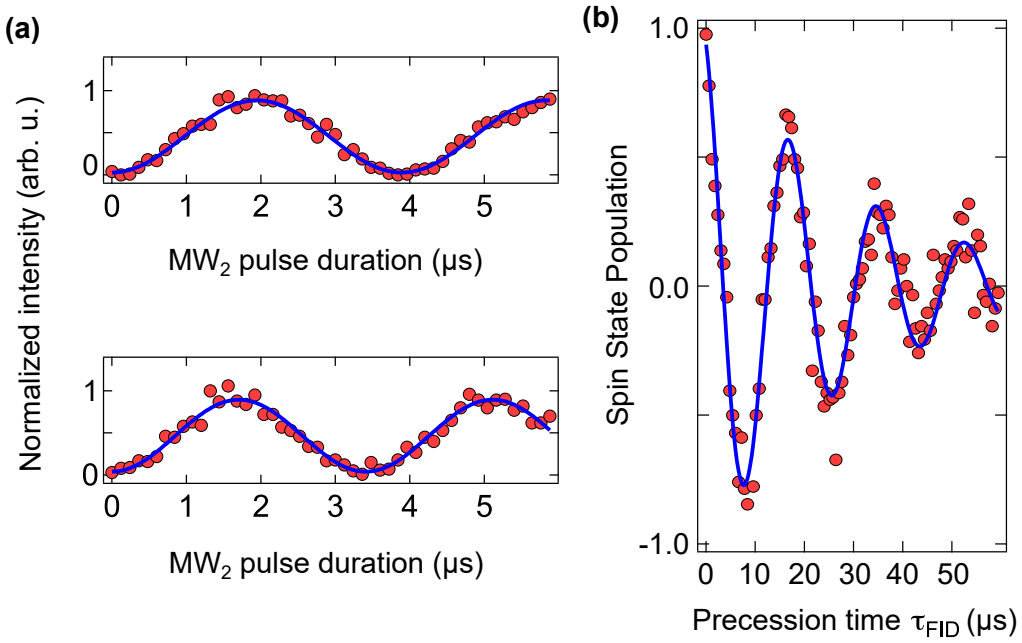

FIGURE 4.8: Spin manipulation and coherence. The system is always initialized into $|-1/2\rangle_{gs}$ using resonant excitation along A2 and MW_3. This step is followed by a Rabi sequence ($MW_{1,2}$), an optional population swap ($|+1/2\rangle_{gs} \leftrightarrow |+3/2\rangle_{gs}$), and optical readout. (a) Rabi oscillations for ($|-1/2\rangle_{gs} \leftrightarrow |-3/2\rangle_{gs}$) (upper panel) and ($|+1/2\rangle_{gs} \leftrightarrow |-1/2\rangle_{gs}$) (lower panel). Blue lines are sinusoidal fits. All data are raw data. (b) Free induction decay measurement yielding $T_2^\star = 30 \pm 2\mu s$, and the blue line is a fit.

I first demonstrate coherent spin state control via Rabi oscillations. Fig. 4.8(a) shows the Rabi oscillations between $|-\frac{1}{2}\rangle_{gs} \leftrightarrow |-\frac{3}{2}\rangle_{gs}$. After spin state initialisation, I apply MW_1 for a time τ_{Rabi} to drive population towards $|-\frac{3}{2}\rangle_{gs}$, followed by optical readout. To observe oscillations between $|-\frac{1}{2}\rangle_{gs} \leftrightarrow |+\frac{1}{2}\rangle_{gs}$, the system is initialised, MW_2 is applied for a time τ_{Rabi}, followed by a population transfer from $|+\frac{1}{2}\rangle_{gs} \rightarrow |+\frac{3}{2}\rangle_{gs}$ using a π-pulse at MW_3, and eventual state readout. Fig. 4.8 (a) shows the experimental results from which I deduce Rabi oscillation frequencies of 257.5 kHz and 293.8 kHz. The frequency ratio of $1.14 \approx \sqrt{\frac{4}{3}}$ is in excellent agreement with the theoretical expectation for a quartet spin system (Mizuochi et al., 2002). In a next step, I proceed to measuring spin coherence times between the ground state levels $|-\frac{1}{2}\rangle_{gs}$ and $|-\frac{3}{2}\rangle_{gs}$. To this end, I perform a free induction decay (FID) measurement in which I replace the Rabi pulse in Fig. 4.8 (a) by two $\frac{\pi}{2}$-pulses separated by a waiting time τ_{FID}. The experimental data in Fig. 4.8 (b) show a dephasing time of $T_2^* = 30 \pm 2\mu s$, which is comparable with state-of-the-art results reported for

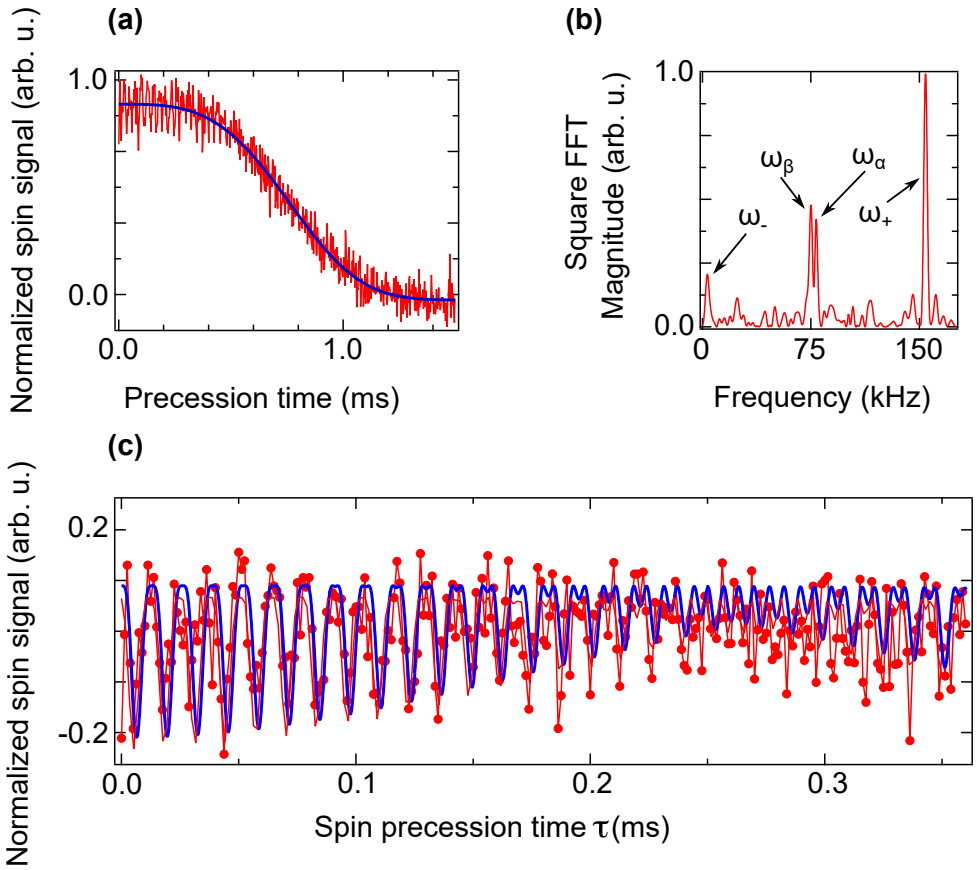

FIGURE 4.9: (a) Hahn echo measurement and nuclear spin coupling, resulting in infer $T_2 = 0.85 \pm 0.12$ ms. Red lines are data and the blue line is a fit using a higher-order exponential function. (c) is a zoom into the first part of the Hahn echo after subtraction of the exponential decay function and normalization. Pronounced oscillations are observed, witnessing coherent coupling to a nearby nuclear spin. Data (red dots connected by lines) are fitted using equation 4.8 (blue line). (c) is a Fourier analysis of the normalized Hahn echo, showing four distinct frequency components through which a weakly coupled ^{29}Si nuclear spin is identified.

NV centres in isotopically ultrapure diamonds (Balasubramanian, 2009). To measure the spin coherence time T_2, I use a Hahn-echo sequence by adding a refocusing π-pulse in the middle of two $\frac{\pi}{2}$-pulses. As shown in Fig. 4.9 (a), I measure a spin coherence time of $T_2 = 0.85 \pm 0.12$ ms. For an isotopically purified system, like the one used in the present experiment I expect somewhat longer dephasing times. As outlined in Section 4.5.1, I attribute the origin to be nearby defect clusters created by microscopic cracks induced by the CVD wafer cutting process using a dicing saw. Hence, optimized sample growth, cutting and annealing should increase dephasing times to several tens of milliseconds (Simin et al., 2017). Quite interestingly, the initial part of the spin echo decay of this particular defect shows pronounced oscillations resulting from the hyperfine coupling of the electron spin to nuclear spins. Being initially polarized along the z-axis in the Bloch sphere, and with microwave pulses polarized along the x-axis, the echo sequence measures (Rowan,

Hahn, and Mims, 1965)

$$-<S_y>=1-\frac{1}{k}[2-2cos(w_a\tau)-2cos(w_\beta\tau)+cos(w_-\tau)+cos(w_+\tau)] \tag{4.8}$$

Here, k is the modulation depth parameter $k=(\frac{2w_aw_\beta}{a_\perp w_I})^2$, with w_I being the nuclear Larmor frequency, and $w_{a,\beta}=[(w_I+m_{a,\beta}A_\parallel)^2+(m_{a,\beta}A_\perp)^2]^{1/2}$. Here, $m_a=-3/2$ and $m_\beta=-1/2$ are the spin projections of the involved ground states with respect to the z-axis. Further, $w_\pm=w_a\pm w_\beta$, and $A_{\perp,\parallel}$ are the orthogonal and parallel hyperfine components, respectively. Essentially, $<S_y>$ is modulated because of quantum beats between hyperfine levels, which not only show the nuclear frequencies $w_{a,\beta}$ but also their sum and difference frequencies $w_\pm$. The Fourier transformation reveals strong frequency components at $w_a/2\pi=77.9\pm0.1$ kHz and $w_\beta/2\pi=76.0\pm0.1$ kHz. As w_+ is quite close to twice the Larmor frequency of a ^{29}Si nuclear spin ($w_I/2\pi\approx77.9$ kHz), I conclude that the parallel hyperfine coupling $A_\parallel$ is weak compared to the Larmor frequency. In addition, from the inferred modulation depth parameter ($k=0.15\pm0.02$), I infer that there is a sizable difference between $A_\perp$ and $A_\parallel$. Indeed, from the fit to the data, I infer a purely dipolar coupling with strengths of $A_\perp\approx29$ kHz and $A_\parallel\approx10$ kHz, respectively. This allows inferring the relative position of the nuclear spin, using $A_\parallel=\frac{\eta_{si}}{r^3}(3cos^3\theta-1)$ and $A_\parallel=\frac{\eta_{si}}{r^3}(3sin\theta cos\theta)$, in which $\eta_{Si}=15.72$ MHz $\AA^3$ is the dipole-dipole interaction coefficient (Carter et al., 2015), r is the distance between electron and nuclear spin, and θ is the c-axis and r. I obtain $r\approx11.6$ $\AA$ and $\theta\approx61°$.

4.5.1 Decoherence Sources

In chapter 4.5, I report a spin decoherence time of $T_2=0.85\pm0.12$ ms, measured by Hahn echo. Although this result is better than the previously reported values (Nagy et al., 2018b; Wallace et al., 2015; Widmann and Lee, 2015; Carter et al., 2015), one may anticipate reduced decoherence rates owing to the use of an isotopically purified nuclear spin free 4H-SiC sample, in analogy to previous experiments with isotopically purified diamond and silicon (Balasubramanian, 2009; Tyryshkin et al., 2012). As I used a rather low dose of electron beam irradiation to create defect centres, the concentration of paramagnetic defects is small ($\sim10^{13}cm^{-3}$) as explained in Section A, which cannot explain the observed T_2 times. Shallow nitrogen donors are also discarded as a major decoherence source as their concentration is also too low to be significant ($\sim3.5\cdot10^{13}cm^{-3}$) since the equivalent spin dipole-dipole interaction in electronic spin bath requires higher total impurity concentration ($\sim6\cdot10^{14}cm^{-3}$) (Widmann and Lee, 2015). I therefore attribute the main decoherence source to be undesired defects near surface paramagnetic defects created by cutting with a typical concentration in the low ($10^{13}cm^{-2}$) range in the region about $\sim1\mu m$ from the surface (Zvanut, Thomas, and Dashdorj, 2010). Before irradiation, samples were annealed to 1130 $°C$ in N_2 gas flow to reduce the concentration of paramagnetic surface defects to below detection of Electron Paramagnetic Resonance (EPR) (below $(10^{12}cm^{-2})$). Since the N_2 annealing is known to reduce only 10% of the surface defects and the EPR experimental conditions are not optimized for the detection of the surface defects, it is safe to assume

that the surface defect concentration within ~ $1\mu m$ range from the surface has an upper limit of ($10^{16} cm^{-3}$). As the optical transition dipole of the investigated defect centres is parallel to the crystal's c-axis, I had to flip the sample by 90°. This comes with the trade-off that all observed defects are located close to the cutting surface. The cutting surfaces are also expected to have structural defects induced by micro cracks caused by cutting. In the future, this issue can be addressed by improved sample processing (Zvanut, Thomas, and Dashdorj, 2010) or by growing SiC layers on a-plane substrate so that solid immersion lens can be fabricated on as-grown surfaces, which contain no such defects.

4.6 Pump Probe Excitation

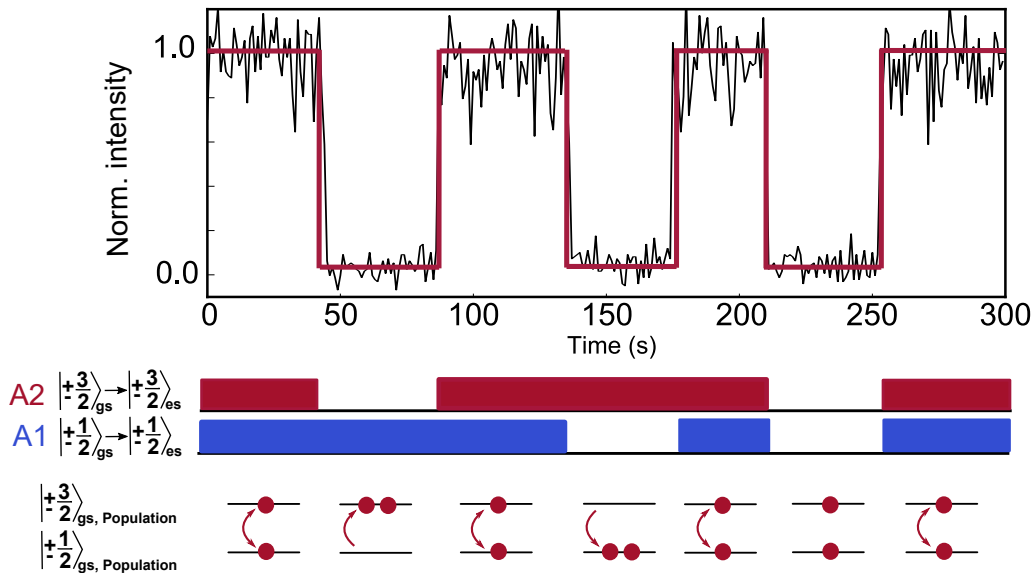

FIGURE 4.10: Pump probe experiment with two resonant lasers parked at A1 and A2. The spin population of the silicon vacancy ground state is pumped into the $|\pm 3/2\rangle$ or $|\pm 1/2\rangle$ subspaces, depending on the used excitation laser.

I performed a pump probe experiment to analyze the spin population dynamics during optical excitation. The initial condition is that all ground state spins $S = \pm 3/2$ and $S = \pm 1/2$ are nearly equally populated after excitation with an 730 nm laser. Both optical transitions A1 and A1 are spin conserving transition and a spin-flip can only occur with intersystem crossing (ISC) through the metastable state. The pump probe experiment is conducted in a way that one resonant laser is parked at A1 and a second at A2. The level structure can be seen in Fig. 4.3 (b). Fig. 4.10 shows the intensity of the emitted photons depending which optical transition is driven. The first scenario in which both transitions A1 and A2 are contentiously driven can be seen between 0 and 45 s. The population is continuously swapped between $|\pm 3/2\rangle \leftrightarrow |\pm 1/2\rangle$ through the metastable state and no dark state is reached. Between 45 and 90 s only the resonant laser at A1 turned on, such that the population is driven from the spin subspace $|\pm 1/2\rangle \leftrightarrow |\pm 3/2\rangle$ through the metastable state. This spin polarization process ends into a dark state as it can be seen in

Fig. 4.10. The system behaves similarly if only the optical transition A2 is driven, as it can be seen between 135 and 180 s. This experiment reveals that photoluminescence excitation (PLE) requires using MW to continuously mix the groundstate population. Secondly it also shows that this mechanism can be used to polarize the groundstate spin manifold as it can be seen in section 4.7.

4.7 Ground State Spin Initialization Fidelity

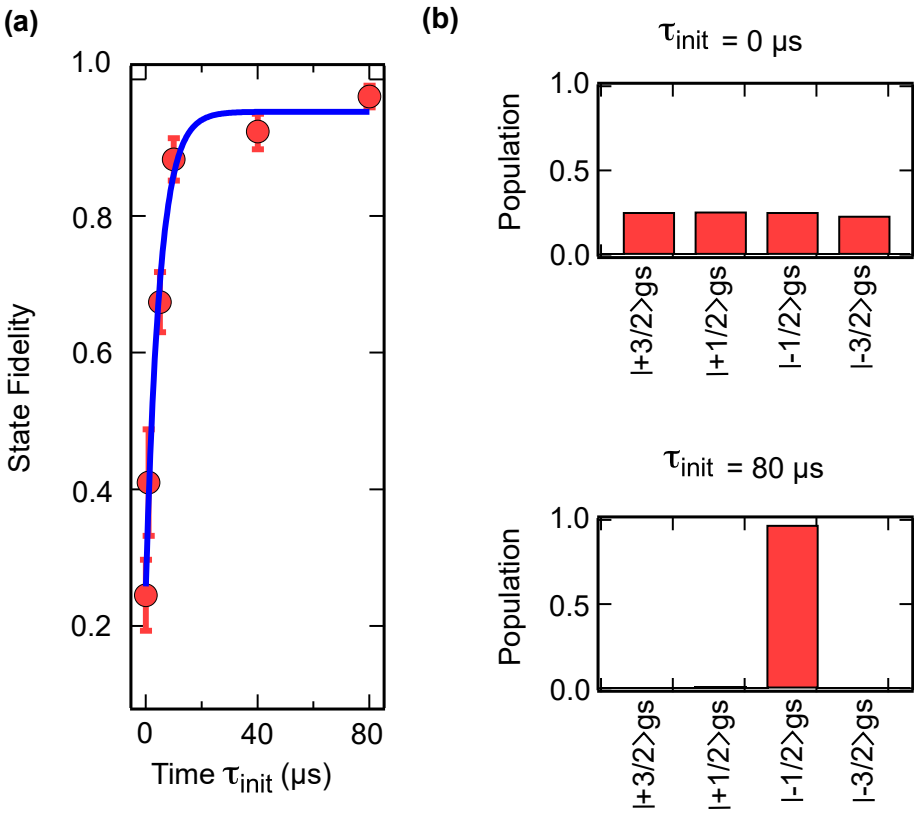

FIGURE 4.11: Electron spin initialization fidelity. Before each round, the ground state spin is depolarized using off-resonant excitation for 40 μs. Then, the system is initialized into $|-1/2\rangle_{gs}$. Ground state populations are inferred from Rabi oscillations and resonant optical readout. (a) spin population in $|-1/2\rangle_{gs}$ as a function of the duration of the initialization procedure. Up to 97.5 % are achieved. The blue line is a fit using an exponential function. (b) inferred spin populations in the four ground state sublevels without initialization and after 80 μs initialization time.

Besides excellent coherence times, a crucial requirement for quantum information applications is high-fidelity quantum state initialization (DiVincenzo, 2000a). To optimize the spin state initialization procedure, I vary the time interval τ_{init} of the initializing laser (A_2) and microwave fields (MW3) and extract the populations in the four ground states via the contrast of Rabi oscillation measurements. I first equilibrate all four ground state populations to within < 1% with a 40μs long off-resonant laser pulse (Nagy et al., 2018b).

Then, I apply the selective spin state initialization procedure for a time τ_{init}, followed by different Rabi sequences, and eventual state readout along the A2 optical transition. Fig. 4.11) (a and b) shows the development of the extracted ground state populations for τ_{init} ranging from 0 to 80 μs. I achieve initialization fidelities up to 97.5 ± 2.0 %, which is comparable to previous demonstrations with color centres in diamond or SiC (Robledo et al., 2011; Christle et al., 2015).

4.7.1 Initialization Fidelity Model

To determine the population in each ground state spin level, I perform Rabi oscillations for the three allowed transitions, linking the levels $|-1/2\rangle_{gs} \leftrightarrow |-3/2\rangle_{gs}$ (MW1),$|-1/2\rangle_{gs} \leftrightarrow |+1/2\rangle_{gs}$ (MW2), and $|+1/2\rangle_{gs} \leftrightarrow |+3/2\rangle_{gs}$ (MW3). Then, I read out the spin population in $|\pm 3/2\rangle_{gs}$ by resonant excitation along the A2 transition for 150 ns. Within such a short readout time, I can safely assume that the obtained fluorescence signal is proportional to the population in $|\pm 3/2\rangle_{gs}$ (as ISC through MS takes several 100 ns). Note that in order to obtain a signal from Rabi oscillations $|-1/2\rangle_{gs} \leftrightarrow |+1/2\rangle_{gs}$, an additional population swap (π-pulse at MW3) between $|-1/2\rangle_{gs}$ and $|-3/2\rangle_{gs}$ is applied before state readout. I denote now the populations in all four ground states by p_i where $i = \{-3/2, -1/2, +1/2, +3/2\}$ stands for the spin quantum number of each state. I then measure the fringe visibility of the obtained Rabi oscillation signal in order to infer ground state spin populations. The fringe visibility for Rabi oscillations between sublevels $|i\rangle_{gs}$ and $|j\rangle_{gs}$ with $i, j = \{-3/2, -1/2, +1/2, +3/2\}$ and $|i - j| = 1$ is defined as,

$$v_{i,j} = \frac{I_{max} - I_{min}}{I_{max} + I_{min}} \tag{4.9}$$

where $I_{max}(I_{min})$ denotes the maximum (minimum) signal during the Rabi oscillation. Considering that our state readout is only sensitive to spin population in $|\pm 3/2\rangle_{gs}$, the three conducted Rabi oscillation experiments lead to the following fringe visibilities:

$$v_{3/2,1/2} = \frac{p_{1/2} - p_{3/2}}{2p_{-3/2} + p_{1/2} + p_{3/2}} \tag{4.10}$$

$$v_{1/2,-1/2} = \frac{p_{-1/2} - p_{1/2}}{2p_{-3/2} + p_{-1/2} + p_{1/2}} \tag{4.11}$$

$$v_{-1/2,-3/2} = \frac{p_{-1/2} - p_{3/2}}{2p_{3/2} + p_{-3/2} + p_{-1/2}} \tag{4.12}$$

In addition, the total population of all the ground states must sum up to unity, i.e

$$p_{-3/2} + p_{-1/2} + p_{+1/2} + p_{+3/2} = 1 \tag{4.13}$$

As all observed Rabi oscillations start with a local minimum in fluorescence intensity, I can further assume that after initialization, the ground state populations fulfill:

$$p_{-3/2} \sim p_{-3/2} < p_{+1/2} < p_{-1/2} \tag{4.14}$$

Solving the system of four equations under these constraints allows me to extract all four values of p_i, which is shown for the initialization times 0 and 80 μs in Fig. 4.11 (a).

4.8 Electronic Fine Structure and Spin Polarization of the Silicon Vacancy Centre

The electron fine structure calculation was done in a collaboration with Dr. Oney Soykal. A simplified electronic fine structure model of the V_1 defect is shown in Fig. 4.12. The spin $m_s = \pm 1/2$ and $m_s = \pm 3/2$ states of the first excited state (es) are labeled as es_1 and es_2, respectively. Similarly, the spin states $m_s = \pm 1/2$ and $m_s = \pm 3/2$ belonging to the ground state (gs) are denoted by gs_1 and gs_2. The optically active transitions $es_1 \rightarrow gs_1$ (red transition) and $es_2 \rightarrow gs_2$ (blue transition) have equal radiative decay rates as the states involved in these transitions have the same molecular orbital configurations result-

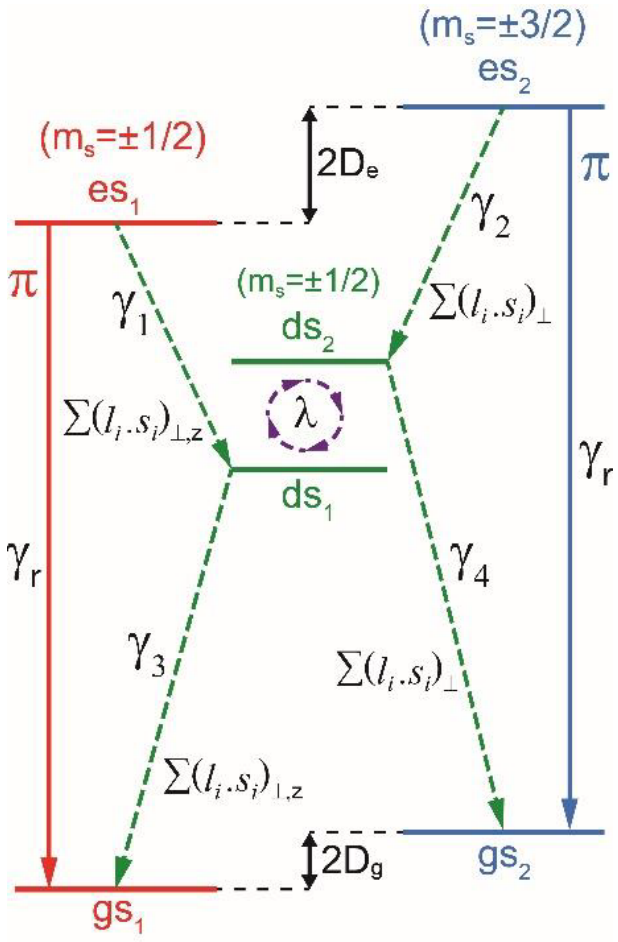

FIGURE 4.12: Electronic fine structure of the V_1 defect in 4H-SiC. The model describes the rates between the ground and excited states by γ_r. The rates between the excited state and the metastable state are described by $\gamma_{1,2}$. The rates from the metastable to the ground states are described by $\gamma_{3,4}$. The mixing in between the metastable state doublets is considered by the parameter λ.

ing with equal transition dipole moments. Moreover, the spin polarisation of the V_1 defect is governed by the phonon-assisted non-radiative in-tersystem crossing (ISC) from and to the metastable doublet states, ds_1 and ds_2, via direct spin-orbit coupling (DSO). The four non-radiative ISC decay rates shown in Fig. 4.12 determine the unique features in the PLE spectra of this defect. The non-radiative decay rates in the entry channel that are associated with the decay from es_1 to ds_1 and from es_2 to ds_2 are labeled as γ_1 and γ_2, respectively, and they determine the amplitudes of the A1 and A2 peaks shown in Fig. 4.4 (a). Similarly, the decay rates originating from ds_1 back to gs_1 and from ds_2 back to gs_2 are labeled as γ_3 and γ_4, respectively, and they are responsible for the shelving lifetime of this defect. We obtain the relationships between γ_1 and γ_2, as well as γ_3 and γ_4, by evaluating the corresponding DSO matrix elements,

$$\gamma_i = \frac{2\pi}{\hbar} |\langle \Psi_i^{gs} | \sum_j L_j s_j | \Psi_i^{ds} \rangle|^2 \tag{4.15}$$

in the symmetry adapted $\Psi_i^{ds/gs}$ wave-functions basis of j = 5 active electrons (Soykal, Dev, and Economou, 2016). We find that 2 metastable doublet states (with symmetries A_1 and ^2E) have non-zero DSO matrix elements that can participate in the ISC. The E-symmetry ds (e^3) can couple to both es and gs by the orthogonal component of the DSO $l_\perp s_\perp$ (with respect to the c-axis). The remaining A1 ds (ve^2) is strongly hybridized with the E ds (e^3) by the $l_\parallel s_\parallel$ component of the DSO. As a result, the overall ISC can be simplified into two doubly degenerate metastable states, labeled as ds_1 and ds_2, which can only couple to the spin $\pm 1/2$ or the $\pm 3/2$ states of the es and gs, respectively. The PLE spectra of the V_1 defect can be accurately reproduced by using the theoretical fine structure of Fig. 4.12. The PLE signal of the V_1 defect corresponds to the sum of the steady state es_1 and es_2 excited state populations of es_1 and es_2, that are calculated using the following master equation,

$$\frac{d\rho}{dt} = -\frac{i}{\hbar}[H_0, \rho] + \gamma_r \sum_{i=0}^{2} L(A_r^i) + \sum_{i=0}^{4} \gamma_i L(A_{ds}^i) + \gamma_R \sum_{i=0}^{2} L(A_R) + \gamma_s L(A_s) \tag{4.16}$$

The decay and decoherence processes of the defect are represented by the Lindblad super-operators, i.e. $L(0) = 0\rho 0^+ - \{0^+0, \rho\}/2$ for any operator 0. The electronic fine structure Hamiltonian is given by,

$$\begin{aligned} H_0 = \frac{(D_{gs} - D_{es} - \delta_L)}{2}(|gs_1\rangle\langle gs_1| - |es_1\rangle\langle es_1|) - \frac{(D_{gs} - D_{es} - \delta_L)}{2} \\ (|gs_2\rangle\langle gs_2| - |es_2\rangle\langle es_2|) + \lambda(|ds_1\rangle\langle ds_2| - |ds_2\rangle\langle ds_1|) + \\ \Omega_L(|gs_1\rangle\langle es_1| - |gs_2\rangle\langle es_1| + c.c.) \end{aligned}$$

in the rotating frame of the excitation laser with Rabi frequency Ω_L and detuning $\delta_L = w_L - w_{ZPL}$ from the zero phonon line (ZPL). The excited and ground state's ZFS are given by $2D_{es}$ (975 MHz) and $2D_{gs}$ (9 MHz), respectively. The radiative decays, $A_4^i = |gs_i\rangle\langle es_i|$, have same radiative decay rate γ_4. The ISC from es to the metastable ds are given by $A_{ds}^1 = \langle ds_1||es_1\rangle$ and $A_{ds}^2 = \langle ds_2||es_2\rangle$ with rates γ_1 and γ_2, whereas the ISC from ds back

to gs are denoted by $A^3_{ds} = \langle gs_1||ds_1\rangle$ and $A^4_{ds} = \langle ds_2||es_2\rangle$ with ratesγ_3 and γ_4, respectively. The intrinsic spin relaxation in the ground state and dephasing among ds are considered by $A_R = |gs_1\rangle\langle gs_2| + |gs_2\rangle\langle gs_1|$ with rate γ_R and $A_s = |ds_1\rangle\langle ds_1| - |ds_2\rangle\langle ds_2|$ with rate γ_s. Spin-mixing among ds via fast relaxation processes is also included in H_0 by the λ term. Resonant optical excitation along the A2 transition ($gs_2 \rightarrow es_2$) will lead to an optical pumping into the gs_1. Therefore, to observe a measurable signal during PLE, the ground state spin must be able to relax. Alternatively, one can use MW pulses on the gs spin states for coherent control as well as to overcome this optical pumping. During a continuous broadband MW pulse where all three gs spin transitions shown in Fig. 4.7 (a) are allowed to relax equally, the PLE amplitude mismatch between A1 and A2 is directly determined by the ISC rates of γ_1 and γ_2. We find that the faster γ_1 rate causes more population to be removed non-radiatively from $|\pm 1/2\rangle_{es}$ per optical cycle compared to $|\pm 3/2\rangle_{es}$, therefore leading to a smaller amplitude for A1 than A2.

CHAPTER 5

Indistinguishable Absorption Properties of Silicon Vacancy Centre

5.1 Indistinguishability of Single Silicon Vacancy Centres

Many quantum information experiments are based on optical interference between emission of multiple single emitters, requiring that their photon emission is indistinguishable and spectrally stable. The V_{Si} centre in 4H-SiC is a solid state quantum defect with outstanding spectral stability (see Chapter 4.3.1). The spectral stability mainly originates from the identical symmetry in the ground and first excited state (called V1). This results in ground and excited state electronic wavefunctions for which, the dipole moments are nearly identical (see Chapter 4.3.1). Since the dipole moment of the ground and excited state are not perfectly identical, their relative change in energy dependence on the electric field and difference of the dipole moments. This effect is known as spectral diffusion (Neu et al., 2013).However, the difference between the dipole moments of ground and excited state is expected to be two orderes of magnitude less than for the NV-centre in diamond, such that one would expect that spectral diffusion is strongly suppressed for V_{Si} centre in 4H-SiC. Fig 4.4 (d) shows five V_{Si} centres for which the absorption lines (energy between ground and excited state) are energetically nearly identical. This measurement supports the calculations of almost identical dipole moments and spectral diffusion in Chapter 4.3.1.

Fig 4.4 (d) shows however that the absorption lines are not perfectly indistinguishable for multiple V_{Si} centres in 4H-SiC. This phenomenon is observed for almost all single emitters in the solid state, and quite natural considering that the local environment of each defect is different. For NV centres in diamond, it has however been demonstrated already that initially distinguishable emitters can be made indistinguishable by means of Stark shift tuning. Unfortunately I showed in Chapter 4.3.1 that the V_{Si} centre absorption lines can not be shifted by an electric field of ± 200 kV/m to overlap spectrally with a second V_{Si} centre.

For this reason, I will perform in this Chapter an analysis of ≈ 50 V_{Si} centres in 4H-SiC to

measure the natural distribution of the optical absorption lines. This analysis will show how many by chance V_{Si} centres one may need to analyze until one will find two indistinguishable V_{Si} centres. The statistical value will give a hint about the realistic scalability potential of V_{Si} centres in 4H-SiC in the perspective of large-scale quantum information processing applications with V_{Si} centres in 4H-SiC.

5.1.1 Sample Preparation

To analyze the indistinguishability of single V_{Si} centres I used a $4H-^{28}Si^{12}C$ silicon carbide layer grown by chemical vapour deposition (CVD) on a n-type (0001) 4H-SiC substrate. The isotope purity was measured with SIMS to be $4H-^{28}Si > 99.85\%$ and $^{12}C > 99.98\%$. To assure the same conditions of the Fermi level and impurities the same sample parameters where chosen as in Chapter 4. More details are given in Table 2.2. The sample was flipped to the side to excite the first exited state V_1. The light extraction efficiency was improved by fabricating solid immersion lenses using a focused ion beam milling machine (Helios NanoLab 650). To increase the density of single V_{Si} centres by a factor of 10 as compared to Chapter 4, the electron irradiation dose was increased from $1 \cdot 10^{12} cm^{-2}$ to $1 \cdot 10^{13} cm^{-2}$. The energy of the electron irradiation was 2 MeV. At the end, the sample was cleaned for two hours in peroxymonosulfuric acid to remove surface contaminations (Widmann and Lee, 2015).

5.1.2 Optical Absorption Properties of Single Silicon Vacancy Centre

To analyze optical absorption properties of V_{Si} centres in 4H-SiC, a confocal scan with a off-resonant laser (730 nm) is necessary. Fig. 5.1 (a) shows the result of a confocal scan where the red dots indicate single V_{Si} centres in 4H-SiC. The difference in intensity comes from different focal planes of the localized V_{Si} centres. A PLE measurement is shown in Fig. 5.1 (b) of a single V_{Si} centre to reveal the optical absorption lines. The resonant laser intensity during the measurement was 1 W/cm^2. The first peak shows the A1, and the second peak the A2 optical spin conserving transition of a V_{Si} centre. The measured linewidth of both transitions A1 and A2 is $\approx$ 168 MHz. In a second step, I perform a confocal scan using resonant laser excitation. The resonant excitation laser is parked at the A2 optical transition of the above investigated V_{Si} centre. This measurement can be seen in Fig. 5.1 (c). The bright spots indicate single V_{Si} centres with the same energy in absorption (either A1 or A2). This result shows that one can indeed find single V_{Si} centres with indistinguishable PLE frequencies. A more detailed analysis is needed to understand the spectral overlapping effect between single V_{Si} centre absorption lines. Only a perfect overlap within the Fourier transform limited linewidth (FTL), which is $\approx$ 30 MHz for a V_{Si} centre, would result in indistinguishable photon emission. Fig. 5.1 (d) shows the level structure of a V_{Si} centre with the A1 and A2 optical spin conserving transitions respectively.

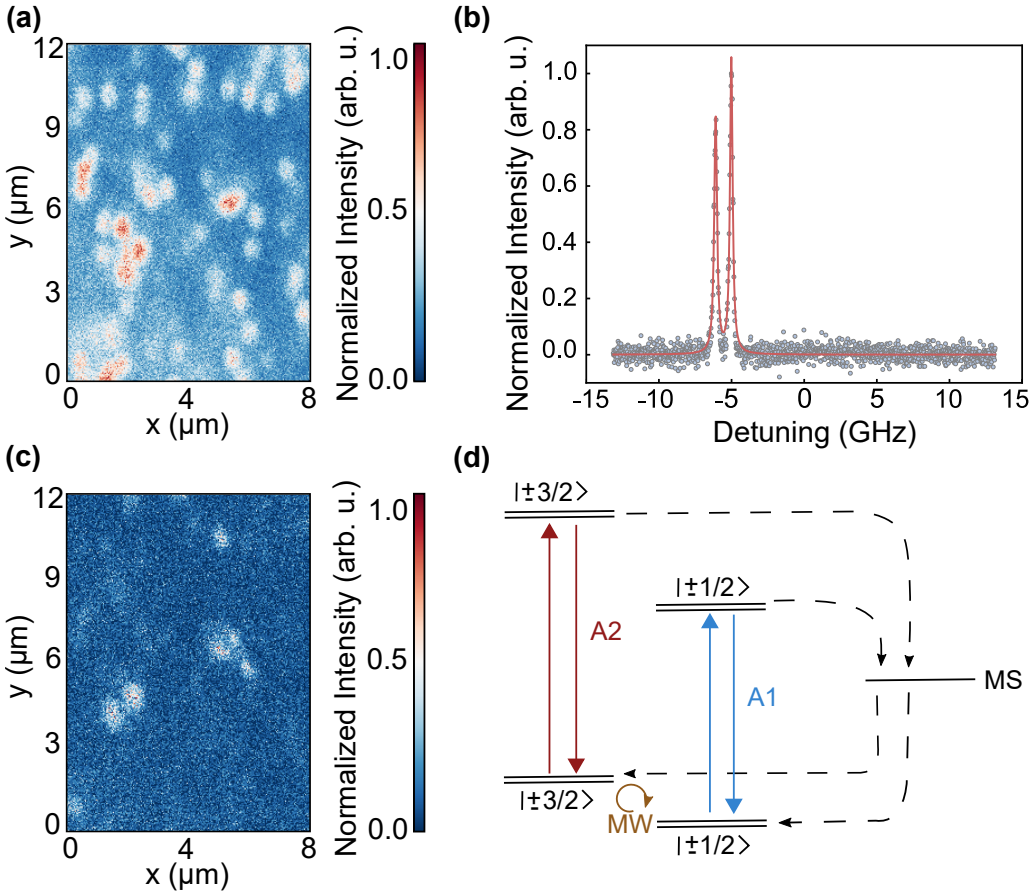

FIGURE 5.1: Indistinguishability properties of V_{Si} centre in 4H-SiC. (a) Confocal scan with a off-resonant 730 nm laser. The red dots indicate single V_{Si} centre. (b) PLE scan of single V_{Si} centre from the confocal scan in (a). (c) The resonant laser is now parked at the A2 transition as inferred in (b) and a confocal scan is performed. The bright spots indicate single V_{Si} centre with the same absorption energy. (d) Level scheme of silicon vacancy centres in 4H-SiC.

5.1.3 Dependence of Electron Irradiation on the Optical Linewidth

In Chapter 4, I report 60 MHz linewidth of single V_{Si} centre resonant optical transition. Although this is close to the FTL linewidth (≈ 30 MHz), I still observe inhomogeneous broadening (see Fig. 5.1). I suspect the origin of the broadening is due to the local electric field fluctuations originating from free carriers injected by ionized defects in proximity. The PLE measurement in 5.1 (b) shows a linewidth of ≈ 168 MHz which is almost three times the reported linewidth as in Chapter 4. Although the change in dipole moments by optical pumping is minimal, since it still can be coupled to the fluctuating electric fields, residual broadening takes place. As discussed in Chapter 2, various defects exist in the tested samples which are created during the sample growth and post-process or by electron irradiation, such as shallow N impurities, and carbon vacancies. I show in Fig. 5.2 (a) representing absorption spectrum of the single V_{Si} centre in the high-dose electron irradiated sample ($1 \cdot 10^{13}$ cm^{-2}). Under 1 W/cm^2 optical pumping intensity, I find an average linewidth of 167 ± 9 MHz from ≈ 50 tested defects. Since the only different parameter

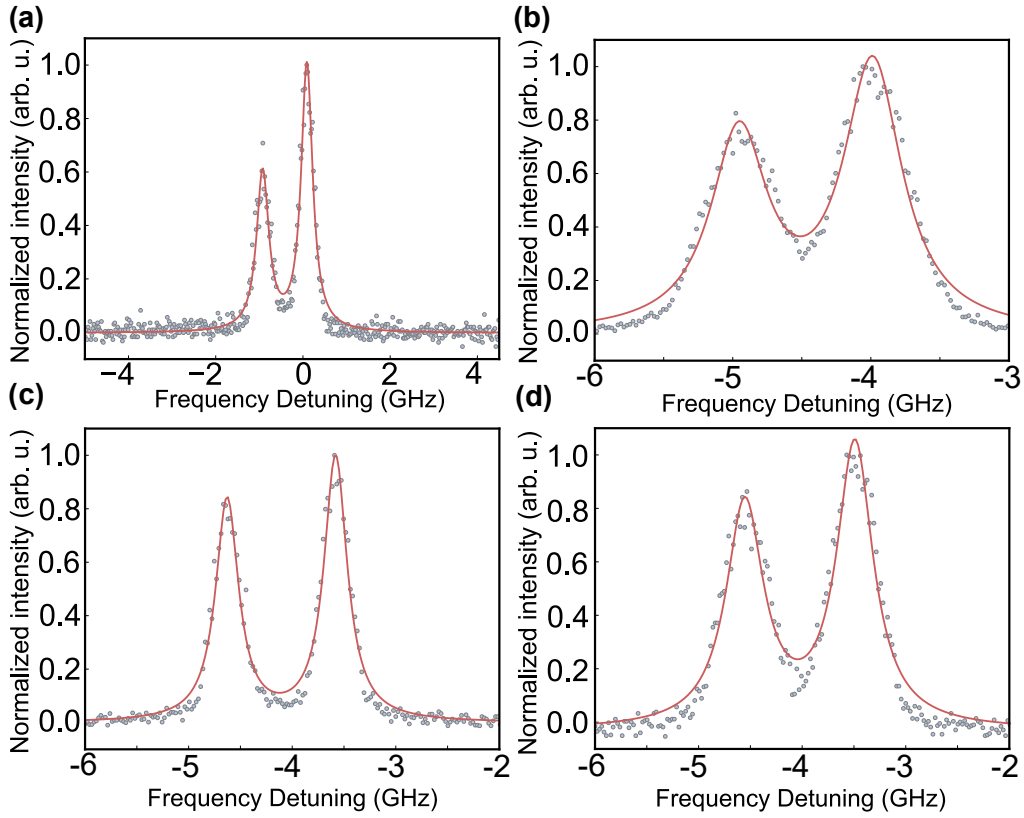

FIGURE 5.2: PLE measurements of various single V_{Si} centres (a,b,c,d) at a electron irradiation dose of $1 \cdot 10^{13} cm^{-2}$. The measured HWHM average linewidth is 167 ± 9 MHz, roughly three times higher that at the low electron irradiation value of $1 \cdot 10^{12} cm^{-2}$.

between the sample in Chapter 4 and 5 is the electron irradiation dose, which differs by one order of magnitude ($1 \cdot 10^{12}$ cm^{-2} and $1 \cdot 10^{13}$ cm^{-2}), I attribute this broadening to the increased density of free carriers originating from dense defect clusters surrounding the tested silicon vacancies in the high-dose irradiated sample. This result shows that the high purity silicon carbide crystal is essential for achieving lifetime-limited linewidth of optical transition.

5.1.4 Statistics on the Inhomogeneous Distribution of the Resonant Absorption Lines

In this section, I want to analyze the effect of strain in the 4H-SiC crystal on absorption lines of the V_{Si} centre. The measured V_{Si} centre were distributed in an area of 8 $\mu m \cdot$ 12 μm (see Fig. 5.1 (a)). The resonant laser power was fixed to 1 W/cm^2 and the MW power to 0 dBm during all measurements. I performed PLE measurements to analyze the strain effect on V_{Si} centre. The results of the PLE experiments (see Fig. 5.2 for four different V_{Si} centres) where fitted with an Lorentzian fit (Wertheim et al., 1974). The linewidth and centre position of the optical transition A1 and A2 were extracted from the Lorentzian fit. The reference value of the scanning laser during the PLE measurements was kept at $f_{detuning}$ = 347.94059 THz (0 V at the piezo of the laser cavity). The laser frequency was

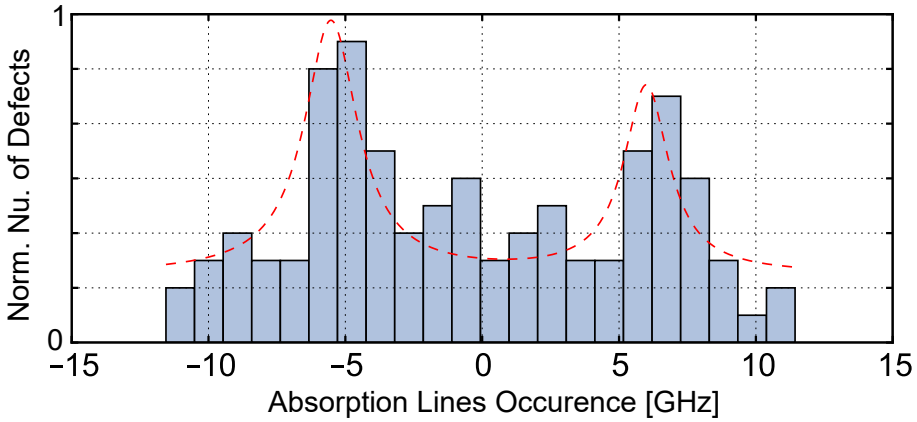

FIGURE 5.3: Number of V_{Si} centres per 200 MHz bin. The central frequency of the optical A1 and A2 transition of 50 defects is shown. The central frequency is f = 347.94059 THz. The histogram shows clustering of V_{Si} centres at - 5 and + 6 GHz.

continuously tracked with a wavemeter from HighFinesse Angstrom WS7/30. The result of the measurement is illustrated as histogram in Fig. 5.3. The bin width of the histogram is ≈ 1 GHz. The x-axis of the histogram is the laser detuning and the y-axis represents the normalized number of V_{Si} centres. The total number of measured V_{Si} defects is 50. The centre frequency of the optical transition A1 and A2 of all V_{Si} centre is plotted on the x-axis. The y-axis counts the number of V_{Si} centre at one bin width (no absolute numbers are shown because one V_{Si} centre can be in two bins due to 1 GHz separation between A1 and A2). The result of the histogram shows a broad distribution (≈ 20 GHz) of the V_{Si} centres optical absorption lines. The distribution shows that 28 % of all V_{Si} centres are distributed between -6 and -3 GHz and 22 % between +5 GHz and +8 GHz. This indicates that roughly 50 % of all V_{Si} centres are distributed between two laser detuning ranges. The resonant confocal scan in Fig. 5.1 (c) shows a spatial clustering of V_{Si} centres with identical optical absorption energies. This might give a hint that the V_{Si} centre feels a similar local strain, depending on the position in the 4H-SiC crystal. Due to the higher dipole moment the excited state is more sensitive to strain (see Section 4.3.1). Strain coupling parallel to the c-axis shifts all energies of the ground and excited state nearly equally. The main contribution of the strain coupling comes from a parallel electric field inside the crystal, called crystal field (Soykal and Reinecke, 2017), see Section 4.3.1. The crystal field in 4H-SiC points always in the direction of the c-axis. This indicates that strain at the position of the V_{Si} centre in the 4H-SiC crystal needs to be at least on the same order of magnitude as the crystal field to achieve an effect. The absolute value of the crystal field at a V_{Si} centre is still under debate. Measurements of the crystal field have been done within previous studies (Castelletto et al., 2014; Lohrmann et al., 2015). This results may indicate why the V_{Si} centre in 4H-SiC feels a low electric field sensitivity.

A more important question is how likely it is that two V_{Si} centres show emission lines that overlap within the FTL. I extracted the linewidth and centre frequency of all measured PLE measurements and correlated the spectral overlap properties. Fig. 5.4 shows the result of

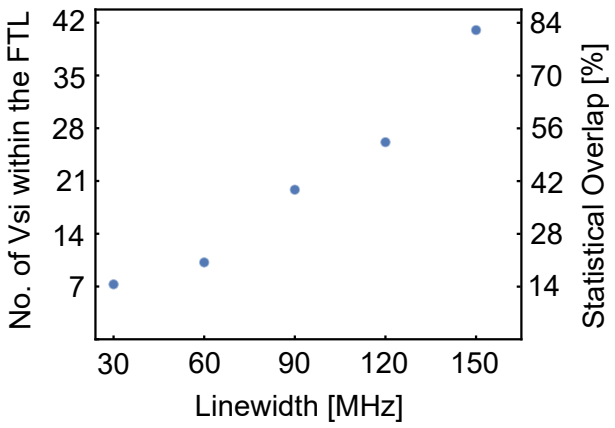

FIGURE 5.4: Spectral overlap of V_{Si} centres within the FTL. The statistics shows that 7 out of 50 V_{Si} centres exhibit indistinguishable absorption lines. If the linewidth is increased, also the number of defects that spectrally overlap is increased.

the measurement. The Fig. 5.4 shows that 7 out of 50 measured V_{Si} centres do perfectly spectral overlap withing the FTL linewidth. If the FTL linewidth is increased also the number of defects who that spectrally overlap is increased. The result of this graph shows that V_{Si} centres in 4H-SiC provide a reasonably high probability to show overlapping emission lines. The silicon vacancy centre in diamond shows similar statistics where some of the defects do overlap within the FTL linewidth (Rogers et al., 2014b). The origin of the statistics in diamond is inversion symmetry. If the inversion symmetry is slightly disturbed, which may occur in nano-structures, the properties can strongly change. In the scenario of the V_{Si} centre in 4H-SiC, the statistics is governed by similar dipole moments in ground and excited state (due to same wavefunction symmetry) and a strong crystal field which shields the defects against electric field fluctuations and strain. These properties make the V_{Si} centre in 4H-SiC an interesting system for quantum technologies.

5.1.5 Influence of Strain on the Exited State Zero Field Splitting

The strain Hamiltonian (Soykal and Reinecke, 2017) for the V_{Si} centre can be seen here

$$H_\sigma = \begin{bmatrix} D+\xi_1^r\Lambda^r & \xi_3\Lambda_{xy} & i\xi_3\Lambda_{xy}^\star & 0 \\ \xi_3^\star\Lambda_{xy}^\star & -D+\xi_2^r\Lambda^r & 0 & -i\xi_3\Lambda_{xy}^\star \\ -i\xi_3\Lambda_{xy}^\star & 0 & -D+\xi_2^r\Lambda^r & -i\xi_3\Lambda_{xy}^\star \\ 0 & -\xi_3\Lambda_{xy} & i\xi_3\Lambda_{xy}^\star & D+\xi_1^r\Lambda^r \end{bmatrix}. \tag{5.1}$$

The off diagonal term is $\Lambda_{xy} = \sigma_{xx}^E - \sigma_{yy}^E + 2i\sigma_{xy}^E$, σ the strain coefficient, D the zero field term, r the sum over the allowed molecular orbitals A1 and E, ξ the strain coupling coefficient (Soykal and Reinecke, 2017). The calculated strain sensitivity with a deformation potential of 11.6 eV (Iwata and Itoh, 2001) for bulk 4H-SiC is $\approx 6.7 \cdot 10^{-8}$ strain $\mathrm{Hz}^{-1/2}$ (Soykal and Reinecke, 2017) in the ground state. The strain in the crystal affects the absolute energy of the ground and excited spin state manifolds (see Section 4.3.1 and 5.1.4). Due to

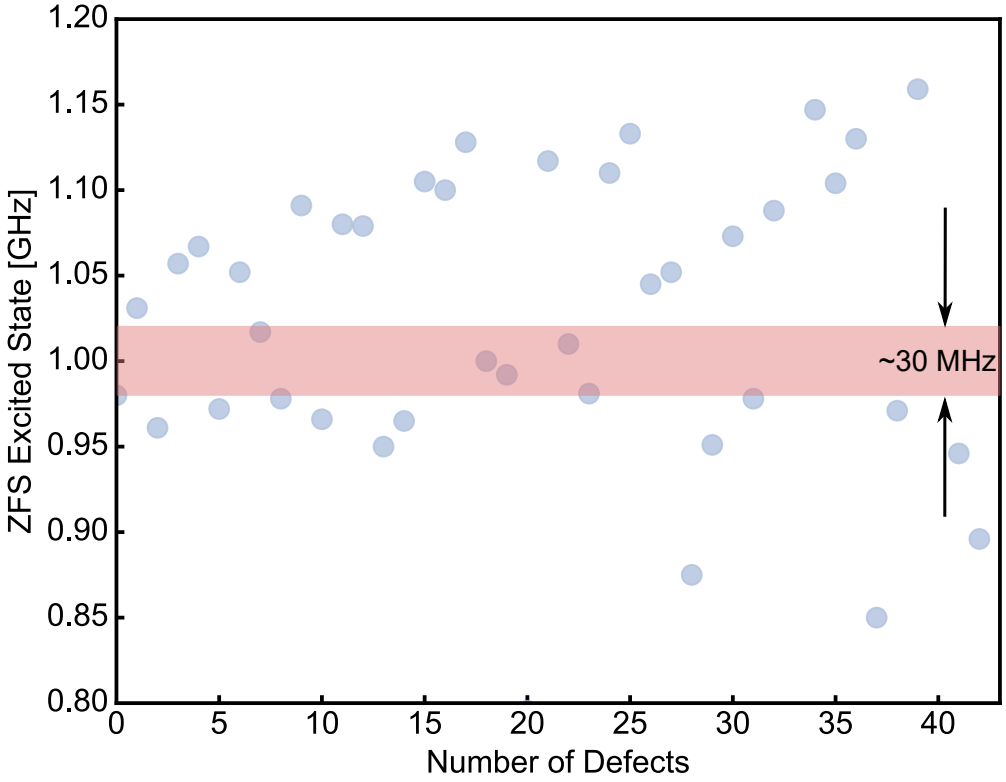

FIGURE 5.5: Excited state ZFS (ZFS_{ex}) statistics: Distribution of the ZFS_{ex} of V_{Si} centres in 4H-SiC. The x-axis describes the number of V_{Si} centre and the y-axis the ZFS_{ex}. The ZFS_{ex} was measured with PLE measurements where the difference between A2 and A1 is the ZFS_{ex} (the ZFS_{gs} is subtracted). The shaded red region shows the FTL linewidth on the absorption lines.

the slightly stronger dipole moment in the excited state in comparison to the ground state, the excited state is affected stronger by local strain. This indicates that a detailed analysis of the effect of strain in the excited state ZFS is needed. Fig. 5.5 shows a detailed analysis of the excited state ZFS_{ex} of 50 V_{Si} centres in 4H-SiC. The x-axis represents the number of V_{Si} centres and the y-axis the exited state ZFS_{ex} of each V_{Si} centre. The graph shows that the distribution of the excited state ZFS has a range of $\approx \pm$ 150 MHz. The shaded red region represents the FTL linewidth.

Fig. 5.6 shows further that the strain in the crystal does not only affect the excited state ZFS but also the absolute energy separation between ground and excited states. The excited state ZFS for the A1 optical transition decreases with increasing of the relative energy between ground and excited states. This behavior is an indicator that the ZFS in the excited state is tunable by applying strain. To achieve a spectral overlap between two spatially separated V_{Si} centres both transitions A1 and A2 need to overlap within the FTL linewidth. To achieve this situation, also the ZFS_{ex} needs to be identical. This scenario becomes likely as it can be seen in Fig. 5.6. Strain can be applied to the crystal to tune the excited state ZFS. The statistics in Fig. 5.4 shows that roughly $\approx$ 14 % of absorption lines for V_{Si} centre in 4H-SiC do perfectly overlap. The most likely explanation for this statistics is a spectral

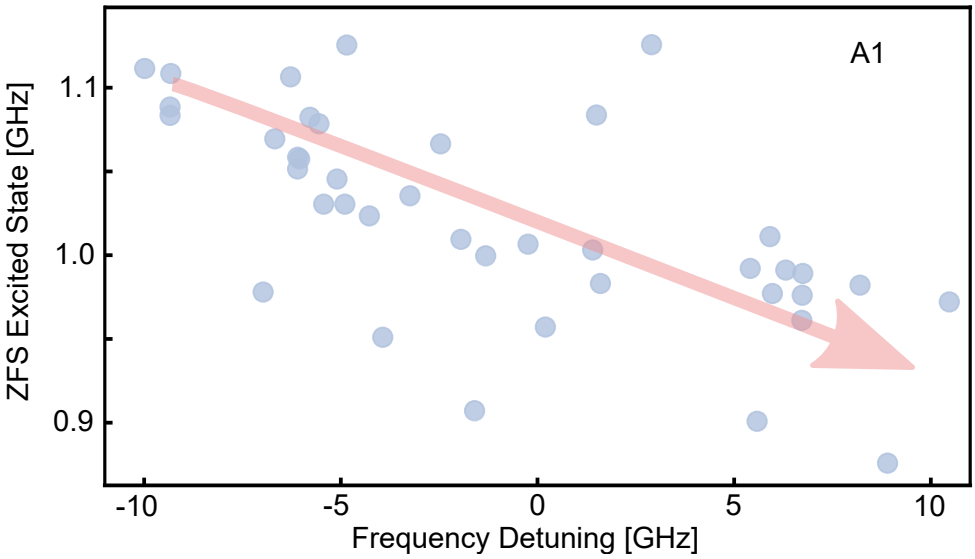

FIGURE 5.6: Excited state zero field splitting functin of the A1 as a absorption line frequency detuning. The excited state zero field splitting changes due to different strain at different locations of the V_{Si} centre in the 4H-SiC crystal.

overlap between A1 for one V_{Si} centre and A2 for a second V_{Si} centre. If I take this value into account my measurement shows an upper limit behavior for the V_{Si} centre in 4H-SiC.

5.1.6 Silicon Vacancy Centres with Small Detunings

There have been many efforts to realize a solid state quantum memory and register with individual optical manipulation and readout (Morton et al., 2008; Rabl et al., 2006; Waldherr et al., 2014; Robledo et al., 2011). It has been shown with NV-centres in diamond that one can entangle two distinct NV-centre at room temperature with dipole-dipole coupling (Dolde et al., 2012; Jakobi et al., 2016). To realize a fully functional quantum system, one would need to individually optically address and manipulate two (or more) dipole-dipole coupled NV-centres at 4 K. Unfortunately, this has not been shown yet. I show in this section that the V_{Si} centres in 4H-SiC may solve this problem. I present two V_{Si} centres located within the diffraction limit. Both V_{Si} centres can be individually optically addressed and manipulated. Additionally, the emission of one optical transition of each V_{Si} centre overlaps with the other V_{Si} centre. The emission can be used for entanglement experiments.

The crystal strain affects V_{Si} centre in 4H-SiC on a sub-micrometer spatial range (Meesala et al., 2018). The crystal field and the similar dipole moment shields the V_{Si} centre in 4H-SiC against most of the strain-effects and stray electric fields (introduced by ionizing processes) inside the crystal, but only $\approx$ 14 % of all V_{Si} centres in 4H-SiC do spectrally overlap (see Fig. 5.4). A better approach would be to create two V_{Si} centres separated within the diffraction limit (Strutt, 1872). I use in my setup a 861 nm laser and a microscope objective with a numerical aperture of 0.9. The diffraction limit in this case is $\approx$ 480 nm (the diffraction limit shows the minimal resolvable spectral resolution on my

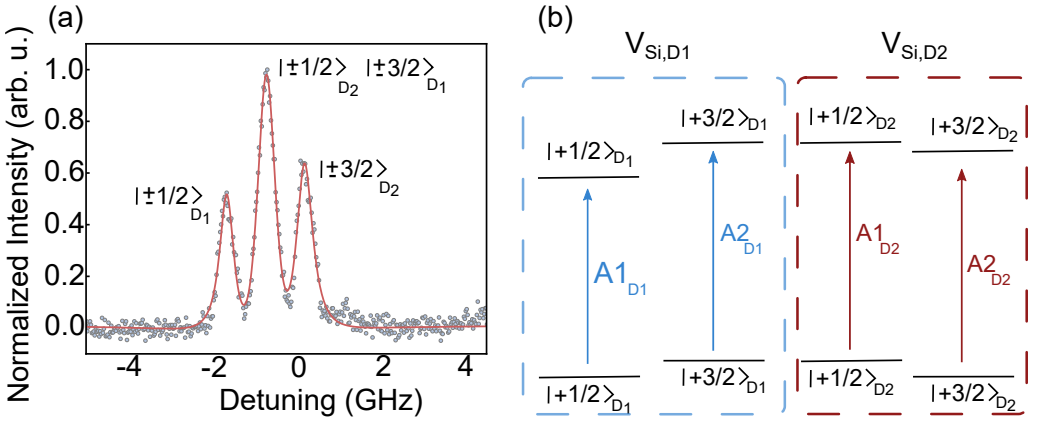

FIGURE 5.7: Indistinguishable emitted photon emission of two silicon vacancy centres within the diffraction limit. (a) PLE measurement of two V_{Si} centre where the central peak shows spectral overlap between the A2 of the first V_{Si1} and A1 of the second V_{Si2}. (b) Level structure configuration with two spectrally overlapping V_{Si} centres.

experiment). The desired distance between two V_{Si} centres would be in a range of ten nanometer to still observe dipole-dipole coupling in the range of some 10 kHz. Both V_{Si} centres within a range of 480 nm still feel a different magnitude of strain. The absolute difference in strain is expected to increase with spatial distance between two V_{Si} centres. A PLE measurement of two V_{Si} centres can be seen in Fig. 5.7 (a). The PLE result shows a measurement with three peaks. The first peak corresponds the A1 optical transition of the first V_{Si} centre called V_{Si1}. The third peak corresponds to the A2 optical transition of the second V_{Si} centre called V_{Si2}. The centre peak is a overlap between A2 from V_{Si1} and A1 from V_{Si2}. If one photon is emitted at the central optical transition it is unknown from which V_{Si} centre(different spin state) the photon was emitted. This indicates that in this configuration, the emitted photons at the central optical transition are indistinguishable (same linewidth, polarization....). The level scheme of two V_{Si} centres with the configuration of Fig. 5.7 (a) can be seen in (b). This configuration can be used for entanglement creation of spatially distributed V_{Si} centres in 4H-SiC.
A protocol for a spin-photon entanglement with two V_{Si}-centre with spectral overlap between $A2_{D1}/A1_{D2}$ can be seen here:

1. Initialize $V_{Si,D1}$ into $|\pm 3/2\rangle$ via excitation on $A1_{D1}$
2. Initialize $V_{Si,D2}$ into $|\pm 1/2\rangle$ via excitation on $A2_{D2}$
3. Ground state MW to generate the state $(\sqrt{\alpha}|\pm 3/2\rangle_{D1}+\sqrt{1-\alpha}|\pm 1/2\rangle_{D1})\otimes(\sqrt{\alpha}|\pm 1/2\rangle_{D2}+\sqrt{1-\alpha}|\pm 3/2\rangle_{D2})$ with $\alpha \ll 1$
4. Excite both systems along $A2_{D1}/A1_{D2}$
5. Detection of a single photon projects the system into the state $|\Psi^+\rangle = \frac{|\pm 3/2\rangle_{D1}|\pm 1/2\rangle_{D2}+|\pm 1/2\rangle_{D1}|\pm 3/2\rangle_{D2}}{\sqrt{2}}$

CHAPTER 6

Summary, Conclusion and Outlook

In my thesis, I demonstrated that the silicon vacancy V_1 centre in 4H-SiC has a strong and realistic potential for applications in quantum information distribution, notably in the framework of establishing a quantum repeater network. In such network, high-level quantum computational tasks are to be implemented (error correction, entanglement distillation, Bell state projections), such that the seven DiVincenzo criteria need to be fulfilled (DiVincenzo, 2000b). The five criteria that cover computational tasks are system scalability, ability to initialize qubits, long coherence times, a universal set of quantum gates for multiple qubits, and qubit specific measurement capability. The additional two criteria for networking tasks are an efficient interface between stationary and flying qubits, and interconnectablity between experiments. The results in my thesis show actually that the V_1 silicon vacancy center fulfills almost all of those criteria.

In Chapter 2, I introduce silicon carbide as a promising host material for optically active spin defects. In Section 2.4, I showed several repeatable/scalable methods for creating V_1 centers, such as electron irradiation, focused ion beam bombardment and laser writing (Chen et al., 2018). In Chapter 3, I performed experiments on V_1 ensembles, showing that the electron spin can be controlled to an excellent degree with long coherence times on the millisecond scale. Subsequently, in Chapter 4, those techniques were extended to investigate single silicon vacancy V_1 centers in 4H-SiC. I showed that single V_1 centers could be isolated and individually addressed, and I developed an efficient strategy for ground state spin initialization with up to 97.5 ± 2 % fidelity (see Section 4.7). This allowed me to perform Optically Detected Magnetic Resonance studies with near 100 % contrast, representing a two orders of magnitude improvement compared to the state of the art (see Section 4.4). Thanks to the system's long electron spin coherence times, I was able to resolve the defect's magnetic environments with ≈ 1 kHz resolution (see Section 4.5). I identified a coherently coupled ^{29}Si nuclear spin qubit in the environment of one V_1 center. This milestone achievement opens the path for implementing high-level quantum computational tasks, e.g. via applying a nuclear-spin controlled CNOT gate on the electron spin.

Additionally, long storage time quantum registers are now definitely within reach.
Besides excellent spin properties, I showed that the V_1 silicon vacancy center in 4H-SiC provides also outstanding optical properties. The optical emission spectrum of single V_1 centers showed about 40 % of coherent emission in the zero phonon line (ZPL), which is one order of magnitude higher than for NV centers in diamond (Doherty et al., 2013). Resonant absorption studies in Section 4.3 showed that the ZPL line shows almost no signs of spectral diffusion (on the order of the natural emission linewidth, i.e. 30 MHz). This finding came as a surprise to the community, as it was commonly expected that only quantum systems with structural inversion symmetry could provide stable optical lines due to vanishing permanent dipole moments in ground and excited states (Stoneham, 2001). However, I showed that this constraint can be relaxed, i.e. systems in with (near-)identical ground and excited state dipole moments can also provide ultrastable optical lines. Note that this property does not require inversion symmetry, which opens a completely new avenue in investigating pertinent quantum defect host materials, notably semiconductors with high scalability potential due to their industrial relevance. I further investigated optical selection rules and identified that all optical transitions are spin conserving. This property is key for realizing a high-fidelity interface that connects stationary spin qubits to flying photonic qubits within a quantum network. To evaluate whether such a network could be scaled up by connecting multiple such spin-to-photon interfaces, I performed statistical studies on 50 silicon vacancy V_1 centres. The results in Chapter 5 showed that 14 % of all V_1 silicon vacancy centers provide indistinguishable photon emission, providing a pathway for large-scale optically assisted entanglement generation among multiple V_1 centers. Considering a fiber-based quantum network comprising of multiple V_1 centers, it is crucial to have access to telecom wavelength photons at a wavelength of about 1550 nm where fiber loss is minimal. It turns out that the natural emission wavelength of the V_1 center (861 nm) is ideally suited for nonlinear wavelength conversion to the telecom range with state of the art devices (Lenhard et al., 2017; Krutyanskiy et al., 2017). One key challenge that remains to be addressed is the optimization of the quantum state readout efficiency (Robledo et al., 2011; Neumann et al., 2010). Readout is performed via optical excitation along one desired transition. The presence or absence of photon emission then heralds whether the system is in the associated state spin state or not. For NV centers in diamond, this procedure works with near unity efficiency and fidelity, thanks to the availability of one very efficient optical transition along which several 100 excitation/emission cycles can be performed before an undesired spin-flip occurs. For the V_1 center in 4H-SiC, optical transitions are cycling, however, there are other decay pathways through metastables states, which are not spin conserving. Unfortunately, the excited state coupling to the metastable states is rather strong, such that only a very few optical excitation/emission cycles can be achieved before a spin-flip occurs. Considering that in the current optical setup, only about 0.2 % of all emitted photons are detected, this means that the quantum state readout efficiency is rather low, on the order of 0.5 %. In other words, every experiment has to be repeated about 200 times before one successful measurement outcome is obtained. To improve this situation, I propose two main pathways. On one

hand, by strongly coupling V_1 centers to a photonic cavity mode, one can enhance the optical emission rate via Purcell enhancement, and achieve significantly enhanced light collection efficiency, up to 70 % (Evans et al., 2018). We estimate that a moderate Purcell enhancement of 5-10 should indeed by sufficient to achieve deterministic spin state readout before a spin-flip occurs. Another pathway was demonstrated almost one decade ago here in Stuttgart, and is based on nuclear spin assisted repeated quantum state readout. The idea here is to store the electron spin state on a nearby nuclear spin memory qubit (via a CNOT gate) before the first readout. Thereafter, one applies multiple repetitions of the following sequence: the nuclear spin is (classically) copied onto the electron spin state (via a CNOT gate), and the electron spin is read out again. By repeating this sequence a few 100 times, near deterministic readout can be achieved. In this regard, the di-atomic nature of SiC may be a strongly beneficial, as the nuclear spin baths of ^{29}Si and ^{13}C can be decoupled at magnetic fields of B > 0.1 T. Thus, one could use a ^{13}C nuclear spin memory for quantum processing tasks, and a ^{29}Si for assisting the readout procedure.

In summary, I showed in my thesis that the V_1 silicon vacancy center in 4H-SiC is a unique quantum spintronics system that combines excellent spin and optical properties in one system. Almost all DiVincenzo criteria are fulfilled, promising a great potential for high-level quantum applications. I also outlined pathways toward improving the readout efficiency, which is currently the remaining challenge for the system. Crucially, I clearly demonstrated that the quantum system could provide indistinguishable photon emission. Together with the high industrial relevance of 4H-SiC, this promises system scalability and integration into nano-photonics and electronics structures, and I truly believe that this platform will be used for realizing quantum networking architectures in the near future.

APPENDIX A

Experimental Methods

A.1 Experimental Setup

All experiments were performed at a cryogenic temperature of 4 K in a Montana Instruments Cryostation. A home-built confocal microscope (Nagy et al., 2018b) was used for optical excitation and subsequent fluorescence detection of single silicon vacancies and ensembles. Off-resonant optical excitation of single silicon vacancy centres was performed with a pulsed home build 730 nm diode laser with a tunable laser power up too 20 mW. For resonant optical excitation at 861.4 nm of the V1 excited state an external cavity tunable diode laser (Toptica DL pro) was used. The laser power for the resonant excitation was adjustable from 0.5 to 500 nW (measured in front of the microscope objective). Optical laser pulses with the Toptica DL pro were created with an acoustic-optic modulator. All lasers (two Toptica DL pro and one home build 730 nm laser diode) were coupled into a photonic crystal fiber to overlap the beam path. HWP and a PBS from Thorlabs in excitation path were used to excite the silicon vacancy centre $\vec{E} \parallel \vec{c}$. A 75 μm pin hole was used to filter out unwanted fluorescence background. The spectrometer from Princeton Instruments was coupled with a standard flip mirror from Thorlabs. In front of the spectrometer a half-wave plate and a polarization beamsplitter were placed to analyze during ensemble measurement the emission of the zero phonon line. Fluorescence in front of the APD was collected in the red-shifted phonon sideband (875 - 890 nm) for which I used a tunable long-pass filter (Versa Chrome Edge) from Semrock. To detect light, I used a near infrared enhanced single-photon avalanche photodiode (Excelitas). Two single-photon avalance photodiods are placed in an Hanbury Brown and Twiss configuration for autocorrelation measurements. The used 4H-SiC sample was flipped to the side, i.e. by 90° compared to the c-axis, such that the polarization of the excitation laser was parallel to the c-axis $\vec{E} \parallel \vec{c}$ which allows to excite the V1 excited state with maximum efficiency (Nagy et al., 2018b; Janzén et al., 2009). Note that the solid immersion lenses (SILs) were fabricated on the

side surface. In order to manipulate ground state spin populations, microwaves are applied through a 20 μm thick copper wire located in close proximity to the investigated V1 defect centres.

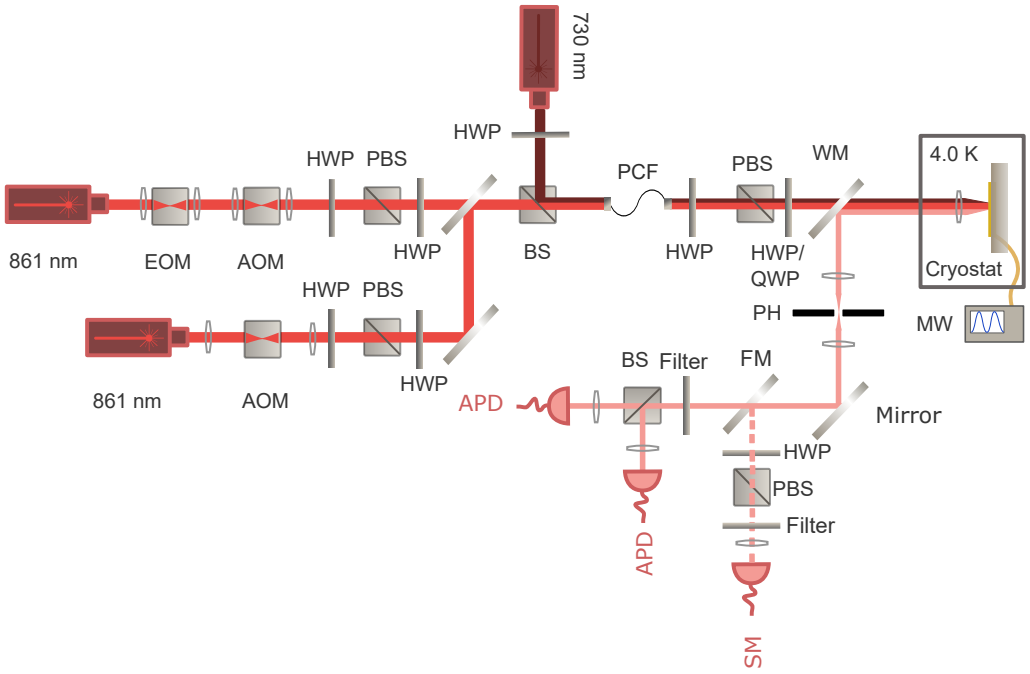

FIGURE A.1: Home build confocal setup with a Montana C2 cryostation. All experiments performed in this thesis where conducted with this setup. Explanation of used elements: AOM: Acoustic-optic modulator, HWP: Half wave plate, PBS: Polarized beam splitter, QWP: Quarter wave plate, BS: 50:50 Beam splitter, SM: Spectrometer, MW: Microwave source, PH: Pin hole, APD: Avalance photo diode, WM: Wedge mirror, PCF: Photonic crystal fiber

A.1.1 Magnetic Field Alignment

In order to allow for selective ground state spin manipulation, level degeneracy has to be lifted. This is realized by applying a magnetic field that has to be precisely aligned along the z-axis of the spin system in order to avoid the appearance of new mixed eigenstates. The z-axis of the spin system is parallel to the c-axis of the 4H-SiC crystal (Sörman et al., 2000). I apply a magnetic field of strength $B_0 = 92$ G with two permanent magnets, placed outside the cryostat chamber. From previous studies, it is already known that the quantization axis of the silicon vacancy centre on a cubic lattice site (usually referred as V_2 centre) (Ivády et al., 2017; Widmann and Lee, 2015) is parallel to the defect centre studied in this report (Sörman et al., 2000). Therefore, I take advantage of an ensemble of V_2 centres found at the edge of the solid immersion lens, which was likely created by ion bombardment during the FIB milling. For a perfectly aligned magnetic field, the splitting between two outer spin resonances of the V_2 centre is $|4D_{gs,V_2}| = 140$ MHz for $|B_0| > |2D_{gs,V_2}$ (Niethammer et al., 2016; Widmann and Lee, 2015). Here, I measure a splitting of 139.93±0.04 MHz, meaning that the magnetic field is aligned within ≈ 1.3 degrees. From ground state

spin spectra as in Fig. 4.7 at the aligned magnetic field, I determine the ZFS of the V_1 centre ground state, $D_{gs} = 4.5 \pm 0.1$ MHz.

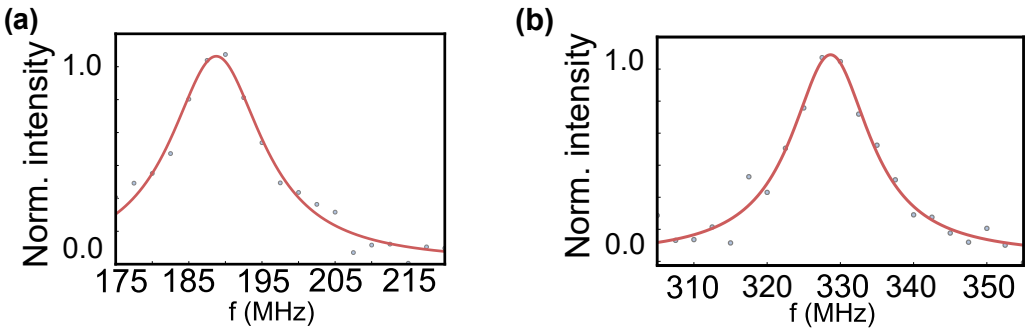

FIGURE A.2: ODMR of an ensemble of silicon vacancy V_2 centres. The graph (a) corresponds to the $|-1/2\rangle \leftrightarrow |-3/2\rangle$ spin transition. In (b) the second spin transition is shown, $|-1/2\rangle \leftrightarrow |-3/2\rangle$. The third spin transition between $|-1/2\rangle \leftrightarrow |+1/2\rangle$ is not visible as $|\pm 1/2\rangle$ have equal populations. The total difference between the central frequency of (a) and (b) is 139.93± 0.04 MHz. This corresponds to an alignment error of the applied magnetic field parallel to the c-axis below 1 ° (see (Niethammer et al., 2016)).

A.2 Experimental Measurement Methods

A.2.1 Optically Detected Magnetic Resonance (ODMR)

Historically was the silicon vacancy V_{Si} centre's electron spin state first investigated with electron spin resonance (ESR) techniques (Wertz, 2012). The principle of ESR is usually an induced static frequency by a resonator and sweeping the amplitude of the magnetic field. The ESR probe emits MW photons when the energy of the sweeped magnetic amplitude and the ground state zero field energy matches. The emitted MW photons can be guided into a cavity to enhance the SNR further. This also indicates that the amount of emitters inside an ESR probe needs to be very high $> 1 \cdot 10^{13} cm^{-13}$ (Balona and Loubser, 1970). Optically Detected Magnetic Resonance (ODMR), which is used in this thesis, is a further improved method of classical ESR. During ODMR the defects are optically stimulated with a laser (730 or 785 nm wavelength) and the emitted photons are detected. Depending on the polarized spin state (see Section 4.6 optically polarization explanation of the V_{Si}) a change in fluorescence is detected during ODMR. This change in fluorescence gives the name "Optically Detected" for this method. The ground state is manipulated during ODMR with MW photons which are either applied with a nano photonic structure on the surface of the sample or with a wire. The applied magnetic field is kept constant and the MW frequency is sweeped. If the MW frequency matches the resonance condition between the ground state spin levels $|-3/2\rangle \leftrightarrow |-1/2\rangle \leftrightarrow |+1/2\rangle \leftrightarrow |+3/2\rangle$, a change in fluorescence can be detected. This gives ODMR in general a couple of advantages in comparison to conventional ESR techniques. ODMR can be integrated into a classical home build confocal microscope and does not need a special device like ESR. Another advantage of ODMR is the increased SNR in comparison to ESR. The better SNR results from

the detection of the change in florescence rather then detecting MW photons. This gives rise to isolate single paramagnetic defects with an confocal setup and perform ODMR on single electron spins. This is a very powerful method to manipulate and control electron spin in solids with a high fidelity ($\approx$ 97% see Section 4.7). ODMR is, like ESR, a universal technique that is not limited to V_{Si} in 4H-SiC, but rather to all paramagnetic impurities in solids (Low, Seitz, and Turnbull, 1960).

A.2.2 Pulsed Optically Detected Magnetic Resonance (ODMR)

The pulse sequence can be seen in Fig. A.3 (c). An important note is that all ODMR measurements on single V_{Si} centers were performed in the pulsed ODMR scheme with resonant laser excitation. The general protocol is the following:

1.) Depolarize the ground state spin population using off-resonant excitation at 730 nm or 785 nm for 1 μs. This ensure that all experiments have identical starting conditions.

2.) Initialize the ground state spin into $|-1/2\rangle$ by simultaneously applying the resonant laser on the A2 transition and microwaves connecting the spin levels $|+1/2\rangle \leftrightarrow |+3/2\rangle$ for 80 μs. Alternatively, the ground state can be initialized into $|-1/2\rangle$ using the resonant laser on the A2 transition with microwaves connecting the spin levels $|-1/2\rangle \leftrightarrow |-3/2\rangle$.

3.) Apply a MW pulse at a frequency in the range of 250 MHz to 263 MHz. The length of the pulse is chosen to perform roughly a π-rotation between the spin levels $|+1/2\rangle \leftrightarrow |+3/2\rangle$.

4.) Read out the spin population in $|\pm 1/2\rangle$ or $|\pm 3/2\rangle$ using resonant excitation on the A1 or A2 transition, respectively. Typically, a readout time of 500 ns is used, however, only photon detection events within the first 120 ns are considered to maximise the signal-to-noise ratio.

For each run of the above-described protocol, I detect $\approx 1.8 \cdot 10^{-3}$ photons in average. This means that the whole sequence has to be repeated several million times in order to achieve a high-quality signal. All pulsed ODMR measurements presented in my thesis are fitted with a Lorentzian function (Wertheim et al., 1974). Note that the narrowest observable linewidth of pulsed ODMR measurements is limited by the inverse of the spin decoherence time T_2^*. T_2^* can be inferred with a Free Induction Decay (FID) or Ramsey measurement, as will be described later.

A.2.3 Rabi Oscillations

Rabi oscillations describe a coherent oscillation of spin population in a two level system. Fig. A.4 shows a typical data fore Rabi oscillations and the associated pulse scheme. As described in Section A.2.2, the sequence starts by polarizing the ground state spin into $|-1/2\rangle$ or $|+1/2\rangle$. In case the system is initialized into $|-1/2\rangle$ a resonant driving field (MW

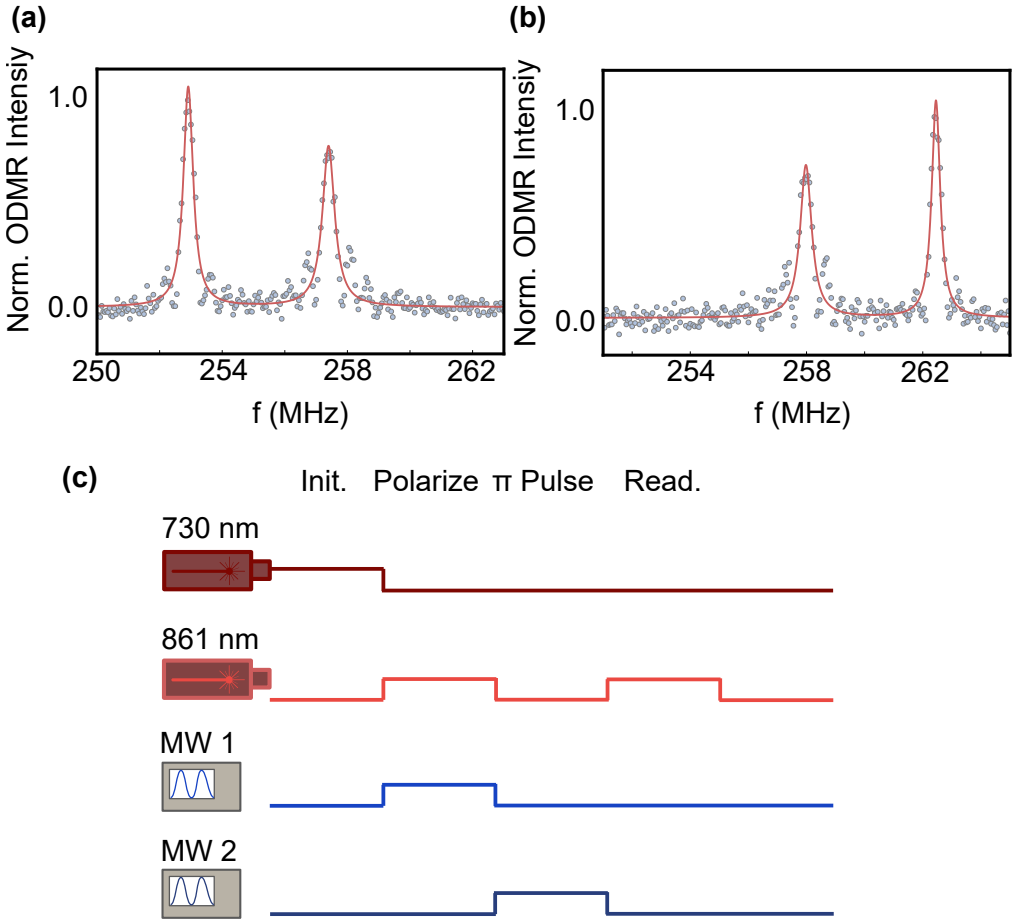

FIGURE A.3: Resonant ODMR measurement on a single silicon vacancy centre. (a) shows the allowed dipole spin transition from $|1/2\rangle \leftrightarrow |-3/2\rangle$ at 253 MHz and second allowed spin transition from $|-1/2\rangle \leftrightarrow |+1/2\rangle$. (b) shows additionally the third allowed spin transition from $|1/2\rangle \leftrightarrow |+3/2\rangle$. The origin why not all transitions can be seen in one single measurement is due to the optical pumping explained in Section 4.6. (c) Pulsed ODMR sequence with 730 nm laser for initialization. 861 nm laser for resonant excitation of the A1 or A2 transition for ground state spin polarization with MW1 and readout. MW 2 applies π pulses.

between $|-1/2\rangle \leftrightarrow |-3/2\rangle$) is subsequently applied with varying time duration τ for coherent spin manipulation. After this MW pulse, a laser resonant either with A1 or A2 reads out the spin state (duration $1\mu s$). During the Rabi measurement the applied resonant driving field is constant in power. If the driving field power would fluctuate, then the measured Rabi Oscillation frequency would become inaccurate. The Rabi oscillation frequency is an important parameter to decide how long a resonant driving field needs to be applied to receive a π-pulse (180° rotation) or $\pi/2$-pulse (90° rotation). The possibility to have access to this kind of spin control is mandatory for any further advanced spin manipulation schemes. Rabi oscillation can be described mathematically in a two level system as

$$S(\tau) = Asin^2\left(\frac{\Omega\tau}{2}\right) + c. \tag{A.1}$$

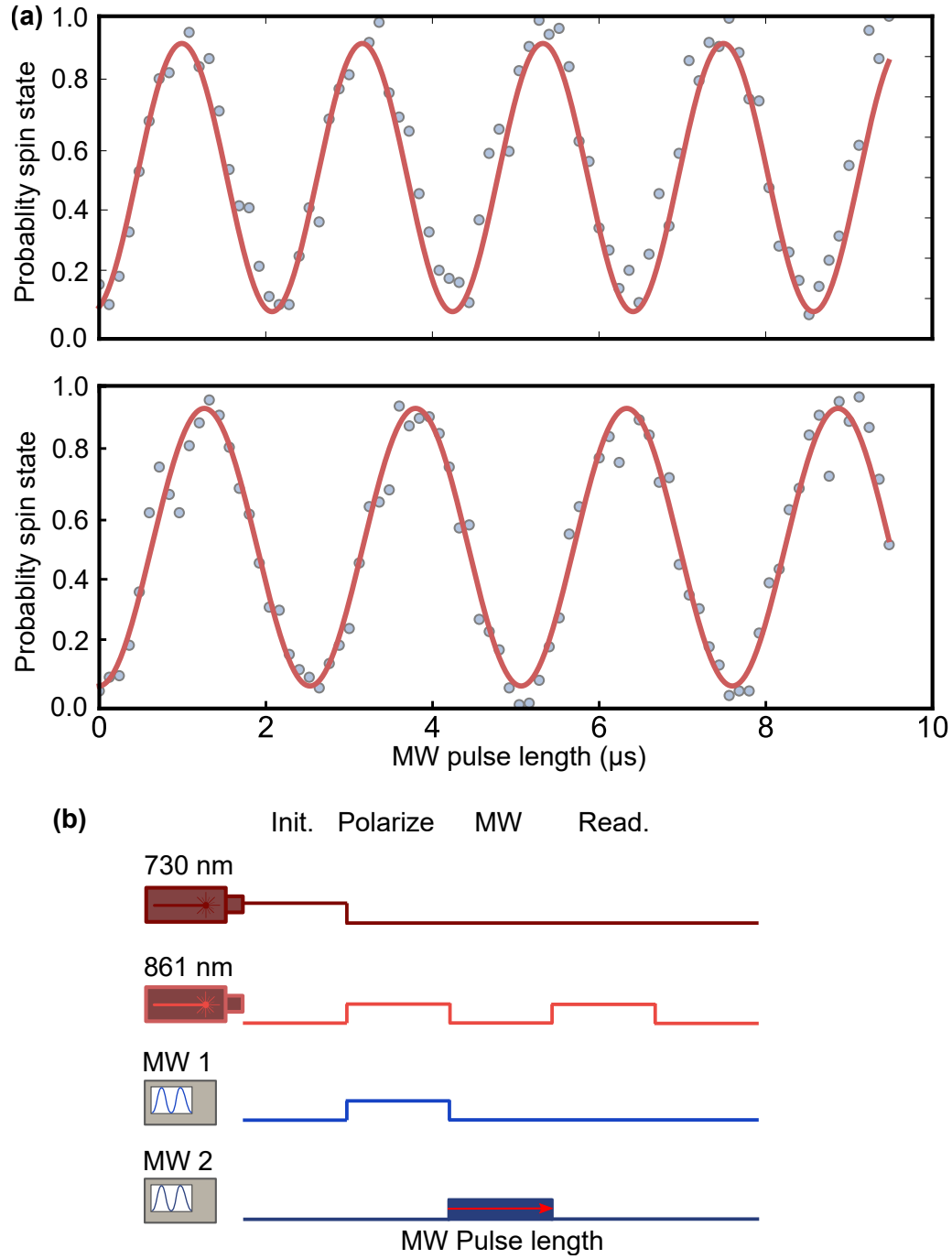

FIGURE A.4: Rabi oscillations. (a) The upper graph shows Rabi oscillations between $|-1/2\rangle \leftrightarrow |+1/2\rangle$. In the lower graph shows Rabi oscillations between $|+1/2\rangle \leftrightarrow |+3/2\rangle$. The upper graph shows a higher Rabi frequency by a factor of ≈ 1.14 what is in excellent agreement with the theoretical expection for a quartet spin system (Mizuochi et al., 2005). (b) Rabi pulse sequence with 730 nm laser for initialization. 861 nm laser for resonant excitation of the A1 or A2 transition for ground state spin polarization with MW1 and readout. MW 2 applies variable pulse lengths.

Here A is the amplitude of the Rabi oscillation and Ω the Rabi frequency. The applied driving field time is τ. The constant c describes an offset due to experimental imperfactions, e.g. the MW cannot be switched on the full power in zero time. This formula is slightly different if the applied driving field is not in resonance with the V_{Si} centre's Larmor frequency. In an experiment, this is achieved if the applied driving field does not perfectly match with the energy between the spin transitions. Mathematically this is described with a finite detuning Δ that alters the Rabi frequency Ω.

$$\Omega_\Delta = \sqrt{\Omega^2 + \Delta^2} \tag{A.2}$$

Not only the Rabi frequency is changed if a detuning is introduced, but also the amplitude of the Rabi oscillation.

$$\tilde{A} = A\left(\frac{\Omega}{\Omega_\Delta}\right) \tag{A.3}$$

The new amplitude $\tilde{A}$ can be described with a Lorentzian of the form

$$\tilde{A} = \frac{A}{1 + \left(\frac{\Delta}{\Omega}\right)^2}. \tag{A.4}$$

If I combine Equation A.1 with A.4 an overall formula for the Rabi oscillation can be derived.

$$S(\tau, \Delta) = \frac{A}{1 + \left(\frac{\Delta}{\Omega}\right)^2} \cdot A sin^2\left(\frac{\Omega_\Delta \tau}{2}\right) + c \tag{A.5}$$

Equation A.5 can also be used to describe pulsed ODMR measurements. During pulsed ODMR measurements is τ defined to be $1/2\Omega$. Additionally, the frequency is changed which is taken into account with a frequency depending detuning $\delta(\upsilon)$.

A.2.4 Ramsey Measurement

The Ramsey scheme is an advanced pulse protocol for magnetic field sensing. It is also known as free induced decay (Ramsey, 1950). Ramsey measurements are used in this thesis to analyze spin decoherence ($T_2^\star$) of V_{Si} centres. Spin decoherence gives an estimation of the magnetic noise at the lattice position of the V_{Si} centre. The pulse protocol can be seen in Fig. A.5. First, the ground state spin is initialized, e.g. into $|+1/2\rangle$. After this step a $\pi/2$-pulse is applied to the system. If I assume that the system is initialized into $m_s = +1/2$ the $\pi/2$-pulse can be applied between $|+1/2\rangle \leftrightarrow |+3/2\rangle$. During a certain waiting time τ the system accumulates a phase between the two superposed states. After the waiting time τ, a second $\pi/2$-pulse is applied to map the accumulated phase onto a population of the eigenstates $|+1/2\rangle$ and $|+3/2\rangle$. After to the last $\pi/2$-pulse a laser (length 1 μs resonant with A1 or A2) is used to read out the fluorescence difference. Mathematically, the measurement can be explained in the following way. If the system is polarized into $m_s = +1/2$ the first $\pi/2$-pulse brings the system in a superposition state

$$|\Psi\rangle = \frac{1}{\sqrt{2}}(|+1/2\rangle + |+3/2\rangle). \tag{A.6}$$

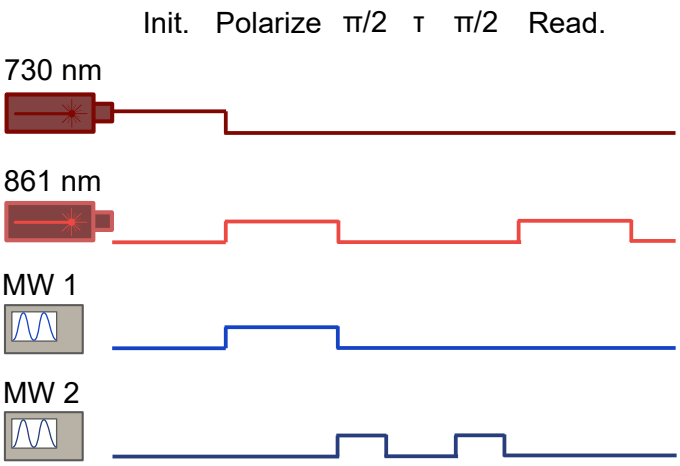

FIGURE A.5: Ramsey pulse scheme. Rabi pulse sequence with 730 nm laser for initialization. 861 nm laser for resonant excitation of the A1 or A2 transition for ground state spin polarization with MW1 and readout. MW2 applies variable pulse lengths.

This state can be represented on the Bloch sphere as an arrow that points towards equator direction (see Fig. 3.5 (d)). The spin $|+3/2\rangle$ will, during the evolution time τ pick up a phase ϕ relative to $|+1/2\rangle$. The magnitude and sign of the phase strongly depends on the detuning Δ. The magnitude can be calculated with Equation 3.3. The evolution time τ and the resulting phase can be calculated as following (Balasubramanian, 2009)

$$\phi(\tau) = \int_0^\tau \Delta(t)dt. \tag{A.7}$$

With Equation A.6, the state can be rewritten as

$$|\Psi\rangle = \frac{1}{\sqrt{2}}(|+1/2\rangle + e^{i\phi}|+3/2\rangle). \tag{A.8}$$

The last $\pi/2$-pulse translates the spin state in a population difference which scales proportionally to the accumulated phase ϕ. This indicates that the measured fluorescence responds scales $P_{|1/2\rangle} \approx sin^2(\phi/2)$ and $P_{|3/2\rangle} \approx cos^2(\phi/2)$ to the frequency of the accumulated phase. A typical Ramsey measurement can be seen in Fig. A.6. If a nuclear spin couples strongly (strong A_{xy} coupling is assumed) to the V_{Si} ground state spin, the result of the Ramsey measurement would show a modulated decay curve. A Fourier transformation of this curve would show the Larmor frequency of the coupled nuclear spin. The decay curve of a Ramsey measurement shows an exponential behavior with a decay constant referred to as $T_2^\star$ (spin dephasing time). The origin of the exponential decay is magnetic noise in the lattice, that is measured as phase accumulation of the V_{Si} centre. The exponential decay can be described by the following equation:

$$S(\tau) = e^{-\frac{\tau}{T_2^\star}} \sum_i A_i cos(2\pi\Delta_i\tau + \phi_i) + c. \tag{A.9}$$

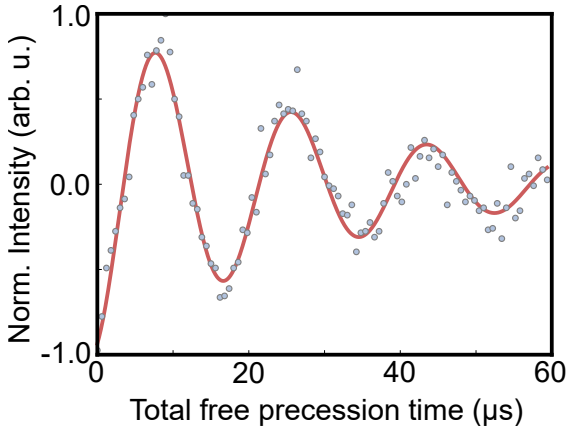

FIGURE A.6: Ramsey measurement. Ramsey measurement with $\Delta \approx 50$ kHz detuning. The detuning can be seen as oscillation in the signal. The V_{Si} was polarized into $|+1/2\rangle$ and pulses were performed between $|+1/2\rangle \leftrightarrow |+3/2\rangle$. The measured spin decoherence is $T_2^\star \approx 29\ \mu s$.

The variable Δ_i is the detuning of the applied microwave, A_i the amplitude, ϕ the phase, τ the free evolution time and c the offset (Staudacher, 2015). The second part of the equation becomes important when a beating (coupling to a nuclear spin) is observed.

A.2.5 Hahn-Echo Measurement

An improved pulse scheme to increase the spin coherence is the Hahn-Echo sequence. The Hahn-Echo pulse sequence was first introduced by Erwin Hahn in 1950 (Hahn, 1950). The sequence follows the Ramsey pulse scheme with a π-pulse in between the $\pi/2$ pulses (see Fig. A.7). The π-pulse between the $\pi/2$ pulses refocuses the spin evolution. Constant magnetic stray fields on this time scale can be canceled out. To understand the mechanism of the refocusing pulse, a more detailed model needs to be discussed. The first $\pi/2$-pulse creates a superposition state

$$|\Psi\rangle = \frac{1}{\sqrt{2}}(|+1/2\rangle + |+3/2\rangle). \tag{A.10}$$

The last $\pi/2$-pulse projects the spin system to a fluorescence difference. The origin of dephasing during Ramsey measurements are small changes (fluctuations) of the magnetic field at the position of the V_{Si}. These small fluctuations are responsible that spins pick up slightly different phases during the free precession acquisition time τ for each measurement. The same effect is also visible after the first $\pi/2$-pulse during the Hahn-Echo measurement. The effect of the π-pulse is that the system accumulates the magnetic noise with a phase change of ($180^\circ \rightarrow \pi$-pulse in x direction). This behavior neglects for a certain frequency range (magnetic noise) the spin dephasing (see Fig. A.8 for a Bloch sphere representation). Another way to look at the behavior is the sensitivity function of the Hahn-Echo pulse scheme. The sensitivity function in the time domain of a Ramsey measurement is a rectangular function with length τ and amplitude of 1. In the scenario of Hahn-Echo, the central π-pulse inverts the effective sensitivity after half of the free precession

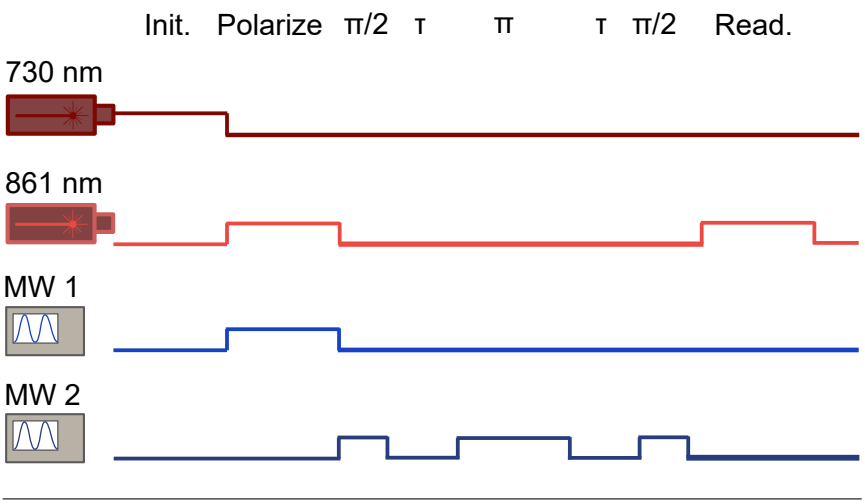

FIGURE A.7: Hahn-Echo measurement: All spin states are first equally populated with a 730 nm laser pule. In the next step, the system is polarized into one spin state. A $\pi/2$-pulse creates a superposition state (see Fig. 3.5 (a)). The spins are now dephasing on the equator plane (see Fig. 3.5 (d)). The π-pulse is inverting (refocusing) the dephased spins. The last $\pi/2$-pulse projects a florescence difference caused by dephasing back to an eigenstate.

time. Constant magnetic fields are then canceled out after the π-pulse. This also indicates that the Hahn-Echo measurement can only be used to detect non constant magnetic fluctuations (Staudacher, 2015; Aslam et al., 2017). A typical Hahn-Echo measurement decay curve can be seen in Fig. 4.9 (a). The origin of the dephasing in Hahn-Echo measurements is the so called spin-spin relaxation or transverse relaxation time T_2. This effect is caused by fluctuations in the environment that are not constant during the total free precession time. Another aspect of the Hahn-Echo measurement is the detection of coupled nuclear spins. This effect becomes visible during the measurement as an oscillation of the signal (see Fig. 4.9). In the case of the V_{Si} centre in 4H-SiC can ^{13}C and ^{29}Si isotopes create these oscillations. The nuclear spin bath of 4H-SiC has a statistical polarization. This indicates that the resulting magnetic field caused by isotopes is not canceled out. If the Larmor precession frequency of ^{13}C or ^{29}Si matches the frequency of the Hahn-Echo measurement the resulting Larmor frequency will create an oscillation in the signal. This can be seen in Fig. 4.9. The physical reason of the oscillation is, if the free precession time τ matches with an odd multiple of ^{13}C or ^{29}Si Larmor frequency during the measurement a collapse will be seen. During even multiples the effect can be canceled out and a revival occurs in the signal. This effect during the measurement is called Electron-Spin-Echo Envelope Modulation (ESEEM). A fitting function for this behavior can be seen here:

$$S(\tau) = Aexp\Big[-\frac{\tau}{T_2}\Big]^n \sum_i exp\Big[-\Big(\frac{\tau - 2i\tau_{Larmor}}{\tau_{Revival}}\Big)^2\Big]. \tag{A.11}$$

Here τ_{Larmor} is the Larmor frequency of either ^{13}C or ^{29}Si, τ_{def} the revival peak frequency.

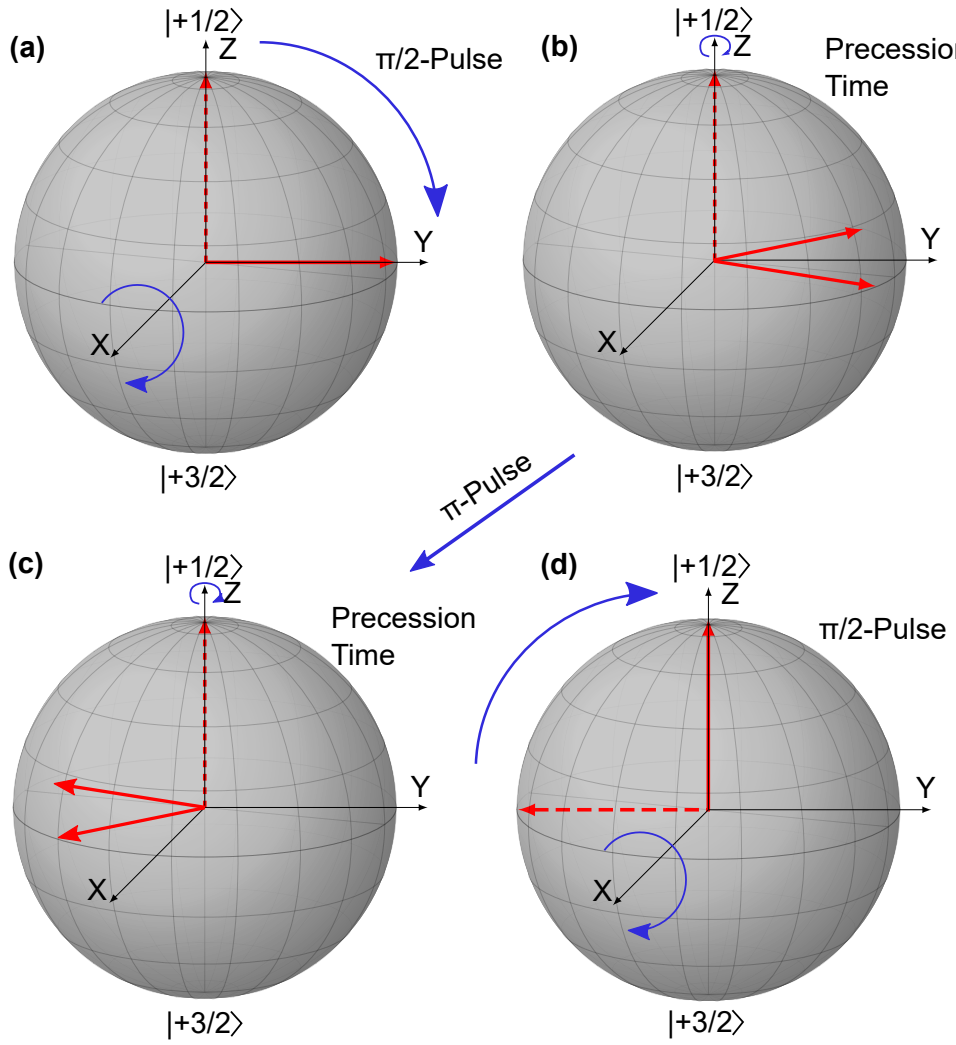

FIGURE A.8: Hahn-Echo sequence visualized on the Bloch sphere: (a) At the begin of the pulse sequence, a $\pi/2$-pulse is applied between $m_s = +1/2$ and $m_s = +3/2$. The resulting state after this pulse is $|\Psi\rangle = \frac{1}{\sqrt{2}}(|+1/2\rangle + |+3/2\rangle)$. (b) The system undergoes now a free precession. This state can now be described as: $|\Psi\rangle = \frac{1}{\sqrt{2}}(|+1/2\rangle + e^{i\phi}|+3/2\rangle)$. (c) After a certain time where the system evolved under a free precession, a π-pulse is applied. The phase of the rotation in the equator plane is now changed by 180°. The system is now refocusing back during the second free precession. (d) The last $\pi/2$-pulse projects the system back to an eigenstate.

A.2.6 Dynamical Decoupling

The first improvement of the spin coherence time was shown with a Hahn-Echo experiment. The origin of the enhanced spin coherence time is the decoupling of the electron spin from its magnetic noise environment. The research community realized already in the 1950's (Carr and Purcell, 1954; Meiboom and Gill, 1958) that more complex pulse sequences would have the potential to stronger decouple the electron spin from the environment. The first improvement of the Hahn-Echo scheme was developed by Carr-Purcell-Maiboom-Gill (CPMG). The scheme can be seen in Fig. A.9 (b). The sequence

is very similar to the Hahn-Echo sequence (see Fig. A.7). The difference is the phase shift

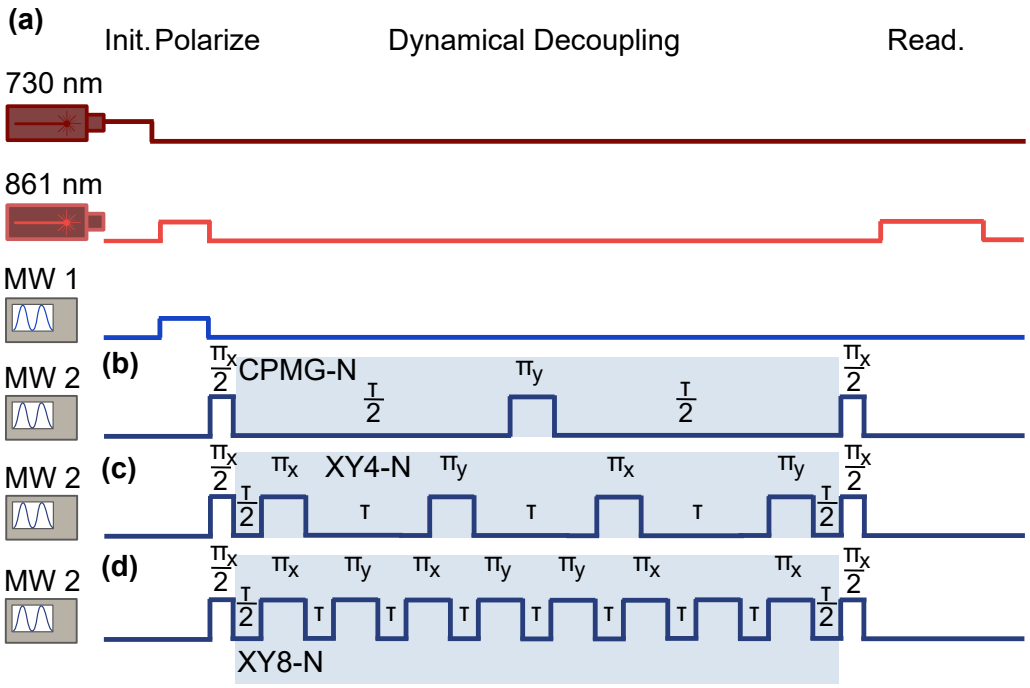

FIGURE A.9: Dynamical Decoupling pulse sequences: (a) The 730 nm laser creates at the begin of every measurement an equal population of the ground state spins. The 861 nm laser and MW1 are polarizing the spin system into one state. The 861 nm laser is also used at the end of the sequence for the readout. (b) CPMG-N applies a π_y-pulse between the $\pi_x/2$-pulses what is N time repeated. (c) XY4-N has 4 π-pulses in between the $\pi_x/2$-pulses what alternate in phase between π_x and π_y. (d) XY8-N is similar to XY4-N but with 8 alternating pulses between the $\pi_x/2$-pulses.

of 180 ° (y-axis on the Bloch sphere) during the π-pulse at the center of the sequence. This phase shifted π-pulse is N times repeated during the measurement to enhance the spin coherence time. The effect of repeating the π-pulse indicates a periodic refocusing effect of the electron spin. A more efficient way of Dynamical Decoupling (DD) is the periodic refocusing in different spatial orientations (De Lange et al., 2010; Souza, Álvarez, and Suter, 2012). The first introduced sequence was the XY4-N (Maudsley, 1986; Gullion and Schaefer, 1991) DD protocol (see Fig. A.9 (c)). The phase of the π-pulse during the XY4-N sequence is periodically changing between the x and y plane on the Bloch sphere (0 or 180 ° phase change). The N in the name stays for the number of repetitions. A more established version of the DD is the XY8-N sequence. The pulse scheme can be seen in Fig. A.9 (d). Another advantage of the XY sequences is the robustness against pulse errors (Souza, Álvarez, and Suter, 2012). The sequence cancels out errors of the MW pulse in amplitude(power) and phase. I used in Chapter 3.6 a XY8-N DD coupling sequence to enhance the spin coherence time. The repetition time N was 50 and 100. The spin coherence time measured with Hahn Echo was 84.9±1.6 μs. The spin coherence time with N = 50 and N = 100 repetitions was respectively T_2 = 286 ±7μs and T_2 = 0.6 ±0.01 ms.

A.2.7 Photoluminescence excitation

Photoluminescence excitation (PLE) is the most frequently used measurement in this thesis. A result of this measurement can be seen in Fig. A.10 (b). The measurement is conducted in a way that an off-resonant laser (730 nm) is first turned on for 1 μs to make sure that the charge state of the V_{Si} is negative. This step becomes mandatory because of a two photon process where the electron of the V_{Si} can be moved to the conduction band. This would result in a new charge state of the V_{Si}. The off-resonant laser brings an electron from the valance band back to the level of the V_{Si} inside the band gap. The level structure of the V_{Si} in the band gap can be seen in Fig. 3.3. I mainly worked in this thesis on

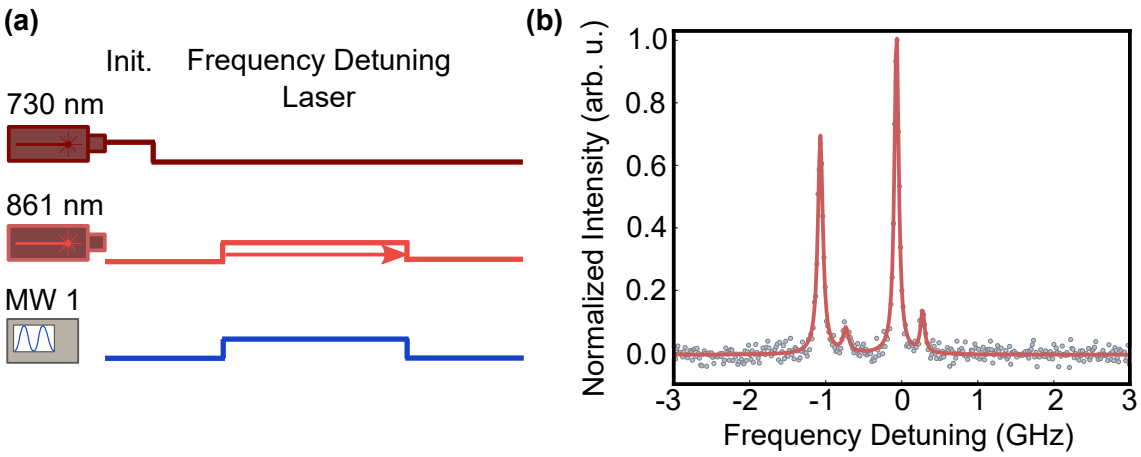

FIGURE A.10: Photoluminescence excitation: (a) The 730 nm laser takes care that the V_{Si} has the right charge state. The 861 nm laser is scanned in frequency such that the frequency of the laser matches the optical transition frequency of the V_{Si}. The MW1 mixes the population during the measurement due to optical pumping (see Chapter 4.6).

the first excited state called V1 (see Fig. 3.6 (a)). The energy of the first excited state V1 is 1.440 eV above the ground state (note that the second excited state called $V1^{'}$ is 1.445 eV above the ground state level). The resonant laser (861 nm $\approx$ 1.440 eV) is continuously detuning the wavelength to reveal the wavelength between the ground and first excited state V1. The level structure of the V_{Si} can be seen in Fig. 4.3 (b). There are two optical transitions that can be exited called A_1 and A_2 (respectively spin conserving transition $m_s = \pm 1/2$ and $m_s = \pm 3/2$). If the energy of the laser matches the energy of the A_1 transition, resonant and side-band photons are emitted and the population is optically pumped into the $m_s = \pm 3/2$ spin state (see Chapter 4.6). To enhance the emission of the photons a microwave is applied to swap the population back into $m_s = \pm 1/2$. The PLE scheme can be seen in Fig. A.10 (a).

Bibliography

Aslam, Nabeel et al. (2017). "Nanoscale nuclear magnetic resonance with chemical resolution". In: *Science* 357.6346, pp. 67–71. ISSN: 0036-8075. DOI: 10.1126/science.aam8697. eprint: http://science.sciencemag.org/content/357/6346/67.full.pdf. URL: http://science.sciencemag.org/content/357/6346/67.

Awschalom, David (2019). "Quantum control of spins in silicon carbide with photons and phonons". In: *Bulletin of the American Physical Society*.

Balasubramanian, G (2009). "G. Balasubramanian, P. Neumann, D. Twitchen, M. Markham, R. Kolesov, N. Mizuochi, J. Isoya, J. Achard, J. Beck, J. Tissler, V. Jacques, PR Hemmer, F. Jelezko, and J. Wrachtrup, Nat. Mater. 8, 383 (2009)." In: *Nat. Mater.* 8, p. 383.

Balona, LA de S and JHN Loubser (1970). "ESR in irradiated silicon carbide". In: *Journal of Physics C: Solid State Physics* 3.11, p. 2344.

Bar-Gill, Nir et al. (2013). "Solid-state electronic spin coherence time approaching one second". In: *Nature communications* 4, p. 1743.

Baranov, Pavel G et al. (2011). "Silicon vacancy in SiC as a promising quantum system for single-defect and single-photon spectroscopy". In: *Physical Review B* 83.12, p. 125203.

Beke, David et al. (2015). "Dominant luminescence is not due to quantum confinement in molecular-sized silicon carbide nanocrystals". In: *Nanoscale* 7.25, pp. 10982–10988.

Bell, John S (1964). "On the einstein podolsky rosen paradox". In: *Physics Physique Fizika* 1.3, p. 195.

Benninghoven, A (1975). "Development in secondary ion mass spectroscopy and applications to surface studies". In: *Surface Science* 53.1, pp. 596–625.

Berry, Michael Victor (2009). "Transitionless quantum driving". In: *Journal of Physics A: Mathematical and Theoretical* 42.36, p. 365303.

Bhatnagar, Mohit and B Jayant Baliga (1993). "Comparison of 6H-SiC, 3C-SiC, and Si for power devices". In: *IEEE Transactions on electron devices* 40.3, pp. 645–655.

Blöchl, Peter E (1994). "Projector augmented-wave method". In: *Physical review B* 50.24, p. 17953.

Boschi, Danilo et al. (1998). "Experimental realization of teleporting an unknown pure quantum state via dual classical and Einstein-Podolsky-Rosen channels". In: *Physical Review Letters* 80.6, p. 1121.

Bouwmeester, Dik et al. (1997). "Experimental quantum teleportation". In: *Nature* 390.6660, p. 575.

Bracher, David O, Xingyu Zhang, and Evelyn L Hu (2017). "Selective Purcell enhancement of two closely linked zero-phonon transitions of a silicon carbide color center". In: *Proceedings of the National Academy of Sciences* 114.16, pp. 4060–4065.

Carr, Herman Y and Edward M Purcell (1954). "Effects of diffusion on free precession in nuclear magnetic resonance experiments". In: *Physical review* 94.3, p. 630.

Carter, SG et al. (2015). "Spin coherence and echo modulation of the silicon vacancy in 4 H- SiC at room temperature". In: *Physical Review B* 92.16, p. 161202.

Castelletto, S. et al. (2018). "Photoluminescence in hexagonal silicon carbide by direct femtosecond laser writing". In: *Opt. Lett.* 43.24, pp. 6077–6080. DOI: 10.1364/OL.43.006077. URL: http://ol.osa.org/abstract.cfm?URI=ol-43-24-6077.

Castelletto, Stefania et al. (2014). "Quantum-confined single photon emission at room temperature from SiC tetrapods". In: *Nanoscale* 6.17, pp. 10027–10032.

Chaussende, D, PJ Wellmann, and M Pons (2007). "Status of SiC bulk growth processes". In: *Journal of Physics D: Applied Physics* 40.20, p. 6150.

Chaussende, Didier and Noboru Ohtani (2019). "Silicon carbide". In: *Single Crystals of Electronic Materials*. Elsevier, pp. 129–179.

Chen, Yu-Chen et al. (2018). "Laser writing of scalable single colour centre in silicon carbide". In: *arXiv preprint arXiv:1812.04284*.

Childress, Lilian and Ronald Hanson (2013). "Diamond NV centers for quantum computing and quantum networks". In: *MRS bulletin* 38.2, pp. 134–138.

Christle, David J et al. (2015). "Isolated electron spins in silicon carbide with millisecond coherence times". In: *Nature materials* 14.2, p. 160.

Christle, David J. et al. (2017). "Isolated Spin Qubits in SiC with a High-Fidelity Infrared Spin-to-Photon Interface". In: *Phys. Rev. X* 7 (2), p. 021046. DOI: 10.1103/PhysRevX.7.021046. URL: https://link.aps.org/doi/10.1103/PhysRevX.7.021046.

Cooperjr, JAMES A and Anant Agarwal (2002). "SiC power-switching devicesThe second electronics revolution?" In: *Proceedings of the IEEE* 90.6.

Coulson, Charles Alfred and Mary J Kearsley (1957). "Colour centres in irradiated diamonds. I". In: *Proceedings of the Royal Society of London. Series A. Mathematical and Physical Sciences* 241.1227, pp. 433–454.

Csóré, A. et al. (2017). "Characterization and formation of NV centers in 3C, 4H, and 6H SiC: An ab initio study". In: *Phys. Rev. B* 96 (8), p. 085204. DOI: 10.1103/PhysRevB.96.085204. URL: https://link.aps.org/doi/10.1103/PhysRevB.96.085204.

Danno, Katsunori, Daisuke Nakamura, and Tsunenobu Kimoto (2007). "Investigation of carrier lifetime in 4 H-Si C epilayers and lifetime control by electron irradiation". In: *Applied physics letters* 90.20, p. 202109.

Dautet, Henri et al. (1993). "Photon counting techniques with silicon avalanche photodiodes". In: *Applied optics* 32.21, pp. 3894–3900.

De Lange, G et al. (2010). "Universal dynamical decoupling of a single solid-state spin from a spin bath". In: *Science* 330.6000, pp. 60–63.

Demichelis, F, CF Pirri, and E Tresso (1992). "Influence of doping on the structural and optoelectronic properties of amorphous and microcrystalline silicon carbide". In: *Journal of Applied Physics* 72.4, pp. 1327–1333.

Deutsch, David (1985). "Quantum theory, the Church–Turing principle and the universal quantum computer". In: *Proceedings of the Royal Society of London. A. Mathematical and Physical Sciences* 400.1818, pp. 97–117.

Deutsch, David and Richard Jozsa (1992). "Rapid solution of problems by quantum computation". In: *Proceedings of the Royal Society of London. Series A: Mathematical and Physical Sciences* 439.1907, pp. 553–558.

DiVincenzo, David P (2000a). "The physical implementation of quantum computation". In: *Fortschritte der Physik: Progress of Physics* 48.9-11, pp. 771–783.

DiVincenzo, David P. (2000b). "The Physical Implementation of Quantum Computation". In: *Fortschritte der Physik* 48.911, pp. 771–783. DOI: 10.1002/1521-3978(200009)48:9/11<771::AID-PROP771>3.0.CO;2-E. eprint: https://onlinelibrary.wiley.com/doi/pdf/10.1002/1521-3978%28200009%2948%3A9/11%3C771%3A%3AAID-PROP771%3E3.0.CO%3B2-E. URL: https://onlinelibrary.wiley.com/doi/abs/10.1002/1521-3978%28200009%2948%3A9/11%3C771%3A%3AAID-PROP771%3E3.0.CO%3B2-E.

Doherty, Marcus W. et al. (2013). "The nitrogen-vacancy colour centre in diamond". In: *Physics Reports* 528.1. The nitrogen-vacancy colour centre in diamond, pp. 1 –45. ISSN: 0370-1573. DOI: https://doi.org/10.1016/j.physrep.2013.02.001. URL: http://www.sciencedirect.com/science/article/pii/S0370157313000562.

Dolde, Florian et al. (2011). "Electric-field sensing using single diamond spins". In: *Nature Physics* 7.6, p. 459.

Dolde, Florian et al. (2012). "Room temperature entanglement between distant single spins in diamond". In: *arXiv preprint arXiv:1212.2804*.

Drabold, David A. (2007). *Theory of Defects in Semiconductors*. 105. Springer-Verlag Berlin Heidelberg.

Epstein, Paul S (1926). "The stark effect from the point of view of Schroedinger's quantum theory". In: *Physical Review* 28.4, p. 695.

Evans, R. E. et al. (2018). "Photon-mediated interactions between quantum emitters in a diamond nanocavity". In: *Science* 362.6415, pp. 662–665. ISSN: 0036-8075. DOI: 10.1126/science.aau4691. eprint: http://science.sciencemag.org/content/362/6415/662.full.pdf. URL: http://science.sciencemag.org/content/362/6415/662.

F Koehl, William et al. (Nov. 2011). "Room temperature coherent control of defect spin qubits in silicon carbide". In: *Nature* 479, pp. 84–7. DOI: 10.1038/nature10562.

Falk, AL (2013). "AL Falk, BB Buckley, G. Calusine, WF Koehl, VV Dobrovitski, A. Politi, CA Zorman, PX-L. Feng, and DD Awschalom, Nat. Commun. 4, 1819 (2013)." In: *Nat. Commun.* 4, p. 1819.

Feynman, Richard P. (1982). "Simulating physics with computers". In: *International Journal of Theoretical Physics* 21.6, pp. 467–488. ISSN: 1572-9575. DOI: 10.1007/BF02650179. URL: https://doi.org/10.1007/BF02650179.

Gajdoš, M et al. (2006). "Linear optical properties in the projector-augmented wave methodology". In: *Physical Review B* 73.4, p. 045112.

Gali, Adam and Jeronimo R Maze (2013). "Ab initio study of the split silicon-vacancy defect in diamond: Electronic structure and related properties". In: *Physical Review B* 88.23, p. 235205.

Gali, Adam et al. (2009). "Theory of spin-conserving excitation of the N- V- center in diamond". In: *Physical review letters* 103.18, p. 186404.

Gao, F. and W. J. Weber (May 2002). "Empirical potential approach for defect properties in 3C-SiC". In: *Nuclear Instruments and Methods in Physics Research B* 191, pp. 504–508. DOI: 10.1016/S0168-583X(02)00600-6.

Giustina, Marissa et al. (2015). "Significant-loophole-free test of Bells theorem with entangled photons". In: *Physical review letters* 115.25, p. 250401.

Glass, RC et al. (1997). "SiC seeded crystal growth". In: *physica status solidi (b)* 202.1, pp. 149–162.

Golter, D Andrew et al. (2016). "Optomechanical quantum control of a nitrogen-vacancy center in diamond". In: *Physical review letters* 116.14, p. 143602.

Green, BL et al. (2017). "Neutral silicon-vacancy center in diamond: spin polarization and lifetimes". In: *Physical review letters* 119.9, p. 096402.

Gruber, A. et al. (1997). "Scanning Confocal Optical Microscopy and Magnetic Resonance on Single Defect Centers". In: *Science* 276.5321, pp. 2012–2014. ISSN: 0036-8075. DOI: 10.1126/science.276.5321.2012. eprint: http://science.sciencemag.org/content/276/5321/2012.full.pdf. URL: http://science.sciencemag.org/content/276/5321/2012.

Gullion, Terry and Jacob Schaefer (1991). "Elimination of resonance offset effects in rotational-echo, double-resonance NMR". In: *Journal of Magnetic Resonance (1969)* 92.2, pp. 439–442.

Hahn, Erwin L (1950). "Spin echoes". In: *Physical review* 80.4, p. 580.

Harris, Gary Lynn (1995). *Properties of silicon carbide*. 13. Iet.

Heine, Volker, Ching Cheng, and Richard J Needs (1991). "The preference of silicon carbide for growth in the metastable cubic form". In: *Journal of the American Ceramic Society* 74.10, pp. 2630–2633.

Hemmingsson, Carl et al. (1997). "Deep level defects in electron-irradiated 4H SiC epitaxial layers". In: *Journal of applied physics* 81.9, pp. 6155–6159.

Hensen, Bas et al. (2015). "Loophole-free Bell inequality violation using electron spins separated by 1.3 kilometres". In: *Nature* 526.7575, p. 682.

Heremans, F. J., C. G. Yale, and D. D. Awschalom (2016). "Control of Spin Defects in Wide-Bandgap Semiconductors for Quantum Technologies". In: *Proceedings of the IEEE* 104.10, pp. 2009–2023. ISSN: 0018-9219. DOI: 10.1109/JPROC.2016.2561274.

Ito, Tomonori et al. (2011). "Theoretical investigations for the polytypism in semiconductors". In: *Journal of crystal growth* 318.1, pp. 141–144.

Ivády, Viktor et al. (2017). "Identification of Si-vacancy related room-temperature qubits in 4 H silicon carbide". In: *Physical Review B* 96.16, p. 161114.

Iwamoto, Naoya and Bengt G. Svensson (Dec. 2015). "Point Defects in Silicon Carbide". In: vol. 91, pp. 369–407. DOI: 10.1016/bs.semsem.2015.02.001.

Iwasaki, Takayuki et al. (2015). "Germanium-vacancy single color centers in diamond". In: *Scientific reports* 5, p. 12882.

Iwasaki, Takayuki et al. (2017). "Tin-vacancy quantum emitters in diamond". In: *Physical review letters* 119.25, p. 253601.

Iwata, Hisaomi and Kohei M Itoh (2001). "Donor and acceptor concentration dependence of the electron Hall mobility and the Hall scattering factor in n-type 4H–and 6H–SiC". In: *Journal of Applied Physics* 89.11, pp. 6228–6234.

Jakobi, Ingmar et al. (2016). "Efficient creation of dipolar coupled nitrogen-vacancy spin qubits in diamond". In: *Journal of Physics: Conference Series*. Vol. 752. 1. IOP Publishing, p. 012001.

Janzén, Erik et al. (2009). "The silicon vacancy in SiC". In: *Physica B: Condensed Matter* 404.22, pp. 4354–4358.

Jelezko, Fedor et al. (2004). "Observation of coherent oscillations in a single electron spin". In: *Physical review letters* 92.7, p. 076401.

Kildemo, Morten (2003). *Optical properties of silicon carbide polytypes*. Tech. rep. CERN-OPEN-2003-047. Geneva: CERN. URL: https://cds.cern.ch/record/639624.

Kimoto, Tsunenobu (2015). "Material science and device physics in SiC technology for high-voltage power devices". In: *Japanese Journal of Applied Physics* 54.4, p. 040103.

— (2016). "Bulk and epitaxial growth of silicon carbide". In: *Progress in Crystal Growth and Characterization of Materials* 62.2. Special Issue: Recent Progress on Fundamentals and Applications of Crystal Growth; Proceedings of the 16th International Summer School on Crystal Growth (ISSCG-16), pp. 329 –351. ISSN: 0960-8974. DOI: https://doi.org/10.1016/j.pcrysgrow.2016.04.018. URL: http://www.sciencedirect.com/science/article/pii/S0960897416300213.

— (2019). "SiC material properties". In: *Wide Bandgap Semiconductor Power Devices*. Elsevier, pp. 21–42.

Kimoto, Tsunenobu and James A Cooper (2014). *Fundamentals of Silicon Carbide Technology: Growth, Characterization, Devices and Applications*. John Wiley & Sons.

King-Smith, RD and David Vanderbilt (1993). "Theory of polarization of crystalline solids". In: *Physical Review B* 47.3, p. 1651.

Kobayashi, Takuma et al. (2019). "Native point defects and carbon clusters in 4H-SiC: A hybrid functional study". In: *arXiv preprint arXiv:1901.05667*.

Koehl, William F. et al. (2017). "Resonant optical spectroscopy and coherent control of Cr^{4+} spin ensembles in SiC and GaN". In: *Phys. Rev. B* 95 (3), p. 035207. DOI: 10.1103/PhysRevB.95.035207. URL: https://link.aps.org/doi/10.1103/PhysRevB.95.035207.

Kraus, H. et al. (2017). "Three-Dimensional Proton Beam Writing of Optically Active Coherent Vacancy Spins in Silicon Carbide". In: *Nano Letters* 17.5. PMID: 28350468, pp. 2865–2870. DOI: 10.1021/acs.nanolett.6b05395. eprint: https://doi.org/10.1021/acs.nanolett.6b05395. URL: https://doi.org/10.1021/acs.nanolett.6b05395.

Kresse, Georg and Jürgen Furthmüller (1996a). "Efficiency of ab-initio total energy calculations for metals and semiconductors using a plane-wave basis set". In: *Computational materials science* 6.1, pp. 15–50.

— (1996b). "Efficient iterative schemes for ab initio total-energy calculations using a plane-wave basis set". In: *Physical review B* 54.16, p. 11169.

Kresse, Georg and Jürgen Hafner (1993). "Ab initio molecular dynamics for liquid metals". In: *Physical Review B* 47.1, p. 558.

Krutyanskiy, V et al. (2017). "Polarisation-preserving photon frequency conversion from a trapped-ion-compatible wavelength to the telecom C-band". In: *Applied Physics B* 123.9, p. 228.

Leblebici, Anil et al. (2019). "Smart Energy". In: *Nano-Tera. ch.* Springer, pp. 109–137.

Lee, S-Y et al. (2010). "Spin-dependent processes in amorphous silicon-rich silicon-nitride". In: *Applied Physics Letters* 97.19, p. 192104.

Lenhard, Andreas et al. (2017). "Coherence and entanglement preservation of frequency-converted heralded single photons". In: *Optics express* 25.10, pp. 11187–11199.

Lingner, Th et al. (2001). "Structure of the silicon vacancy in 6 H- SiC after annealing identified as the carbon vacancy–carbon antisite pair". In: *Physical Review B* 64.24, p. 245212.

Lohrmann, A et al. (2015). "Single-photon emitting diode in silicon carbide". In: *Nature communications* 6, p. 7783.

Low, William, Frederick Seitz, and David Turnbull (1960). *Paramagnetic resonance in solids*. Vol. 2. Academic Press New York.

M. Stoneham, A and R Smoluchowski (Jan. 1976). "Theory of Defects in Solids: Electronic Structure of Defects in Insulators and Semiconductors". In: *Physics Today - PHYS TODAY* 29. DOI: 10.1063/1.3023378.

Matsunami, Hiroyuki and Tsunenobu Kimoto (1997). "Step-controlled epitaxial growth of SiC: High quality homoepitaxy". In: *Materials Science and Engineering: R: Reports* 20.3, pp. 125–166.

Maudsley, AA (1986). "Modified Carr-Purcell-Meiboom-Gill sequence for NMR fourier imaging applications". In: *Journal of Magnetic Resonance (1969)* 69.3, pp. 488–491.

Meesala, Srujan et al. (2018). "Strain engineering of the silicon-vacancy center in diamond". In: *Physical Review B* 97.20, p. 205444.

Meiboom, Saul and David Gill (1958). "Modified spin-echo method for measuring nuclear relaxation times". In: *Review of scientific instruments* 29.8, pp. 688–691.

Mercier, Frédéric and Shin ichi Nishizawa (2012). "Role of surface effects on silicon carbide polytype stability". In: *Journal of Crystal Growth* 360. 5th International Workshop on Crystal Growth Technology, pp. 189 –192. ISSN: 0022-0248. DOI: https://doi.org/10.1016/j.jcrysgro.2011.11.052. URL: http://www.sciencedirect.com/science/article/pii/S0022024811009754.

Michel, C et al. (2009). "Influence of disorder on electrically and optically detected electron spin nutation". In: *Physical Review B* 79.5, p. 052201.

Mizuochi, N et al. (2002). "Continuous-wave and pulsed EPR study of the negatively charged silicon vacancy with S= 3 2 and C 3 v symmetry in n-type 4 H- SiC". In: *Physical Review B* 66.23, p. 235202.

Mizuochi, N et al. (2005). "Spin multiplicity and charge state of a silicon vacancy (T V 2 a) in 4 H-SiC determined by pulsed ENDOR". In: *Physical review B* 72.23, p. 235208.

Moore, Gordon (1965). "Moores law". In: *Electronics Magazine* 38.8, p. 114.

Morton, John JL et al. (2008). "Solid-state quantum memory using the 31 P nuclear spin". In: *Nature* 455.7216, p. 1085.

N. T. Son P. Carlsson, E. Janzen (2006). "Divacancy in 4H-SiC". English. In: *Physical Review Letters* 96.5. ISSN: 0031-9007. DOI: 10.1103/PhysRevLett.96.055501.

Nagy, Roland et al. (2018a). "High-fidelity spin and optical control of single silicon vacancy centres in silicon carbide". In: *arXiv preprint arXiv:1810.10296*.

Nagy, Roland et al. (2018b). "Quantum properties of dichroic silicon vacancies in silicon carbide". In: *Physical Review Applied* 9.3, p. 034022.

Neill, C (2016). "C. Neill, P. Roushan, M. Fang, Y. Chen, M. Kolodrubetz, Z. Chen, A. Megrant, R. Barends, B. Campbell, B. Chiaro, A. Dunsworth, E. Jeffrey, J. Kelly, J. Mutus, PJJ O'Malley, C. Quintana, D. Sank, A. Vainsencher, J. Wenner, TC White, A. Polkovnikov, and JM Martinis, Nat. Phys. 12, 1037 (2016)." In: *Nat. Phys.* 12, p. 1037.

Neu, Elke et al. (2013). "Low-temperature investigations of single silicon vacancy colour centres in diamond". In: *New Journal of Physics* 15.4, p. 043005.

Neudeck, Philip G (1995). "Progress in silicon carbide semiconductor electronics technology". In: *Journal of Electronic Materials* 24.4, pp. 283–288.

Neumann, Philipp et al. (2010). "Single-shot readout of a single nuclear spin". In: *Science* 329.5991, pp. 542–544.

Niethammer, Matthias et al. (2016). "Vector Magnetometry Using Silicon Vacancies in 4 H-SiC Under Ambient Conditions". In: *Physical Review Applied* 6.3, p. 034001.

Oliveira, Felipe Fávaro de et al. (2017). "Tailoring spin defects in diamond by lattice charging". In: *Nature communications*.

Oreg, J, FT Hioe, and JH Eberly (1984). "Adiabatic following in multilevel systems". In: *Physical Review A* 29.2, p. 690.

Paier, Joachim et al. (2006). "Screened hybrid density functionals applied to solids". In: *The Journal of chemical physics* 124.15, p. 154709.

Perdew, John P, Kieron Burke, and Matthias Ernzerhof (1996). "Generalized gradient approximation made simple". In: *Physical review letters* 77.18, p. 3865.

Perlin, Iĭ Evgenevich and Max Wagner (1984). *The dynamical Jahn-Teller effect in localized systems*. Vol. 7. Elsevier Science Ltd.

Planck, Max (1890). "Ueber die erregung von electricität und wärme in electrolyten". In: *Annalen der Physik* 275.2, pp. 161–186.

Rabl, P et al. (2006). "Hybrid quantum processors: molecular ensembles as quantum memory for solid state circuits". In: *Physical review letters* 97.3, p. 033003.

Radulaski, Marina et al. (2017). "Scalable quantum photonics with single color centers in silicon carbide". In: *Nano letters* 17.3, pp. 1782–1786.

Ramsey, Norman F (1950). "A molecular beam resonance method with separated oscillating fields". In: *Physical Review* 78.6, p. 695.

Rao, DD Bhaktavatsala (2015). "DDB Rao, S. Yang, and J. Wrachtrup, Generation of entangled photon strings using NV centers in diamond, Phys. Rev. B 92, 081301 (2015)." In: *Phys. Rev. B* 92, p. 081301.

Raussendorf, Robert and Hans J Briegel (2001). "A one-way quantum computer". In: *Physical Review Letters* 86.22, p. 5188.

Resta, Raffaele (1994). "Macroscopic polarization in crystalline dielectrics: the geometric phase approach". In: *Reviews of modern physics* 66.3, p. 899.

Robledo, Lucio et al. (2011). "High-fidelity projective read-out of a solid-state spin quantum register". In: *Nature* 477.7366, p. 574.

Rogers, Lachlan J et al. (2014a). "All-optical initialization, readout, and coherent preparation of single silicon-vacancy spins in diamond". In: *Physical review letters* 113.26, p. 263602.

Rogers, Lachlan J et al. (2014b). "Multiple intrinsically identical single-photon emitters in the solid state". In: *Nature communications* 5, p. 4739.

Roschke, M. and F. Schwierz (2001). "Electron mobility models for 4H, 6H, and 3C SiC [MESFETs]". In: *IEEE Transactions on Electron Devices* 48.7, pp. 1442–1447. ISSN: 0018-9383. DOI: 10.1109/16.930664.

Rowan, L_G, EL Hahn, and WB Mims (1965). "Electron-spin-echo envelope modulation". In: *Physical Review* 137.1A, A61.

Seo, Hosung et al. (2016). "Quantum decoherence dynamics of divacancy spins in silicon carbide". In: *Nature communications* 7, p. 12935.

Shalm, Lynden K et al. (2015). "Strong loophole-free test of local realism". In: *Physical review letters* 115.25, p. 250402.

Shor, Peter W (1999). "Polynomial-time algorithms for prime factorization and discrete logarithms on a quantum computer". In: *SIAM review* 41.2, pp. 303–332.

Silveira, E et al. (2005). "Excitonic structure of bulk AlN from optical reflectivity and cathodoluminescence measurements". In: *Physical Review B* 71.4, p. 041201.

Simin, D et al. (2017). "Locking of electron spin coherence above 20 ms in natural silicon carbide". In: *Physical Review B* 95.16, p. 161201.

Slichter, Charles P (1990). *Principles of Magnetic Resonance, volume 1 of Springer Series in Solid-State Sciences*.

Son, NT, PN Hai, and Erik Janzén (2001). "Carbon vacancy-related defect in 4H and 6H SiC". In: *Physical Review B* 63.20, p. 201201.

Son, N.T. et al. (1999). "Carbon-vacancy related defects in 4H- and 6H-SiC". In: *Materials Science and Engineering: B* 61-62, pp. 202 –206. ISSN: 0921-5107. DOI: https://doi.org/10.1016/S0921-5107(98)00502-9. URL: http://www.sciencedirect.com/science/article/pii/S0921510798005029.

Sörman, E et al. (2000). "Silicon vacancy related defect in 4H and 6H SiC". In: *Physical Review B* 61.4, p. 2613.

Souza, Alexandre M, Gonzalo A Álvarez, and Dieter Suter (2012). "Robust dynamical decoupling". In: *Philosophical Transactions of the Royal Society A: Mathematical, Physical and Engineering Sciences* 370.1976, pp. 4748–4769.

Soykal, ÖO, Pratibha Dev, and Sophia E Economou (2016). "Silicon vacancy center in 4 H-SiC: Electronic structure and spin-photon interfaces". In: *Physical Review B* 93.8, p. 081207.

Soykal, ÖO and Thomas L Reinecke (2017). "Quantum metrology with a single spin-3 2 defect in silicon carbide". In: *Physical Review B* 95.8, p. 081405.

Srikant, V and D R_ Clarke (1998). "On the optical band gap of zinc oxide". In: *Journal of Applied Physics* 83.10, pp. 5447–5451.

Staudacher, Tobias (2015). *Nuclear Magnetic Resonance Spectroscopy on a Nanoscopic Sample Volume*. Verlag Dr. Hut.

Steeds, John W et al. (2001). "Differentiation between C and Si related damage centres in 4H and 6H SiC by the use of 90-300 kV electron irradiation followed by low temperature photoluminescence microscopy". In: *Materials Science Forum*. Vol. 353. Trans Tech Publications, pp. 381–384.

Stoneham, Arthur Marshall (2001). *Theory of defects in solids: electronic structure of defects in insulators and semiconductors*. Oxford University Press.

Strutt, John W (1872). "On the diffraction of object-glasses". In: *Monthly Notices of the Royal Astronomical Society* 33, p. 59.

Sukachev, Denis D et al. (2017). "Silicon-vacancy spin qubit in diamond: a quantum memory exceeding 10 ms with single-shot state readout". In: *Physical review letters* 119.22, p. 223602.

Szász, Krisztián et al. (2015). "Spin and photophysics of carbon-antisite vacancy defect in 4 H silicon carbide: A potential quantum bit". In: *Physical Review B* 91.12, p. 121201.

Tairov, Yu M and VF Tsvetkov (1978). "Investigation of growth processes of ingots of silicon carbide single crystals". In: *Journal of crystal growth* 43.2, pp. 209–212.

— (1981). "General principles of growing large-size single crystals of various silicon carbide polytypes". In: *Journal of Crystal Growth* 52, pp. 146–150.

Takahashi, J and N Ohtani (1997). "Modified-Lely SiC Crystals Grown in [11-00] and [112-0] Directions". In: *physica status solidi (b)* 202.1, pp. 163–175.

Takayanagi, Kunio, Y Kondo, and H Ohnishi (2001). "Suspended gold nanowires: ballistic transport of electrons". In: *JSAP international* 3.8.

Tamarat, Ph et al. (2006). "Stark shift control of single optical centers in diamond". In: *Physical review letters* 97.8, p. 083002.

Tyryshkin, Alexei M et al. (2012). "Electron spin coherence exceeding seconds in high-purity silicon". In: *Nature materials* 11.2, p. 143.

Vanderbilt, David and RD King-Smith (1993). "Electric polarization as a bulk quantity and its relation to surface charge". In: *Physical Review B* 48.7, p. 4442.

Wagner, Mt et al. (1999). "Zeeman spectroscopy of the neutral silicon vacancy in 6H and 4H SiC". In: *Physica B: Condensed Matter* 273, pp. 663–666.

Wagner, Mt et al. (2000). "Electronic structure of the neutral silicon vacancy in 4 H and 6 H SiC". In: *Physical Review B* 62.24, p. 16555.

Waldherr, Gerald et al. (2014). "Quantum error correction in a solid-state hybrid spin register". In: *Nature* 506.7487, p. 204.

Wallace, JB et al. (2015). "Time constant of defect relaxation in ion-irradiated 3 C-SiC". In: *Applied Physics Letters* 106.20, p. 202102.

Wang, Junfeng et al. (2017). "Scalable Fabrication of Single Silicon Vacancy Defect Arrays in Silicon Carbide Using Focused Ion Beam". In: *ACS Photonics* 4.5, pp. 1054–1059. DOI: 10.1021/acsphotonics.7b00230. eprint: https://doi.org/10.1021/acsphotonics.7b00230. URL: https://doi.org/10.1021/acsphotonics.7b00230.

Weber, JR et al. (2010). "Quantum computing with defects". In: *Proceedings of the National Academy of Sciences* 107.19, pp. 8513–8518.

Wertheim, GK et al. (1974). "Determination of the Gaussian and Lorentzian content of experimental line shapes". In: *Review of Scientific Instruments* 45.11, pp. 1369–1371.

Wertz, John (2012). *Electron spin resonance: elementary theory and practical applications*. Springer Science & Business Media.

Widmann, M and SY Lee (2015). "M. Widmann, S.-Y. Lee, T. Rendler, NT Son, H. Fedder, S. Paik, L.-P. Yang, N. Zhao, S. Yang, I. Booker, A. Denisenko, M. Jamali, SA Momenzadeh, I. Gerhardt, T. Ohshima, A. Gali, E. Janzén, and J. Wrachtrup, Nat. Mater. 14, 164 (2015)." In: *Nat. Mater.* 14, p. 164.

Wolf, Thomas et al. (2015). "Subpicotesla diamond magnetometry". In: *Physical Review X* 5.4, p. 041001.

Wrachtrup, J et al. (1993). "Optical detection of magnetic resonance in a single molecule". In: *Nature* 363.6426, p. 244.

Yang, Li-Ping et al. (2014). "Electron spin decoherence in silicon carbide nuclear spin bath". In: *Physical Review B* 90.24, p. 241203.

Yang, Sen et al. (2016). "High-fidelity transfer and storage of photon states in a single nuclear spin". In: *Nature Photonics* 10.8, p. 507.

Yoo, Woo Sik and Hiroyuki Matsunami (1991). "Solid-State Phase Transformation in Cubic Silicon Carbide". In: *Japanese Journal of Applied Physics* 30.3R, p. 545. URL: http://stacks.iop.org/1347-4065/30/i=3R/a=545.

You, JQ, JS Tsai, and Franco Nori (2002). "Scalable quantum computing with Josephson charge qubits". In: *Physical review letters* 89.19, p. 197902.

Yu-Chen Chen Patrick Salter, Jorg Wrachtrup (2018). "Laser writing of scalable single colour centre in silicon carbide". In: *arXiv:1812.04284* 24, pp. 6077–6080. URL: https://arxiv.org/abs/1812.04284.

Zetter, Bruce R and Jacqueline Banyard (2002). "Cancer: The silence of the genes". In: *Nature* 419.6907, p. 572.

Zhang, Zesheng et al. (2019). "A new method to characterize underlying scratches on SiC wafers". In: *CrystEngComm*.

Zhao, Lixia and Huiwang Wu (2019). "A correlation study of substrate and epitaxial wafer with 4H-N type silicon carbide". In: *Journal of Crystal Growth* 507, pp. 109–112.

Zhou, Brian B et al. (2017). "Accelerated quantum control using superadiabatic dynamics in a solid-state lambda system". In: *Nature Physics* 13.4, p. 330.

Zvanut, Mary Ellen, Sarah Thomas, and Jamiyanaa Dashdorj (2010). "Intrinsic Surface defects on 4H SiC substrates". In: *MRS Online Proceedings Library Archive* 1246.